CONTRACTOR REPORT

SAND97-0194
Unlimited Release
UC-721

Conceptual Model for Transport Processes in the Culebra Dolomite Member, Rustler Formation

Robert M. Holt
Holt Hydrogeology
17 Sunset Blvd.
Placitas, NM 87043

Prepared by
Sandia National Laboratories
Albuquerque, New Mexico 87185 and Livermore, California 94550

Sandia is a multiprogram laboratory operated by Sandia Corporation, a Lockheed Martin Company, for the United States Department of Energy under Contract DE-AC04-94AL85000.

Approved for public release; distribution is unlimited.

Printed August 1997

Sandia National Laboratories

Issued by Sandia National Laboratories, operated for the United States Department of Energy by Sandia Corporation.

Available to DOE and DOE contractors from
Office of Scientific and Technical Information
P.O. Box 62
Oak Ridge, TN 37831

Prices available from (615) 576-8401, FTS 626-8401

Available to the public from
National Technical Information Service
U.S. Department of Commerce
5285 Port Royal Rd
Springfield, VA 22161

NTIS price codes
Printed copy: A08
Microfiche copy: A01

SAND97-0194
Unlimited Release
Printed August 1997

Distribution
Category UC-721

CONCEPTUAL MODEL FOR TRANSPORT PROCESSES IN THE CULEBRA DOLOMITE MEMBER, RUSTLER FORMATION

Robert M. Holt
Holt Hydrogeology
17 Sunset Blvd.
Placitas, NM 87043

ABSTRACT

The Culebra Dolomite Member of the Rustler Formation represents a possible pathway for contaminants from the Waste Isolation Pilot Plant (WIPP) underground repository to the accessible environment. The Culebra is an intensely fractured medium that displays several scales of fracturing. The vertical distribution of both fractures and porosity in the Culebra is heterogeneous. Two types of porosity are present within fracture-bounded blocks. The geologic character of the Culebra is consistent with a double-porosity, multiple-rate model for transport in which the medium is conceptualized as consisting of advective porosity, where solutes are carried by the groundwater flow, and fracture-bounded zones of diffusive porosity, where solutes move through slow advection or diffusion. As the advective travel length or travel time increases, the nature of transport within a double-porosity medium changes. At small length and time scales, solutes will not have enough time to diffuse or be slowly advected into diffusive porosity, and solute plumes will reflect transport in the advective porosity only. As the length and time scales increase, solutes will have enough time to access the diffusive porosity via diffusion or slow advection, and solute plumes will be physically retarded. At a very large length and time scale, all diffusive porosity will participate in the transport processes, because solutes have time to diffuse or slowly advect into and out of diffusive porosity. This behavior is important for chemical sorption, because the specific surface area per unit mass of the diffusive porosity is much greater than in the advective porosity. Culebra transport experiments conducted at two different length scales show behavior consistent with a multiple-rate, double-porosity conceptual model for Culebra transport. Tracer tests conducted on intact core samples from the Culebra show no evidence of significant diffusion, suggesting that at the core scale the Culebra can be modeled as a single-porosity medium where only the advective porosity participates in transport. Field tracer tests conducted in the Culebra show strong double-porosity behavior that is best explained using a multiple-rate model. At larger length and time scales (e.g., a regional scale), it is likely that the Culebra transport can be modeled adequately using a double-porosity, single-rate model with a large apparent advective porosity.

ACKNOWLEDGMENTS

I couldn't have completed this work without the assistance of many others. I would like to thank Hans Papenguth and Margaret Chu for providing me with the opportunity to work on this interesting and challenging subject. Lucy Meigs was an invaluable technical resource and sounding board. Our conversations about Culebra transport processes and her insightful and timely reviews of text and calculations improved this report, and I sincerely thank her for her efforts. Roy Haggerty cheerfully tolerated untimely phone calls and questions and was always extremely helpful. As usual, Rick Beauheim was patient and helpful when I had questions regarding Culebra hydraulic testing. I thank Hans Papenguth for our discussions on the geologic and geochemical character of the Culebra and other subjects. George Perkins eagerly dug into this topic and provided helpful reviews. Peter Davies and Steve Miller provided thorough reviews and helpful comments on drafts of this report and demonstrably improved its content.

Tina Johnson and Bob Jones of Tech Reps created the figures used here and in several presentations of this material. I sincerely appreciate their efforts and their patience. Sally Kmetz of Tech Reps provided helpful reviews and worked tirelessly to assemble the report.

I take sole responsibility for the results presented in this report.

Robert M. Holt

This work was supported by the U.S. Department of Energy (US DOE) under contract DE-AC04-94AL85000. Sandia is a multiprogram laboratory operated by Sandia Corporation, a Lockheed Martin Company, for the U.S. Department of Energy.

CONTENTS

FIGURES

PLATES

TABLES

1. INTRODUCTION

Transport processes within the Culebra Dolomite Member of the Rustler Formation are important because the Culebra is a potential pathway for contaminants from the Waste Isolation Pilot Plant (WIPP) underground repository to the accessible environment. Because it is the most transmissive geologic unit overlying the WIPP, the Culebra has been the subject of extensive geologic and hydrologic investigations since 1977, and Culebra dolomite has long been recognized as a fractured medium. Within a fractured geologic material, such as the Culebra, pore space is present in both the interconnected network of fractures and the blocks of geologic medium. In the Culebra, this relationship is further complicated because several scales of fracturing are present (Holt and Powers, 1988; Beauheim and Holt, 1990), and several types of porosity occur within the fracture-bounded blocks. In addition, fractures may not be the only advective transport path in the Culebra, as interbeds of poorly cemented, silty dolomite may actively participate in advective transport of solutes. Furthermore, diffusion and slow advection into the fracture-bounded blocks of dolomite may significantly affect solute transport in the Culebra.

In a medium as complex as the Culebra, the processes controlling contaminant transport are too complicated to be represented adequately at all scales by a simple conceptual model. The geology must be characterized in detail; the geologic processes that led to the observed porosity distribution must be understood; and geologic features must be conceptually connected to the physical processes that may control transport within the Culebra. Once the connection between physical processes and the medium has been established, a meaningful mathematical representation of the medium can be constructed.

The objective of this work is to develop a conceptual model for flow and transport processes in the Culebra that is consistent with both geologic and hydrologic observations. Therefore, the current understanding of the geologic and hydrologic character of the Culebra is reviewed. The types of porosity that have been observed in the Culebra are characterized, and these porosity types are connected to transport processes (e.g., advection or diffusion) that may be important in the Culebra. Once the hydrogeologic framework of the Culebra is established, expected transport processes are explored conceptually.

A multiple-rate, double-porosity transport model preserves the physical behavior anticipated for Culebra transport processes, and it represents the simplest mathematical conceptualization of Culebra transport processes that can be applied at all scales. At very small or very large time or length scales, however, the mathematical representation of Culebra transport can be further simplified, and a single-porosity model or a physically-retarded, single-porosity model can adequately describe the arrival of transported solutes. The critical scales at which these simplified models can apply are estimated for the H-19 hydropad using a dimensionless ratio of a characteristic time for advective transport versus a characteristic time for diffusion (Damkohler Type I number). Finally, field and laboratory experiments of transport in Culebra rocks are reviewed.

1.1 Culebra Stratigraphy

In the vicinity of the WIPP site, the Culebra Dolomite Member is the most transmissive unit in the Rustler Formation. It is underlain by a mudstone unit, M-2 of Holt and Powers

(1988), and overlain by anhydrite, A-2 of Holt and Powers (1988). The Culebra is a regionally persistent markerbed within the Rustler that occupies an area greater than 25,000 km^2 (Figure 1-1). Because the depositional margins of the Culebra have been removed by erosion processes, the original depositional extent of the Culebra is unknown. It is likely that the Culebra originally occupied an area approaching 100,000 km^2. Because the scale of the Culebra depositional system was so large, facies tracts within the Culebra depositional system were at a scale much larger than the general WIPP study area, which is less than 1,000 km^2 (Holt and Powers, 1988). The vertical character of the Culebra changes little across most of the WIPP area (Holt and Powers, 1988; Beauheim and Holt, 1990).

Spatial variations in Culebra units within the WIPP area are confined to post-depositional features including fractures and the distribution of gypsum cements. The amount of fracturing present within the Culebra has been qualitatively shown to increase from east to west across the WIPP area (Holt and Powers, 1988; Beauheim and Holt, 1990)

Geologic units described in the WIPP shafts are recognizable in cores from throughout the WIPP region. On the basis of shaft descriptions (Holt and Powers, 1984; 1986; 1990), core descriptions (Holt and Powers, 1988; Holt, 1996), and RaaX (borehole) video logs, the Culebra can be subdivided broadly into four distinct Culebra units (CU) (Figure 1-2), which can be identified in the subsurface across the entire WIPP area. The middle two Culebra units (CU-2 and CU-3) have a similar character and often are not recovered during coring. In the following discussion, the geologic character of each Culebra unit is discussed.

1.1.1 Culebra Unit 1

The uppermost unit in the Culebra, CU-1 (Figure 1-2), corresponds to air intake shaft (AIS) mapping units 1 and 2 (Holt and Powers, 1990). Its thickness ranges from 2.5 m to 3.2 m and averages 3.0 m in the WIPP area (Table 1-1). CU-1 consists of well-indurated, microcrystalline dolomite. CU-1 is more massively bedded than the underlying units, and strata within the beds are generally parallel. Some burrows are present, and bioturbation becomes less common upward. Several areally persistent zones showing cryptalgal layering occur within the upper part of CU-1, and many cores show dark brown-stained, bedding-plane separations in the vicinity of these features. Laminae of poorly cemented, silt- to clay-size (silty) dolomite are rare at the base and become more common upward; they are flat with minor undulations along the contacts. Core often separates along these interlaminae. The upper 0.3 to 0.6 m of CU-1 consists of partially cemented silty dolomite with cryptalgal layering. This zone may also contain oolites or coated grains. The top of the Culebra is often marked with organic-rich, crinkled "algal" laminae or stromatolitic mounds (Holt and Powers, 1984; 1988). Fractures are less common than in lower units and are usually parallel to bedding planes or may propagate subvertically from bedding plane to bedding plane. At the AIS, CU-1 is bisected by several synsedimentary reverse faults. These faults originate along slumped zones at the contact between the unnamed lower member and the base of the Culebra and may show up to 1.5 m of throw (Holt and Powers, 1990). Overlying dolomite beds thicken over the displaced section and have flat upper surfaces showing no displacement. Dark brown stains occur along the faulted surfaces. CU-1 usually contains very few large vugs, although microvugs are common and frequently

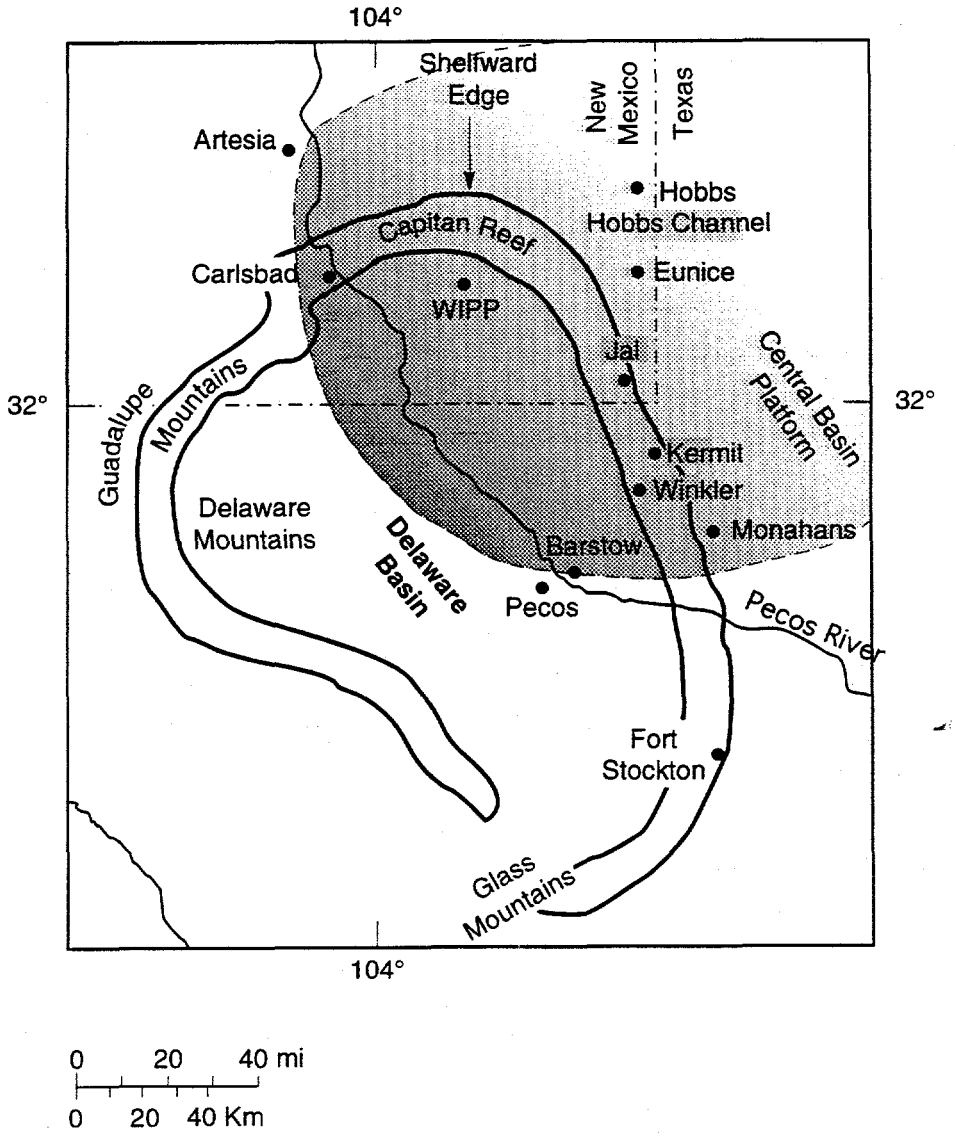

Figure 1-1. Approximate areal extent of the Culebra Dolomite Member of the Rustler Formation.

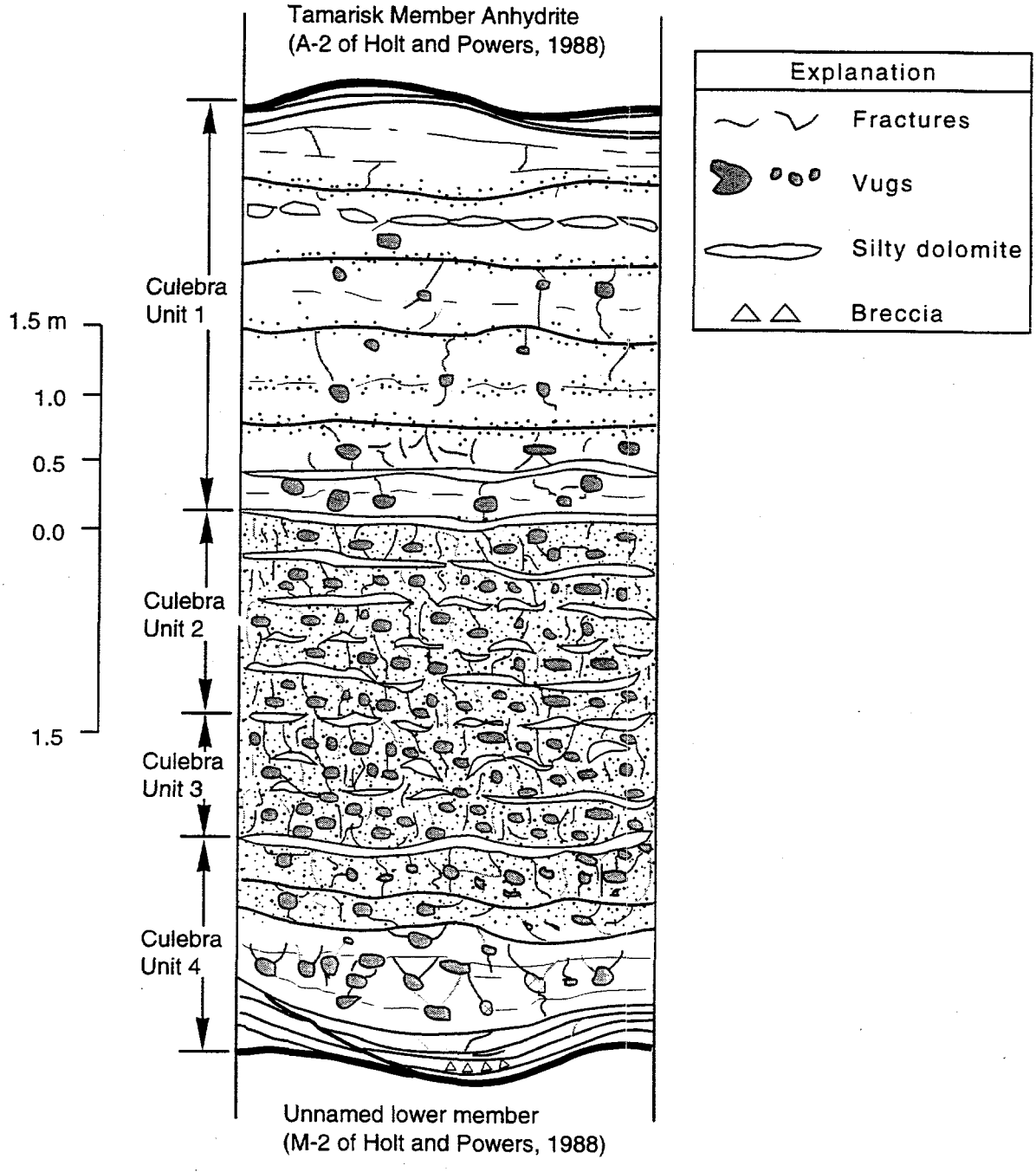

Figure 1-2. Culebra stratigraphic subdivisions.

Table 1-1. Compilation of Culebra Unit Thickness Data

Well	CU-1 Thickness (m)	CU-2 + CU-3 Thickness (m)	CU-4 Thickness (m)	Total Thickness (m)
WIPP 19[1]	3.20	2.71	1.40	7.31
DOE-2[1]	2.99	2.56	1.34	6.89
H-5b[1]	2.83	-	-	-
H-10c[1]	~4.27	~2.44	~2.23	~8.93
H-12[1]	3.32	3.02	1.6764	8.02
H-15[1]	2.93	~1.98	~1.56	6.71
H-17[1]	3.14	2.62	1.86	7.62
H-18[1]	2.53	3.02	1.43	6.98
H-19 (Avg.)[2]	2.99	2.68	1.52	7.19
H-3b3[3]	2.99	-	-	-
H-6b[3]	3.02	-	-	-
H-11[3]	3.02	-	-	-
Waste handling shaft[4]	3.20	-	-	6.71
Exhaust shaft[5]	3.20	-	-	6.86
Air intake shaft[6]	2.59	3.05	1.68	7.32
Average	2.99*	2.80*	1.55*	7.35*/7.32**

Average values marked by * reflect only those data that are not an approximation (indicated by ~). The total average thickness value marked by * is the sum of the average thicknesses for each unit. The total average thickness value marked by ** is the average of the total thickness values.

[1] Data derived from previously unpublished core descriptions by Holt and Powers (Holt, 1996).

[2] Data are average values for the H-19 hydropad and are derived from Table A-1 of Holt (1996). CU-2, CU-3, and CU-4 thickness values reflect core averages, and CU-1 data reflect RaaX averages.

[3] Data from interpretations of RaaX logs. The values for CU-1 from the H-11 hydropad are an average of the thicknesses interpreted from H-11b2 (3.14 m), H-11b3 (2.96 m), and H-11b4 (2.96 m).

[4] Data from Holt and Powers (1984).

[5] Data from Holt and Powers (1986).

[6] Data from Holt and Powers (1990).

occur in zones that parallel stratification. Poikilotopic gypsum cements typically fill some vugs, microvugs, and fractures. The upper contact of the Culebra is sharp and distinct.

1.1.2 Culebra Unit 2

The second Culebra unit, CU-2 (Figure 1-2), ranges in thickness from 1.4 m to 1.8 m where it has been uniquely identified in cores and shafts (Table 1-1). It corresponds to AIS mapping unit 3a, is intensely fractured, and was described by Holt and Powers (1990) as a

packbreccia. The term packbreccia (Morrow, 1982) refers to a highly broken rock with limited rotation of the broken pieces. The portions of the Culebra classified as packbreccia appear similar to a jigsaw puzzle with all of the pieces placed in the correct place, but not interlocked. Intact pieces of dolomite show laminations and thin beds with some cross-cutting relationships. Strata are mostly parallel and flat, although some low-angle cross-stratification, ripple cross-laminae, and ripple forms are preserved. Interbeds of silty dolomite from 1 cm to 7 cm thick become more abundant near the top of CU-2. Subhorizontal burrows, up to 5 cm long and 1 cm in diameter, occur within well-indurated dolomite. Small-scale, soft-sediment deformation is locally abundant because strata are slumped, sheared, and disrupted to varying degrees. Near the base, silty dolomite strata are typically disrupted and may form irregular masses. Vugs and gypsum nodules, to 7 cm in diameter, are locally abundant in CU-2. In places, these vugs give the unit a honeycombed appearance and disrupt and disconnect strata. The margins of some nodules and vugs show soft-sediment displacement and may exhibit concentric zoning of darker material within the dolomite around their margins. Many vugs are partially to completely collapsed. Nearly all vugs are interconnected by fractures. Zones of large vugs may follow bedding planes. Where these vugs are open and have collapsed, zones of breccia parallel stratification. Open and gypsum-filled, subvertical fractures to 0.2 cm wide extend from vug to vug, originate along bedding planes, and bound collapsed vugs. Most of these fractures are less than 5 cm long and are spaced from 0.5 to 5 cm apart. Fracture surfaces are frequently stained orange or dark brown. The upper contact of CU-2 is gradational to diffuse.

1.1.3 Culebra Unit 3

The third unit in the Culebra, CU-3 (Figure 1-2), is between 1.0 m and 1.5 m thick (Table 1-1). It corresponds to AIS mapping unit 3b. CU-3 is generally thinly laminated to very thinly bedded with low-angle cross-laminae, cross-cutting relationships, and wavy to lenticular bedding (Holt and Powers, 1990). Soft-sediment disruption is common, and strata are slumped, disrupted, sheared, and displaced causing some interbeds to become very discontinuous. Vertical displacement from soft-sediment deformation, however, rarely exceeds 5 cm. Laminae and very thin beds of silty dolomite are irregular, highly discontinuous, and deformed. Individual irregular masses of silty dolomite are displaced downward from their original position by soft-sediment slumping. Large (up to 5 cm diameter) vugs and gypsum nodules are common. In some locations (e.g., the AIS) microvugs are common. Some vugs have collapsed, causing locally intense fracturing. At the AIS, Holt and Powers (1990) describe CU-3 as a packbreccia because of its extremely fractured appearance.

In Culebra cores, intact pieces of CU-3 are rare; this interval is typically crushed or unrecovered. Crushed core consists of blocks of well-indurated, microcrystalline dolomite with abundant silt- to clay-size dolomite flour. Crushed blocks range in size from < 1 cm to ~10 cm on a side. The dolomite flour is probably derived from silty dolomite interbeds. Photographs of CU-3 core (e.g., core from the H-19 hydropad), prior to its removal from the core barrel, also show that the unit is intensely fractured. Fractures are subvertical to vertical, often occur in a semi-radial fashion emanating from the tops of collapsed vugs, and frequently occur between vugs, nodules, and deformed silty dolomite interbeds. Fractures are spaced several centimeters apart and typically extend less than 5 cm. Fracture surfaces commonly display an orange or dark brown stain.

1.1.4 Culebra Unit 4

The lowermost Culebra unit, CU-4 (Figure 1-2), corresponds to AIS mapping units 3c and 4. This unit is typically between 1.4 m and 1.9 m thick (Table 1-1), and its average thickness is 1.6 m in the WIPP area. The lower contact of CU-4 is irregular and undulatory, with undulations up to 1.0 m in WIPP shafts (Holt and Powers, 1986; 1990). The lowermost 15 cm to 30 cm consists of thinly laminated to laminated dolomicrite with thin argillaceous partings. The structure of these laminae mimics the lower contact. Where the undulations at the lower contact are most extreme, the laminated dolomite is often brecciated (Holt and Powers, 1986). The remainder of CU-4 is thinly laminated to very thinly bedded. These strata are mostly flat to wavy and show low-angle, cross-cutting relationships and some hummocky cross-stratification. Strata are downwarped where undulations occur at the base of CU-4 (Holt and Powers, 1990). Near the top of CU-4, several interlaminae of silty dolomite occur. These interbeds show moderate amounts of soft-sediment deformation. Large gypsum nodules and vugs (up to 8 cm in diameter) may occur in the lower 30 cm of this zone. Some of these nodules and vugs show evidence of collapse. Gypsum-filled, subvertical fractures connected with angular, gypsum-filled pore spaces are preserved in some cores. The shapes of these features are consistent with minor downward displacement with horizontal extension. Cores of CU-4 often separate along bedding planes (spaced 6 cm to 30 cm) showing orange or dark brown stains. Gypsum-filled or open, subvertical fractures also showing dark brown or orange stains terminate at these bedding planes. Small, open vugs (< 3 mm) are common in CU-4 and appear to be concentrated in the vicinity of bedding-plane partings. The upper contact of CU-4 is gradational in WIPP shafts and marked by brecciation in cores.

1.2 Sulfate Minerals in the Culebra

Sulfate minerals (gypsum or anhydrite) are found within nodules and as secondary cements in vugs, fractures, intercrystalline pore spaces, and interparticle porosity. The distribution of sulfate cements within the Culebra exhibits a clear pattern east to west across the WIPP area (Beauheim and Holt, 1990). The following discussion is based on observations of WIPP core (Holt and Powers, 1988; Holt, 1996), shafts (Holt and Powers, 1984; 1986; 1990), and Culebra thin sections (Holt, 1996).

In the eastern part of the WIPP area, nodules contain gypsum and anhydrite. Anhydrite typically forms a microcrystalline core in nodules and consists of blocky crystals 5 to 25 microns (μm) across that show varying amounts of replacement by gypsum. Gypsum occurs along the outer margins of the nodules and usually displays a fibrous crystal habit. Fibrous gypsum within nodules is more porous than anhydrite and is often penetrated by the blue epoxy in impregnated thin sections. Some gypsum crystals are poikilotopic and completely surround zones of anyhydrite crystals. Rims of dark material occur along some contacts between gypsum and anhydrite. Some nodules contain separate zones, or domains, of gypsum separated by thin rims of dark material. These features appear similar to coalesced gypsum nodules found in modern saline mudflat deposits. Open and fibrous to poikilotopic gypsum-filled fractures (40 μm to 50 μm wide) intersect the nodules.

In the eastern region, many fractures in the Culebra are filled with fibrous gypsum, and some fibrous gypsum contains relict laths of anhydrite. Anhydrite crystal laths and lath-shaped

molds less than 2 mm across are associated with dark-brown, finely-crystalline, argillaceous dolomite. Many "microvugs" are molds of anhydrite laths. Often lath-shaped molds are found within laminae of argillaceous dolomite. Occasionally, they coalesce into groups. Gypsum occasionally fills molds of anhydrite laths, indicating replacement or when the gypsum is in optical continuity with adjacent fractures or lath-fillings (poikilotopic pore filling).

In the central part of the WIPP area, nodules contain only gypsum (Plate 1-1), and the sulfate within some nodules has been removed, leaving vuggy porosity. Some of the nodules show fibrous gypsum crystals surrounding several larger gypsum crystals at the center. In some cases, gypsum in adjacent fractures and vugs may be in optical continuity with the coarser gypsum in the center. In other cases, nodules may contain a single poikilotopic crystal that is in optical continuity with adjacent fractures and vugs. Westward, poikilotopic cements and fracture fillings become more common. Some open vugs and gypsum nodules show evidence of partial to complete collapse (Plate 1-2). Fractures are commonly filled with large poikilotopic gypsum crystals that show optical continuity with gypsum in adjacent fractures and vugs (Plates 1-3 and 1-4).

In the western and southern part of the WIPP area, gypsum is rare, and open vugs are common. Many of the larger vugs show evidence of collapse, and fractures do not contain gypsum fillings. Within Nash Draw, some fractures show subhedral to euhedral, medium- to coarsely-crystalline, calcite crystal linings.

In summary, anhydrite nodules and crystals are partially replaced by gypsum, and fractures contain fibrous, antitaxial gypsum fillings in the eastern part of the WIPP region. Farther west, all sulfate consists of gypsum; poikilotopic gypsum cements become more common; and gypsum fracture fillings, cements, and vug fillings are partially to completely dissolved. Continuing west, little gypsum is present, large vugs and closely spaced groups of smaller vugs are collapsed, and fractures are open to their full aperature. In the western-most part of the region, no gypsum occurs.

The overall areal pattern of sulfate cements can be inferred by the percentage of natural fractures filled with gypsum (Figure 1-3) (Beauheim and Holt, 1990). Fracture data for Figure 5-16 were collected from cores by counting the numbers of filled and open natural fractures intersected by a scan line. The most important feature in Figure 1-3, the zone containing few gypsum filled fractures, is in the southern part of the WIPP site. This feature corresponds roughly to reported high transmissivities in the Culebra (see Section 1.4).

1.3 Geologic History of the Culebra

The geologic history of the Culebra has been described by Holt (1988), Holt and Powers (1988), Powers and Holt (1990), and Beauheim and Holt (1990). The following interpretation is consistent with their interpretations, but reflects minor revisions resulting from the collection of additional WIPP cores, recent studies of the regional geology (Powers and Holt, 1995a; 1995b), and advances in the field of evaporite sedimentology (e.g., Holt, 1993).

Culebra sediments were deposited in lagoonal environments that developed following a transgression of marine waters over salt-pan and saline-mudflat sediments (Holt and Powers, 1988). After the transgression, marine waters dissolved and reworked salt-pan sediments (Figure 1-4, T1), and Culebra sediments began to accumulate on a very unstable substrate (Figure 1-4,

TRI-6801-26-0

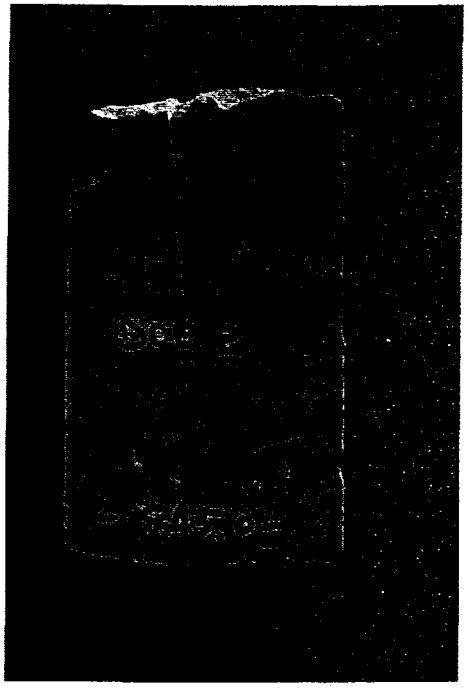

Plate 1-1. Gypsum nodule in Culebra dolomite. Gypsum-filled fractures originate at the top of the nodule. Note subvertical open fracture near center of core. Core width is ~5 cm.

TRI-6801-27-0

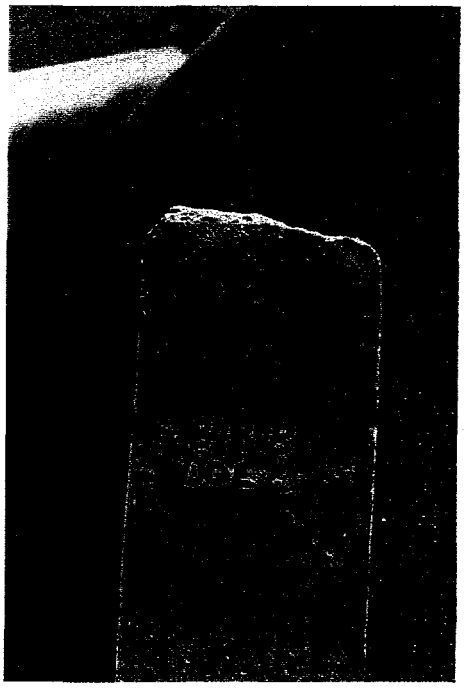

Plate 1-2. Partially collapsed vugs in Culebra dolomite containing poikilotopic gypsum cements. Open microvugs occur within collapsed blocks of intact dolomite. Core width is ~5 cm.

TRI-6801-28-0

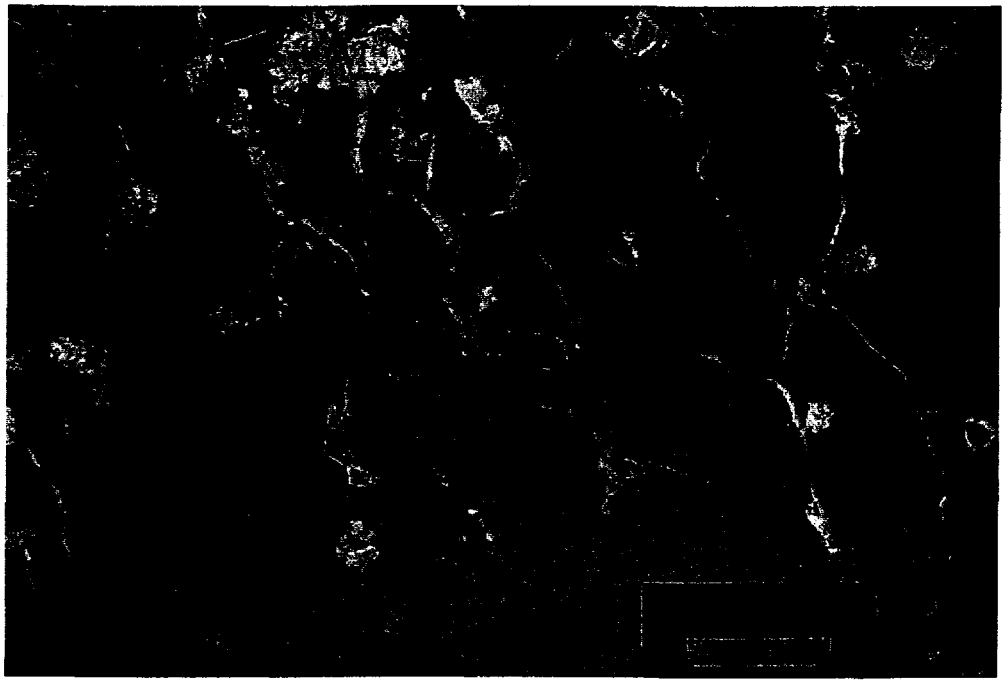

Plate 1-3. Photomicrograph of Culebra dolomite in cross-polarized light. Dolomite contains open vugs, open fractures, and vugs and fractures cemented with poikilotopic gypsum. Orange stains occur along some fracture surfaces. Near the center of the photomicrograph some orange stains occur between microcrystalline dolomite and gypsum cements. Scale bar equals 3.3 mm.

T2). As Culebra sediments were collecting, the substrate would episodically shift or slump downward as salt dissolved from below the Culebra and the muddy salt-pan sediments dewatered (Figure 1-4, T3). These movements disrupted, sheared, and deformed Culebra sediments. The substrate ultimately became stable after a significant thickness of Culebra had accumulated or all of the underlying soluble salts had been removed. After Culebra sediments were no longer affected by soft-sediment deformation processes, planar strata accumulated and remained undeformed (Figure 1-4, T4). Bottom-grazing and burrowing animals also disrupted Culebra sediments. As evaporation reduced the depth of the Culebra lagoon and increased its salinity, these animals died, and algal mats that trapped detrital sediment began to form on the substrate. By the time the upper part of the Culebra was accumulating, sediments were no longer disrupted by bioturbation or soft-sediment deformation processes. As evaporation continued, the Culebra lagoon shallowed, and oolites developed in local shoals. Evaporation eventually concentrated the lagoonal waters to gypsum saturation, and gypsum began to accumulate on the lagoon substrate, marking the end of Culebra deposition.

Important diagenetic processes began to affect the Culebra while the overlying units accumulated. After gypsum deposition began above the Culebra, pore waters within Culebra sediments quickly reached gypsum saturation (Holt and Powers, 1988). Gypsum crystals and nodules grew within and near the more disrupted and permeable parts of the Culebra (Figure 1-4, T4). As gypsum accumulated within and above the Culebra, the Ca^{+2}/Mg^{+2} ratio began to decrease, and dolomite began to replace fine-crystalline calcite or aragonite mud. However, dolomite and gypsum cements did not completely fill all porosity within Culebra sediments, and some dolomite mud remained uncemented. After the gypsum unit accumulated above the Culebra, a saline mudflat/salt pan began to develop (Holt and Powers, 1988). As this occurred, pore waters within the Culebra and the overlying gypsum unit approached halite saturation. At this concentration, anhydrite is more stable than gypsum (Braitsch, 1971), and anhydrite began to replace gypsum crystals and nodules in the Culebra. Also, small anhydrite crystals grew within the more permeable Culebra sediments (e.g., disrupted sediments and along bedding planes). In some places east of the WIPP site (e.g., P-18), thick sections of salt-pan halite accumulated in the section above the Culebra. In these locations, Culebra pore waters may have been concentrated above halite saturation. Under these conditions, halite may have replaced gypsum in the Culebra and cemented Culebra sediments (a process equivalent to that responsible for halite pseudomorphs after gypsum elsewhere within the Rustler and Salado Formations–see Holt and Powers, 1990 and Holt, 1993 for additional explanation of these processes), but this remains unconfirmed because of the lack of core data.

By the close of the Permian, the Culebra was covered by at least 200 m of overburden (Figure 1-5) (Powers and Holt, 1995b). By the end of the Triassic, up to 570 m of rocks had accumulated over the Culebra. The Jurassic was a period of erosion or non-deposition. During the Cretaceous, up to 300 m of additional sediment may have accumulated in the WIPP area. If no erosion occurred between the Triassic and the end of the Cretaceous, the Culebra may have been buried to a depth exceeding 800 m.

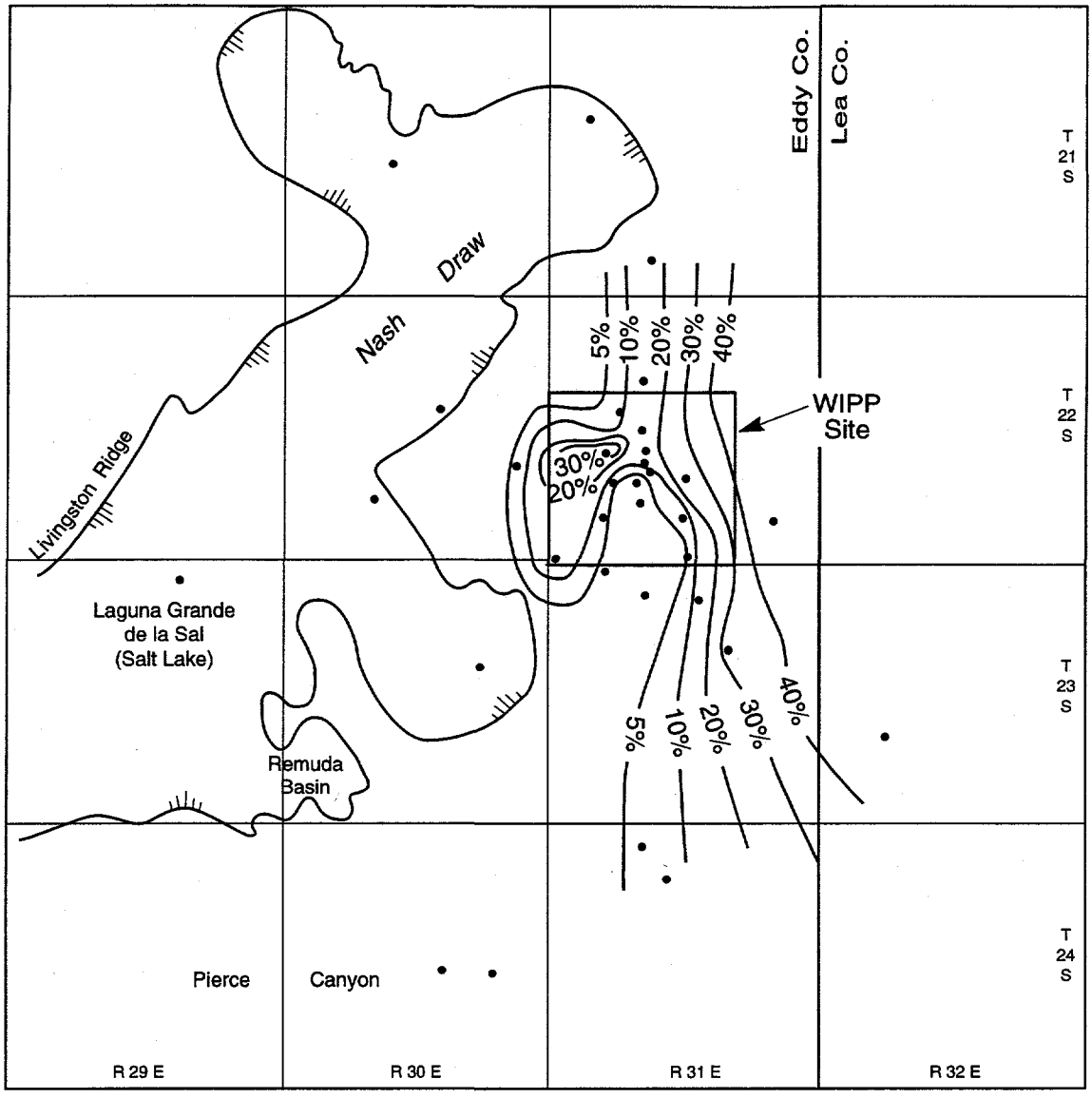

Figure 1-3. Percentage of natural Culebra fractures filled with gypsum (Beauheim and Holt, 1990).

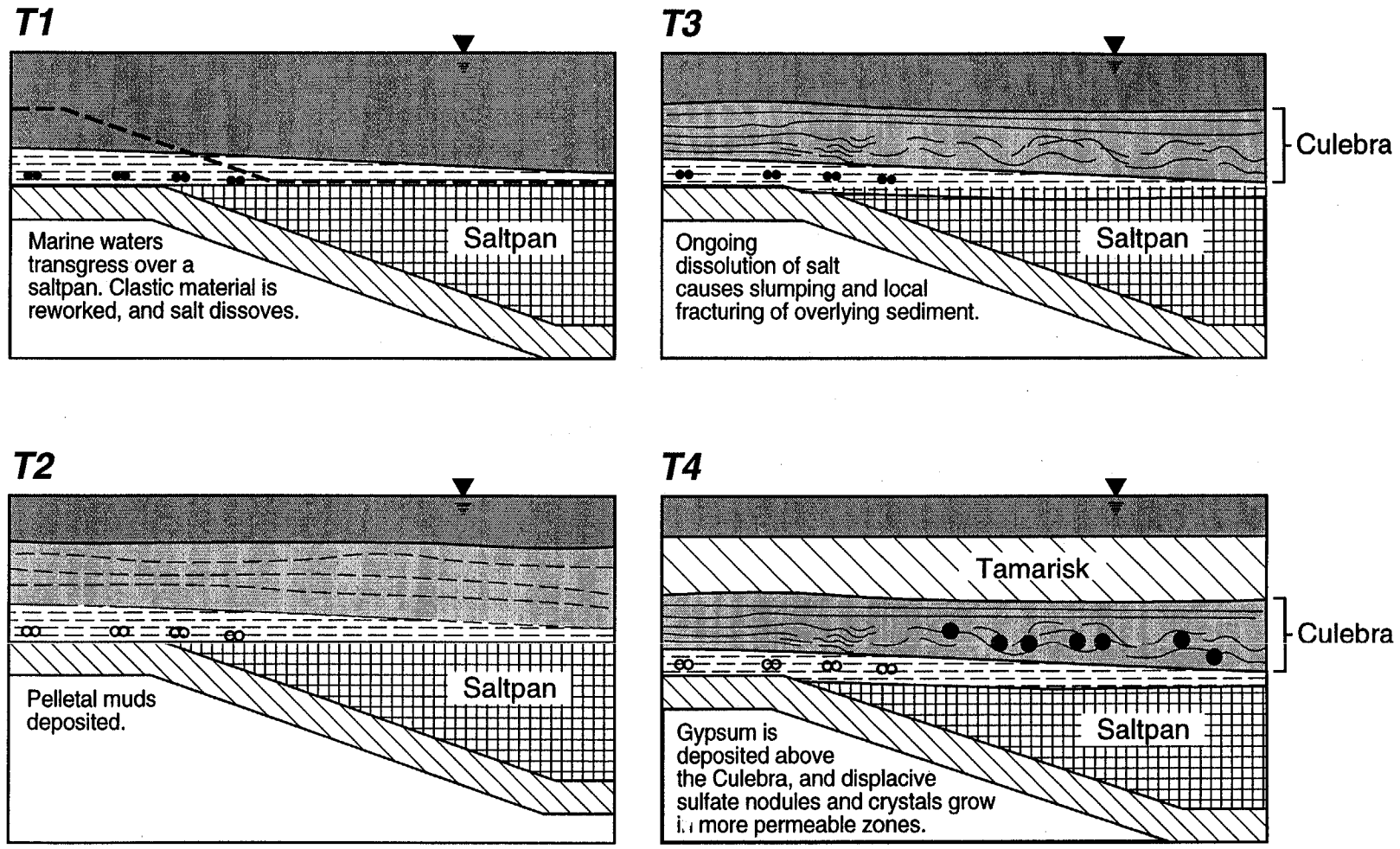

Figure 1-4. The depositional model for Culebra Dolomite Member of the Rustler Formation (modified from Holt and Powers, 1988).

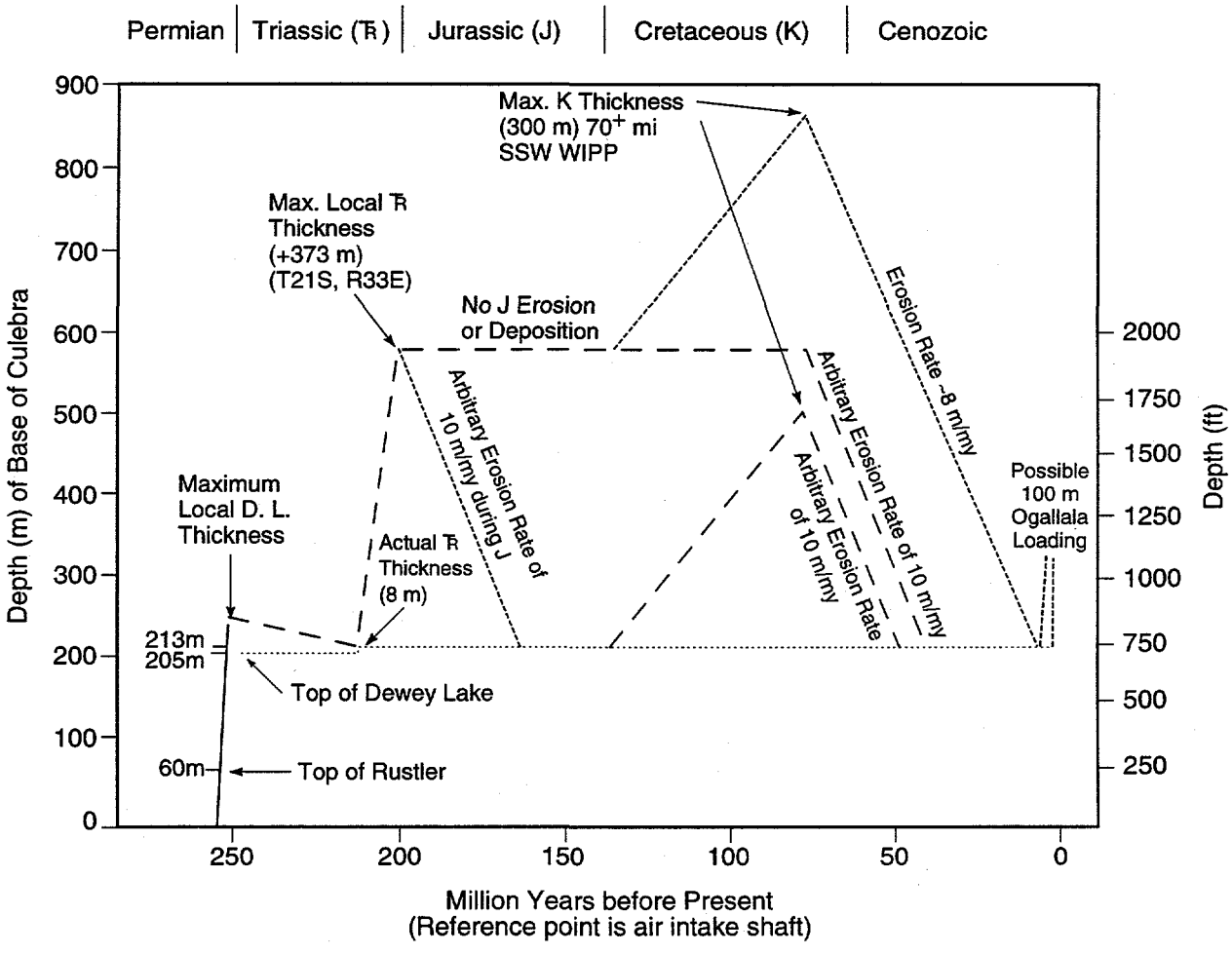

Figure 1-5. Burial history of the Culebra at the WIPP site (Powers and Holt, 1995b).

The Culebra is affected by a large anticline north of the WIPP site (Powers and Holt, 1995b). This anticline formed following gravity foundering in the Castile Formation, probably during the Cretaceous. By the middle of the Cenozoic, the western edge of the Delaware Basin was uplifted, and this may have introduced additional regional stresses in the Culebra. Erosion

associated with this uplift exposed the up-dip edge of Permian evaporites to circulating, low-salinity ground waters, and much of the Permian evaporite section was removed as soluble salts dissolved.

By the late Cenozoic (Pliocene/Pleistocene), the combination of eastward moving erosion and dissolution caused the development of karst features in the WIPP vicinity, including Nash Draw (Powers and Holt, 1995a and 1995b). Within Nash Draw, up to 200 m of salt from the upper part of the Salado Formation have been dissolved, and the overlying rocks, including the Culebra, are extensively brecciated. Across most of the WIPP area, however, the upper part of the Salado Formation has suffered no dissolution (Figure 1-6).

Erosion dominated the WIPP area through most of the Cenozoic, although small amounts of terrigenous clastic material accumulated in local depressions (Powers and Holt, 1995a). In the WIPP area, the depth to the top of the Culebra decreases from east to west. Since its maximum burial, the depth of the Culebra at the WIPP site has been reduced by at least 350 m and possibly by as much as 650 m (Figure 1-5). This represents a significant reduction of vertical stress on the Culebra. Much of this erosion probably occurred during the Cenozoic. Where the Culebra is not affected by Salado dissolution, fractures may have developed in response to stress-relief associated with this erosion.

The following geological model is proposed for the Cenozoic history of the Culebra. It is, in part, based on and is generally consistent with the model reported by Beauheim and Holt (1990), but has been revised slightly to reflect additional core data.

The interpretations regarding fracturing are, in part, based on the following models of fracture behavior. Stress is concentrated along discontinuities and boundaries between different materials within rocks, and fractures often initiate along these features and propagate from feature to feature (Engelder, 1987; Zaitsev, 1985). Materials that are very mechanically heterogeneous typically develop tortuous fracture pathways (Atkinson and Meredith, 1987), and mechanical inhomogeneities serve as loci for strain and complex fracturing with an apparently random orientation. Engelder (1987) suggests that most random fracture patterns develop in association with unloading.

During the Cenozoic, erosion progressed from east to west across the WIPP area, and stress-relief fractures in Culebra units developed as the vertical stresses were reduced (Figure 1-7). The upper units in the Culebra were more mechanically homogeneous and separated along well-defined bedding planes, while shorter length fractures formed along pre-existing shear planes, between nodules of anhydrite, and around deformed strata in the disrupted, mechanically-heterogeneous lower part of the Culebra. Anhydrite nodules were replaced by gypsum as fractures developed and allowed access for pore waters (Figure 1-8). Culebra pore waters were saturated with gypsum, and some fractures were filled by fibrous gypsum crystals as they opened (Durney and Ramsay, 1973). In some areas east of the WIPP site, high ionic-strength waters may have been present, and anhydrite may have precipitated within fractures. Later, lower ionic-strength waters entered these areas, and anhydrite within fractures was replaced by gypsum.

As erosion and stress-release continued, developing fractures followed the earlier patterns, and waters capable of dissolving gypsum fracture-fillings and nodules circulated in Culebra fractures and pores. As gypsum dissolved from nodules, vugs, large, open-void spaces, were created in the Culebra. The dolomite surrounding some of these vugs could not support the

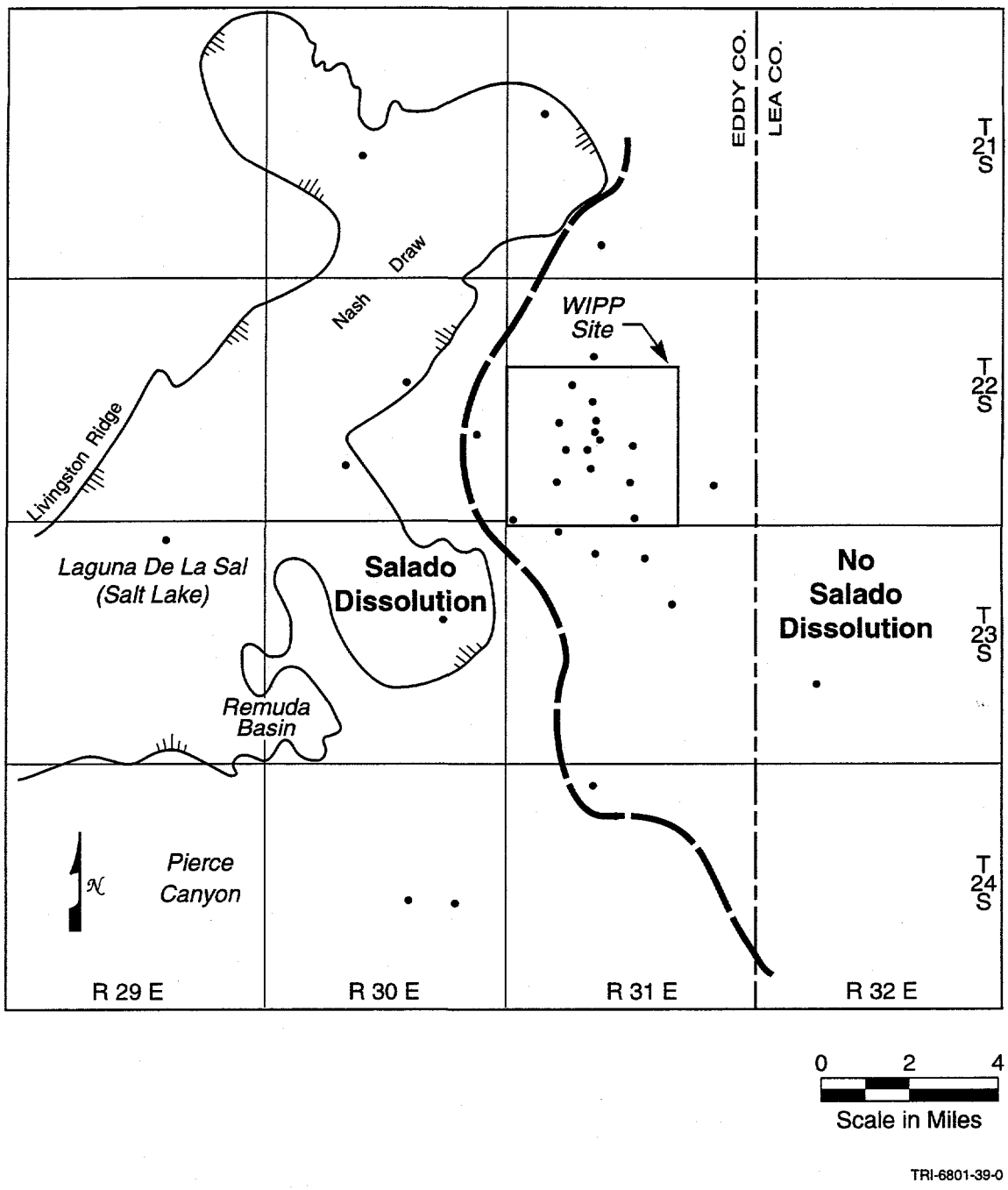

Figure 1-6. Margin of Salado dissolution in the vicinity of the WIPP site (Powers and Holt, 1995b).

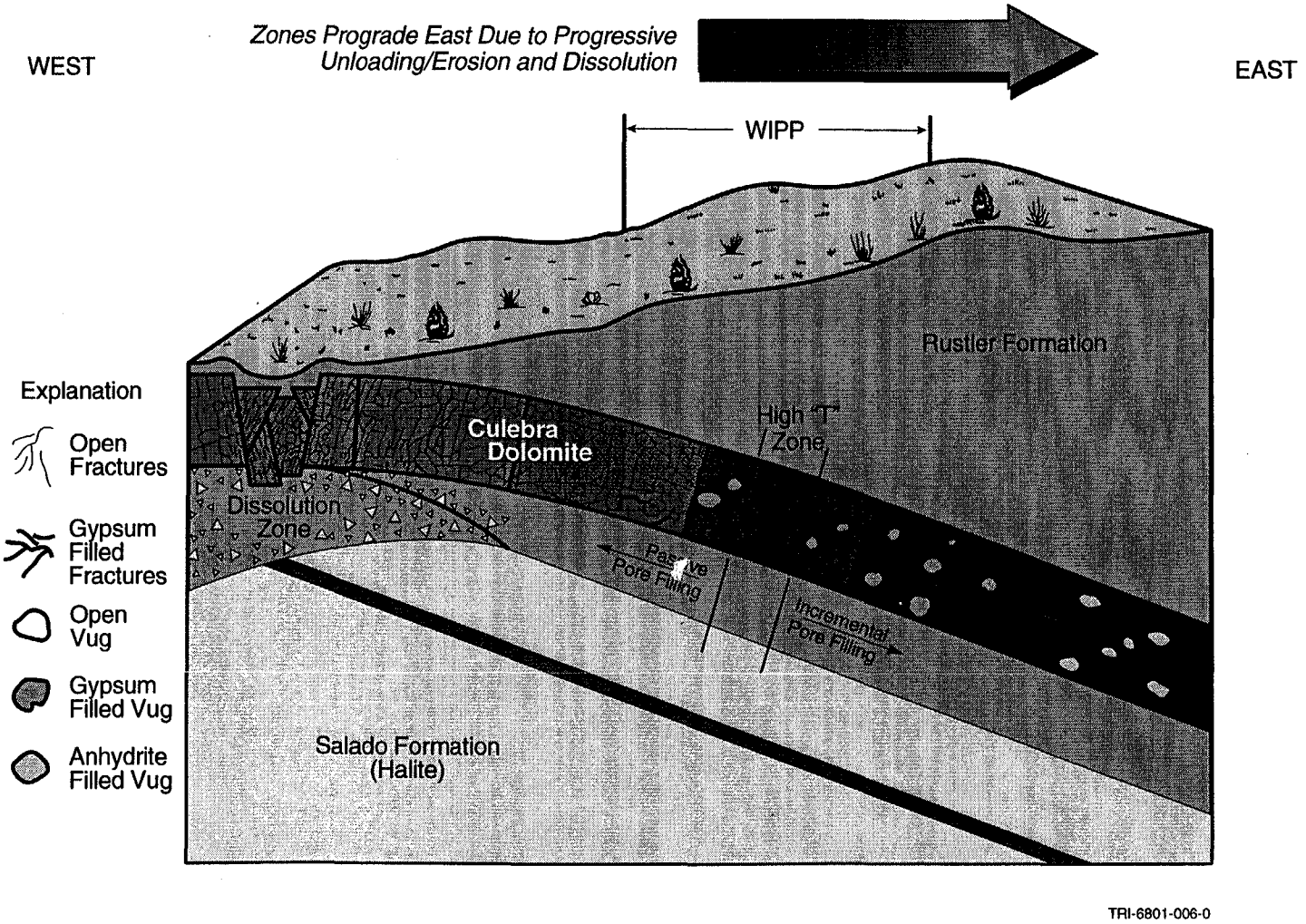

Figure 1-7. Post-depositional history of the Culebra in WIPP area (modified from Beauheim and Holt, 1990).

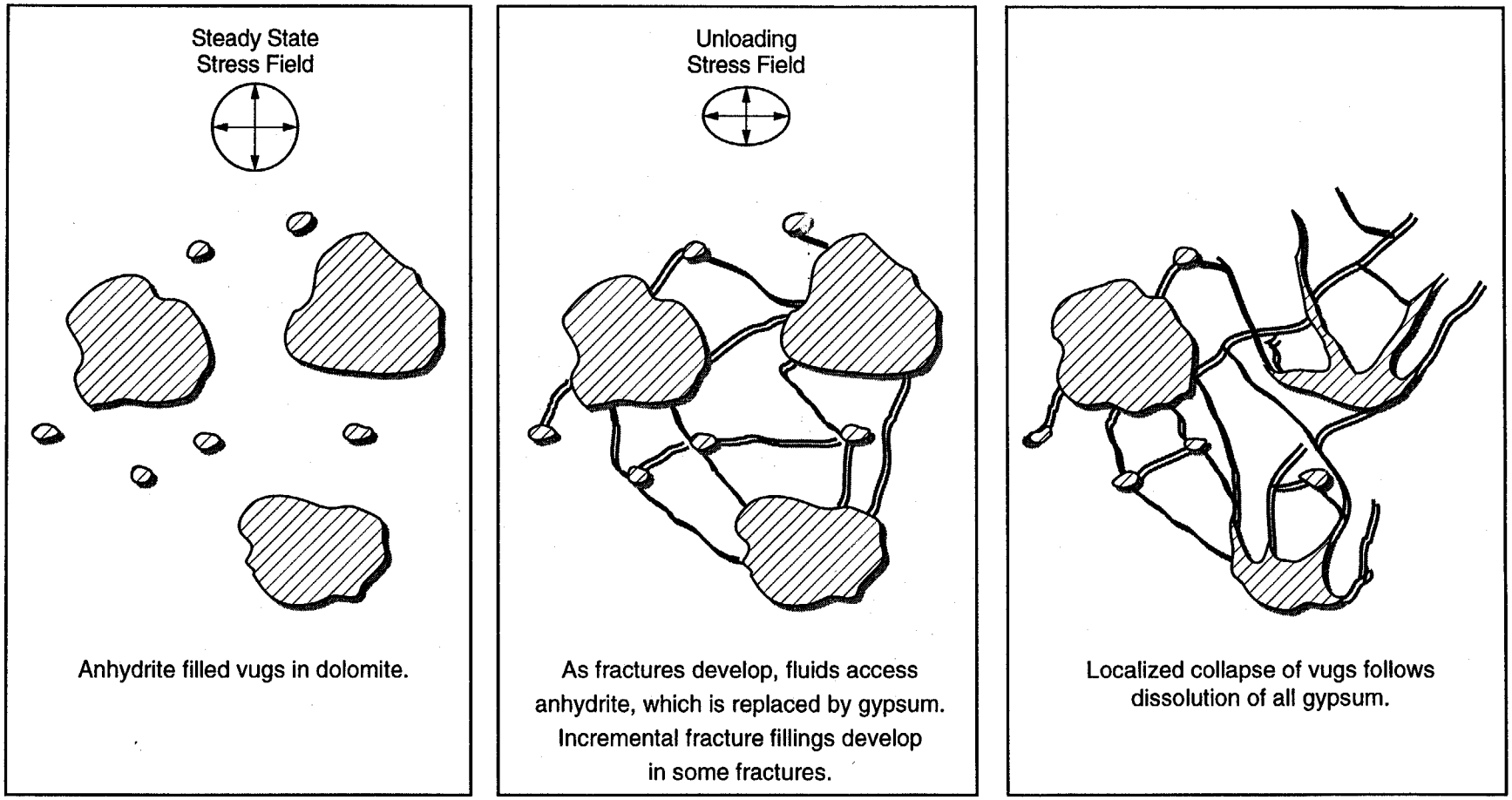

Figure 1-8. Mechanical response of vugs to unloading and dissolution of vug fillings.

opening, and the vugs collapsed, creating additional small-scale fractures. In the western part of the WIPP area, much of the gypsum pore-filling cements were removed (Beauheim and Holt, 1990).

In the western part of the WIPP area, the Culebra groundwater chemistry changed, at least once, and slowly-grown, poikilotopic gypsum cements filled some open fractures and pores, including vugs. In the vicinity of Nash Draw, all gypsum pore-filling cements have been dissolved, and no evidence of recementation with gypsum has been observed.

In some locations (e.g., Nash Draw), erosion was sufficient to allow circulating ground waters to access and dissolve the upper part of the Salado salt. The rocks overlying the Salado, including the Culebra, collapsed and were brecciated. As this process continued, the Culebra lost stratigraphic continuity and became displaced and vertically disrupted.

The processes associated with Rustler Formation depositional environments set the stage for later diagenetic events to produce the porosity distribution now present in the Culebra. In the lower to middle part of the Culebra (e.g., CU-2 and CU-3), soft-sediment deformation disrupted the sediments, allowing the growth of gypsum nodules. Deformed interbeds, shear planes, and nodules were small-scale mechanical inhomogeneities that served as the loci for small-scale fractures. The upper part of the Culebra was not deformed, and fractures there typically occur along bedding planes and are more areally persistent.

1.4 Culebra Hydrology

In the vicinity of the WIPP site, the Culebra is the most transmissive unit in the Rustler Formation. Water levels in 60 wells completed to the Culebra at 41 drilling-pad locations have been measured on a regular basis (Beauheim and Holt, 1990). Since late 1981, however, Culebra water levels at and around the WIPP site have been affected by continuous drainage into one or more WIPP shafts, as well as by numerous pumping tests and water-quality sampling exercises (Lappin, 1988). Cauffman et al. (1990) thoroughly reviewed Culebra water-level data, borehole-fluid density data, and WIPP-related hydraulic stresses, and estimated the undisturbed freshwater heads at 35 wells. Flow is generally to the south (Crawley, 1988; Lappin, 1988) across the WIPP site area. Davies (1989), Crawley (1988), and Corbet and Knupp (1996) suggest that flow directions south of the WIPP site may have a larger easterly, down-dip component than is predicted when considering only freshwater heads (Figure 1-9).

The transmissivity of the Culebra across the WIPP region varies by six orders of magnitude because of varying open fractures within the Culebra (Beauheim and Holt, 1990). In the vicinity of the WIPP, the Culebra has been tested in 47 locations (Figure-10), including the combined testing of the WIPP project and Project Gnome (Beauheim, 1996). The highest transmissivity value reported for the Culebra is 2×10^{-3} m^2/s at borehole H-7 within Nash Draw. The lowest value reported is $< 4\times10^{-9}$ m^2/s at P-18. Where Culebra transmissivities are less than 2×10^{-6} m^2/s, the Culebra behaves hydraulically as a single-porosity medium during pumping and slug tests (Beauheim and Holt, 1990). Where transmissivities are greater than 2×10^{-6} m^2/s, the Culebra hydraulically behaves as a double-porosity medium, with matrix and fracture porosity (Beauheim and Holt, 1990).

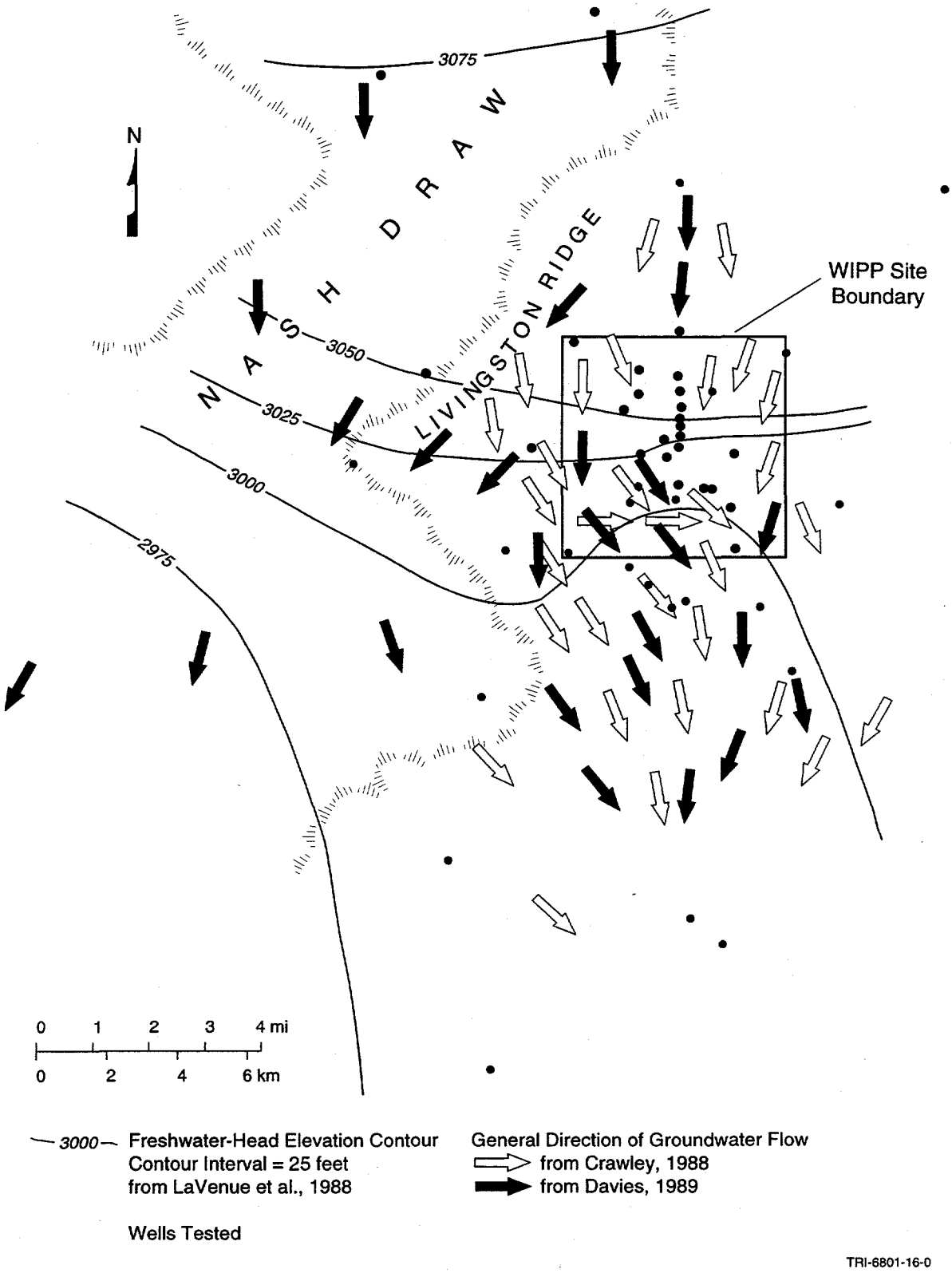

Figure 1-9. Culebra flow directions in the vicinity of the WIPP Site (after Crawley [1988] and Davies [1989]).

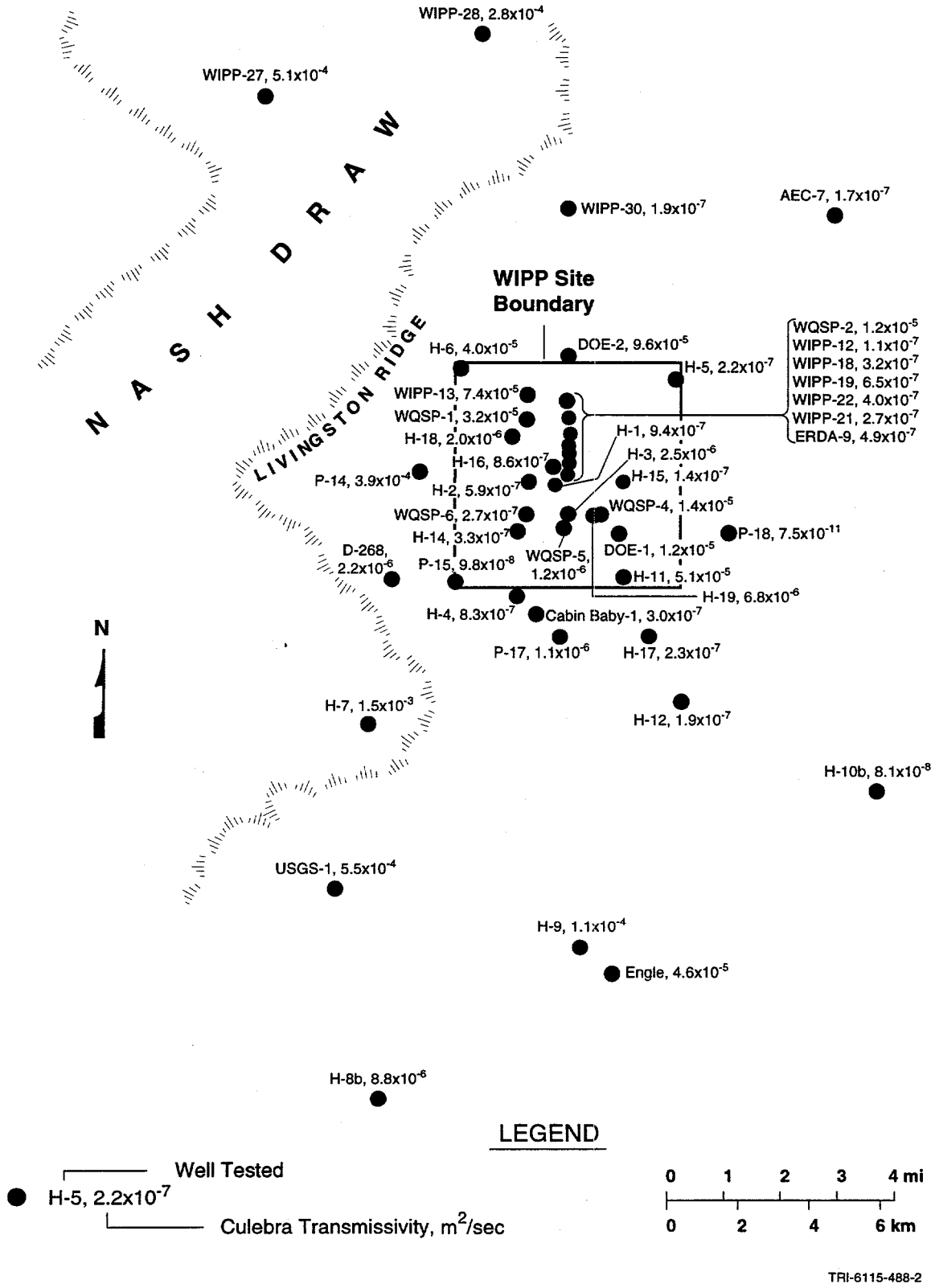

Figure 1-10. Culebra test locations and estimated transmissivity (data from Beauheim, 1996)

LaVenue et al. (1990) calculated Culebra transmissivities across the WIPP site area based on steady-state calibration against an estimate of the pre-shaft distribution of freshwater equivalent heads and transient calibration against hydraulic responses to large-scale pumping tests and leakage into WIPP shafts (Figure 1-11). Aside from the apparent increase of transmissivity toward Nash Draw, several other relationships are important. Transmissivities are relatively high in a wide region south of the WIPP site and west in Nash Draw. A high-transmissivity zone penetrates the southern border of the WIPP site. This zone is important because it may represent a potential fast-path for WIPP contaminants.

Tracer tests and hydraulic tests at several hydropads indicate that the Culebra is vertically and areally heterogeneous at the hydropad scale. At some locations, the uppermost Culebra unit (CU-1) may minimally participate in flow and transport processes in the Culebra. At the H-19 hydropad, hydraulic tests indicate that the permeability of CU-1 is significantly lower than the permeability of the remaining Culebra units (Beauheim et al., 1997). Hydrophysical (fluid) logging at this location suggests that most fluid flow is through the lower Culebra units (COLOG, 1996). Tracer tests at the H-19 hydropad confirm that the upper portion of the Culebra does not significantly contribute to solute transport (Meigs et al., 1997; Beauheim et al., 1997; Meigs, 1996). Holt and Powers (1990) report that most of the Culebra flow into the WIPP AIS was from the lower Culebra units. Tracer and temperature surveys of the Culebra at the H-3 hydropad indicate that most of the flow occurred in the lower ~3 m (Mercer and Orr, 1979). At H-14, the permeability of the upper Culebra is slightly greater than the permeability of the lower Culebra (Beauheim, 1987) and is essentially the same as at H-19. This suggests that most spatial variation in Culebra transmissivity can be attributed to the lower Culebra units. Convergent-flow tracer tests have been conducted in the Culebra at four locations (H-3, H-6, H-11, H-19 hydropads) between 1981 and 1996 (Jones et al., 1992; Meigs et al., 1997). These tests showed that solute transport was strongly dependent on flow direction. At all hydropads tested, the fastest peak arrival time is not from the shortest travel distance; the slowest peak arrival time is not from the longest travel distance; or equidistant wells show different arrival times. This indicates that at these locations transport is through a heterogeneous and/or anisotropic medium (Meigs et al., 1997).

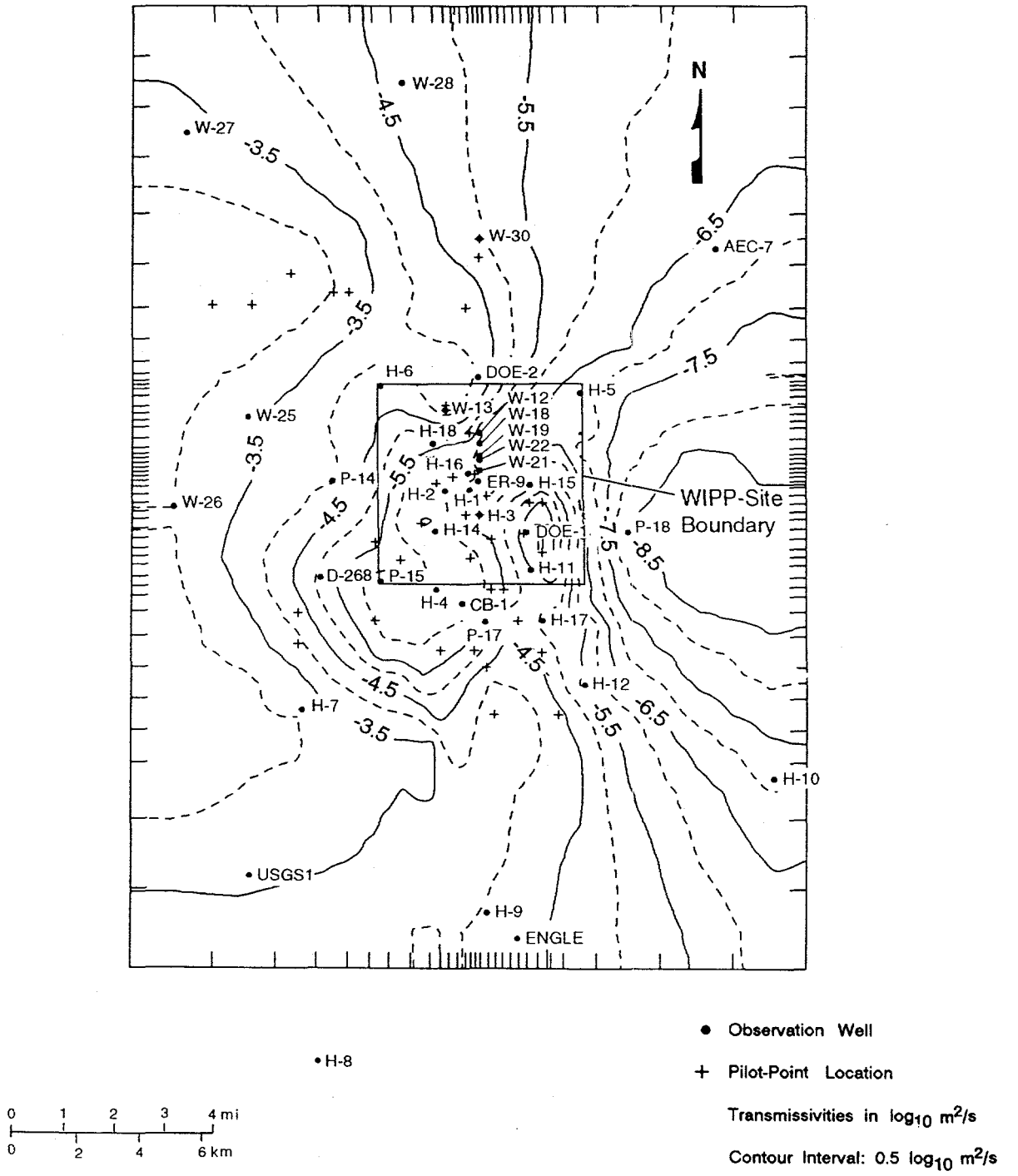

Figure 1-11. Spatial distribution of estimated transmissivity for the Culebra dolomite in the vicinity of the WIPP site (LaVenue et al., 1990).

2. HYDRAULIC CHARACTER OF THE CULEBRA

All transport processes in the Culebra, including chemical interactions with the solid materials, are controlled by the spatial distribution and nature of pore spaces within the Culebra, and porosity or pore size is an explicit or implicit parameter present in all mathematical descriptions of these processes. As such, a basic understanding of the types of porosity present and their vertical and spatial distributions is a basic component of any conceptual model for transport in the Culebra. Once the character of pore-space in the Culebra has been defined, relevant transport processes can be identified, and the conceptual link between these processes and Culebra porosity can be established.

The purpose of this section is to provide the conceptual linkage between Culebra porosity and transport processes; the linkage becomes a basis for developing a mathematical model for transport processes in the Culebra. Several steps are required to accomplish this objective. First, several categories of Culebra porosity will be defined and characterized, and laboratory measurements of relevant hydraulic properties on samples containing each porosity type will be reported. Second, the vertical distribution of the porosity types will be discussed in the context of the Culebra stratigraphy (Section 1.1). Third, transport processes expected to affect solutes moving through the Culebra are reviewed and conceptually linked to Culebra porosity types. Finally, this information will be used to construct an "idealized" representation of the Culebra at the H-19 hydropad.

Except where specifically referenced, the geologic information presented here represents a synthesis of data from core descriptions (Holt and Powers, 1988; Holt, 1996), RaaX video logs, petrographic description (Holt, 1996), and observations in WIPP shafts (Holt and Powers, 1984; 1986; 1990).

2.1 Culebra Porosity Types

Culebra porosity can be classified into intercrystalline porosity, interparticle porosity, fracture porosity, and vuggy porosity. These porosity types are conceptually depicted within the Figure 2-1 and described in detail below. The average values of porosity, formation factor, and horizontal and vertical hydraulic conductivity for laboratory samples containing each porosity type are shown in Table 2-1. The formation factor is a measure of the resistance of the sample containing an electrolytic solution divided by the resistance of an equivalent shape and volume of electrolytic solution (Appendix A). The values of these parameters for individual samples are contained in Appendix B. These data represent a compilation of recent samples from the H-19 hydropad and data from Kelley and Saulnier (1990). The porosity types present in the H-19 samples were determined by geological examination of the samples, and the porosity types present in the Kelley and Saulnier (1990) samples are interpreted from their geologic descriptions. In addition, estimated and average values of the specific surface area for each porosity type are presented in Table 2-2.

2.1.1 Intercrystalline Porosity

Within the well-indurated portions of the Culebra dolomite, intercrystalline porosity occurs (Figure 2-1) and is evident in thin sections and electron backscatter images (Plate 2-1).

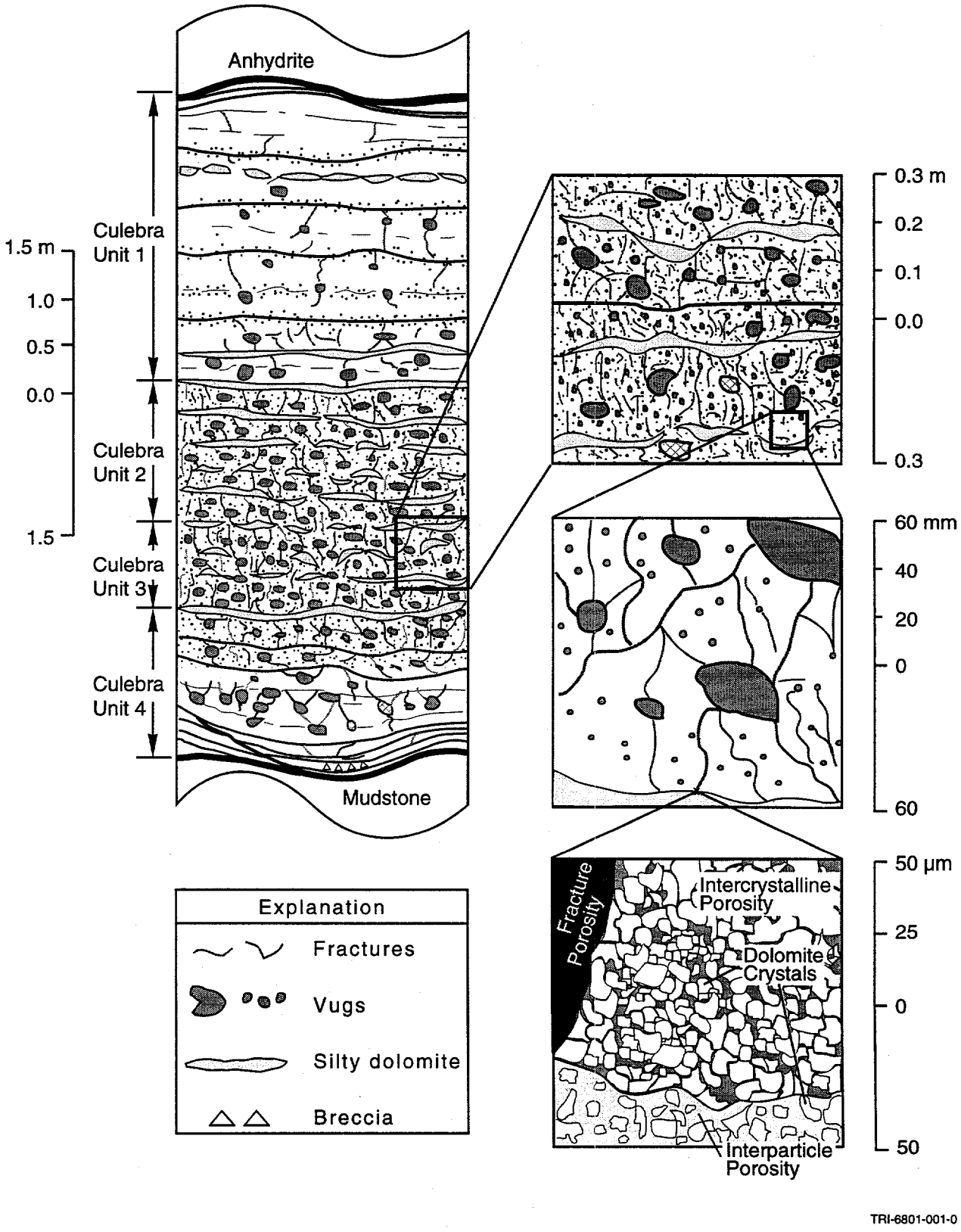

Figure 2-1. Scales of porosity in the Culebra.

Table 2-1. Hydraulic Properties of Samples Containing Culebra Porosity Types

Porosity Type	Mean Porosity	Mean Formation Factor	Median Hydraulic Conductivity (m/s)
Interparticle	0.22 (14)	27 (3)	2.1×10^{-8} (17)
Intercrystalline	0.11 (18)	111 (11)	4.0×10^{-10} (31)
Intercrystalline/vugs	0.15 (51)	104 (14)	2.3×10^{-9} (60)
Intercrystalline/vugs/fractures	0.16 (11)	77 (6)	3.9×10^{-8} (14)
Intercrystalline/fractures	0.11 (6)	266 (2)	3.8×10^{-8} (8)

Values in parentheses indicate number of samples. Data are contained within Appendix B.

Table 2-2. Mean Specific Surface Areas for Culebra Samples

Porosity Type	Specific Surface Area (m^2/gm)
Interparticle porosity	1.3 (8)
Intercrystalline porosity	1 (10)

Values in parentheses indicate the number of samples. Data are contained within Appendix C.

Descriptions of Culebra samples indicated that dolomite crystal sizes range from 0.5 μm (Sewards, 1991) to 30 μm and average between 5 μm and 15 μm. Crystals are typically equigranular mosaics of rhombic crystals. Intercrystalline pore spaces may range from < 1 μm to slightly larger than individual crystals. Pore spaces may occur along the margins of crystals and in crystal-size void spaces. Larger void spaces, between 50 and 100 μm, are probably the result of dissolution of microcrystalline gypsum, anhydrite, or dolomite crystals. The degree of interconnection between these pores is not clearly revealed by petrographic analysis, but because many of these pore spaces are adjacent to and sometimes clearly interconnected with other forms of porosity, it is likely that many of these pores are hydraulically interconnected. Furthermore, gypsum or anhydrite crystals within unfractured dolomite have been dissolved, creating microvugs; this dissolution could not have occurred in the absence of hydraulically connected intercrystalline porosity. Pathways through this interconnected intercrystalline porosity, however, are probably extremely tortuous.

Samples containing primarily intercrystalline porosity have the lowest median hydraulic conductivity (4.0×10^{-10} m/s) of all the types of porosity contained within the Culebra (Table 2-1). The mean porosity of these samples is 0.11, and the mean formation factor is 111 (Table 2-1). The average specific surface area of intact samples containing mainly intercrystalline porosity is 1.0 m^2/gm (Table 2-2).

2.1.2 Interparticle Porosity

Interparticle porosity in the Culebra occurs in clay- to silt-size materials (silty dolomite) (Figure 2-1 and 2-2). Qualitative macroscopic and microscopic observations (Plate 2-2) of silty dolomite suggest that the porosity is relatively high, and this is confirmed by measurements on samples where the average porosity is 22%. Interbeds (<1cm to ~15 cm thick) of poorly cemented, clay- to silt-size dolomite surrounded by more intact well-indurated dolomite occur primarily in the middle and upper parts of the Culebra (CU-1, CU-2, and CU-3) (Plate 2-3). In the middle part of the Culebra (CU-2 and CU-3), many of these interbeds are disrupted by

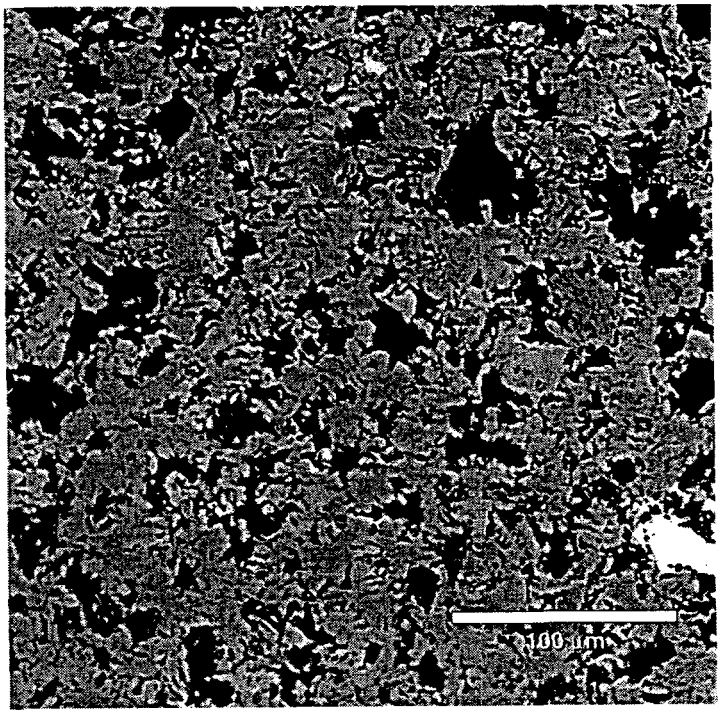

Plate 2-1. Backscatter electron image of Culebra dolomite from H-19b7, depth 752.2 ft. Dark areas are intercrystalline pore spaces filled with epoxy. Image courtesy of Charles Bryan.

soft-sediment deformation processes that occurred synchronously with their deposition (Plate 2-4). In some instances, the horizontal continuity of silty dolomite interbeds was completely destroyed, leaving only cm-scale, disconnected, irregular masses of silty dolomite. In the upper part of the Culebra (CU-1), silty dolomite interbeds show little soft-sediment deformation, are usually better cemented, and may contain coarser materials (silt and oolites). Some of these interbeds are areally persistent at the scale of a hydropad (e.g., H-19), and the silty dolomite interbeds in the upper part of the Culebra appear to persist for over 2 km.

In the past, the silty dolomite interbeds and zones in the middle parts of the Culebra (CU-2 and CU-3) acted as loci for fracturing. Strain from regional processes, including tectonics and unloading, is concentrated at these contacts because the contacts between the silty material and the well-indurated dolomite are very irregular (due to soft-sediment deformation) and the mechanical properties of the two materials are very different. As a result, small-scale fractures are abundant in the well-indurated dolomite surrounding interbeds and irregular masses of silty dolomite. In addition, thin sections from the wall-rock margins of some fractures and bedding-plane separations show dark, clay-size material with interparticle porosity.

Samples of silty dolomite containing interparticle porosity are moderately permeable with a median hydraulic conductivity of 2.1×10^{-8} m/s (Table 2-1). The formation factor of these samples is low and has an average value of 27. In thin section, silty dolomite appears to consist of the same type of dolomite material as the well-indurated dolomite, but it has not been cemented with dolomite. Individual silt-size grains consist of etched subhedral dolomite crystals and composite particles of etched crystals. These grains contain a small amount of internal pore space with a relatively high surface area to volume ratio. The average specific surface area of silty dolomite materials is 1.3 m^2/gm, which is larger than that measured for well-indurated dolomite containing intercrystalline porosity (Table 2-2). The high specific surface area reflects greater irregularities on the surfaces of the grains and microporosity within the grains.

2.1.3 Vugs

Vugs (open, roughly circular void spaces) are a common feature in the Culebra and occur within well-indurated dolomite (Figures 2-1, 2-2, and Plate 2-5). Vugs in the Culebra can be classified into two groups based on size. Small vugs, or microvugs, range from 1 mm to 4 mm in diameter (Plates 1-3 and 2-4), while larger vugs can range up to 4 cm in diameter. Nearly all open vugs in the Culebra formed from the dissolution of nodules or crystals of gypsum or anhydrite. Shortly after the Culebra was deposited, these nodules and crystals grew into and displaced the still soft Culebra sediments. Because the growth of these displacive features depended upon the supply of Ca^{+2} and SO_4^{-2} in the porewaters, displacive nodules and crystals tended to grow in the more permeable parts of the sediment. Permeable zones in unlithified Culebra sediment were concentrated along bedding planes and in the lower part of the Culebra (particularly CU-2 and CU-3) which was more disrupted by syndepositional slumping than was the upper part. Nodules acted as mechanical inhomogeneities during stress-field changes and became loci for fractures. These fractures allowed Culebra waters to access and dissolve the contents of the nodules, leaving open vugs. As a result, nearly all of the large vugs in the Culebra are connected to at least one fracture. Although it is difficult to observe macroscopically, many small vugs are also interconnected to fractures. Some small vugs, however,

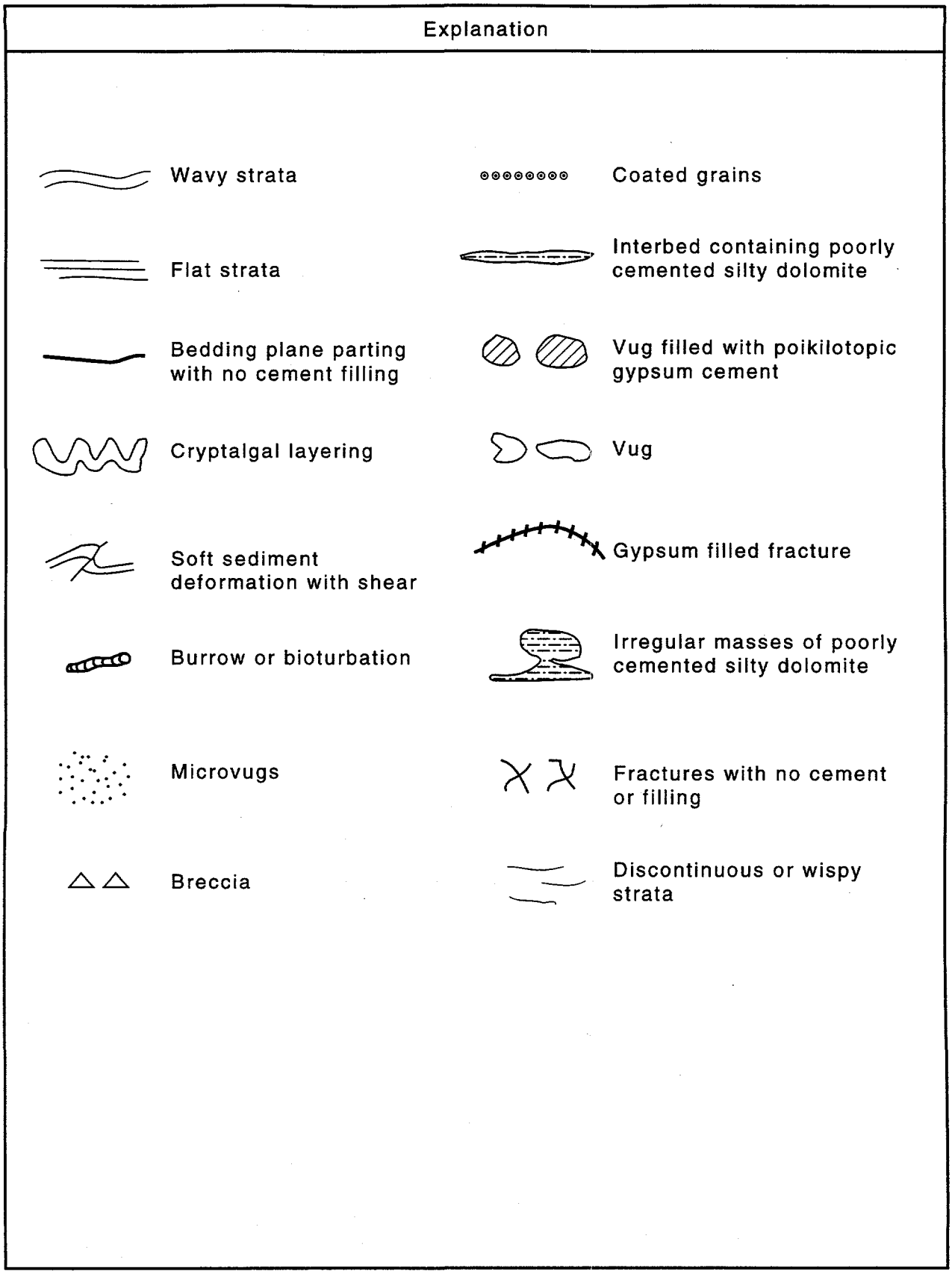

TRI-6801-41-0

Figure 2-2. Geologic description of the H-19b0 core.

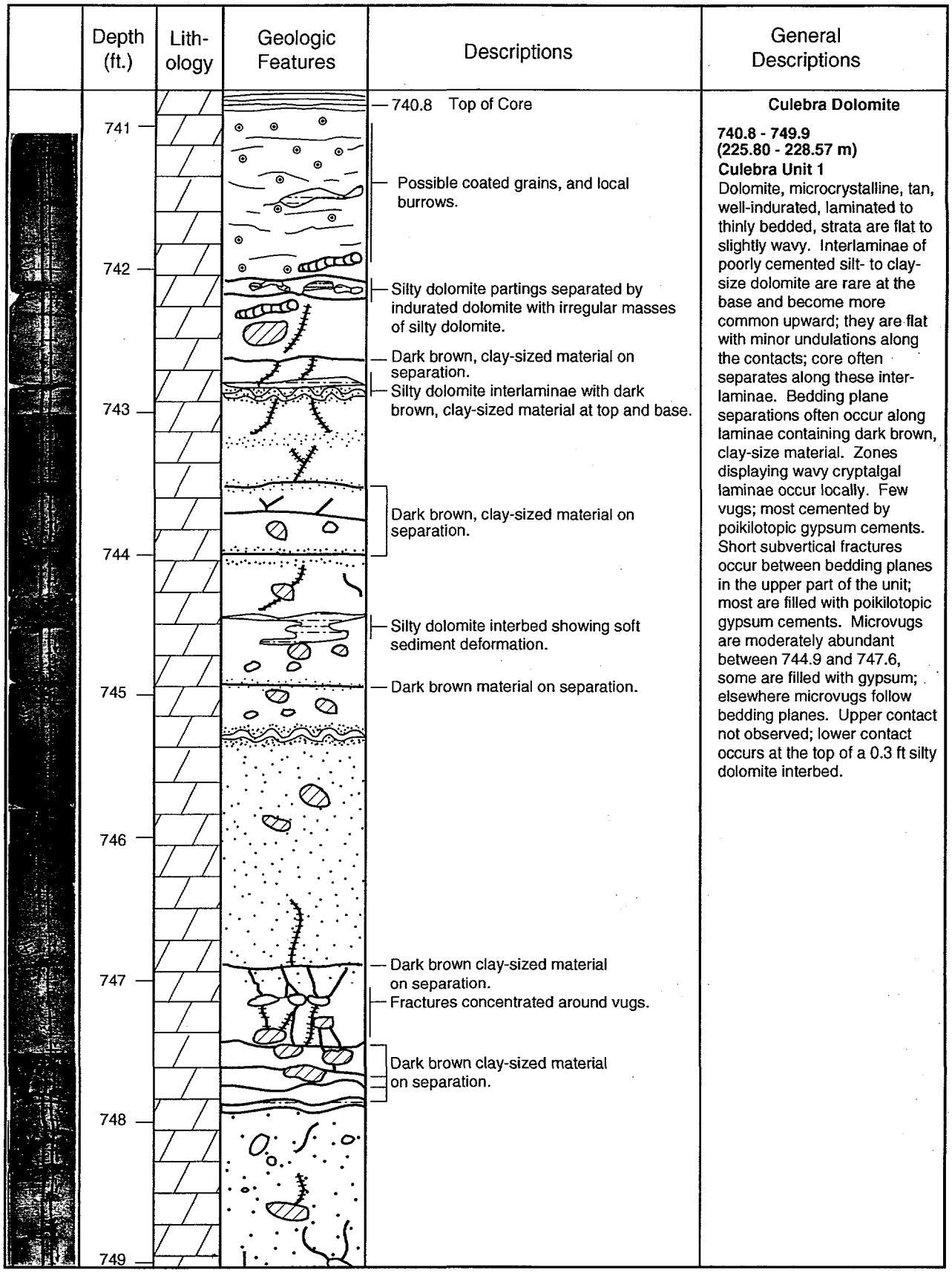

Figure 2-2. Geologic description of the H-19b0 core (continued).

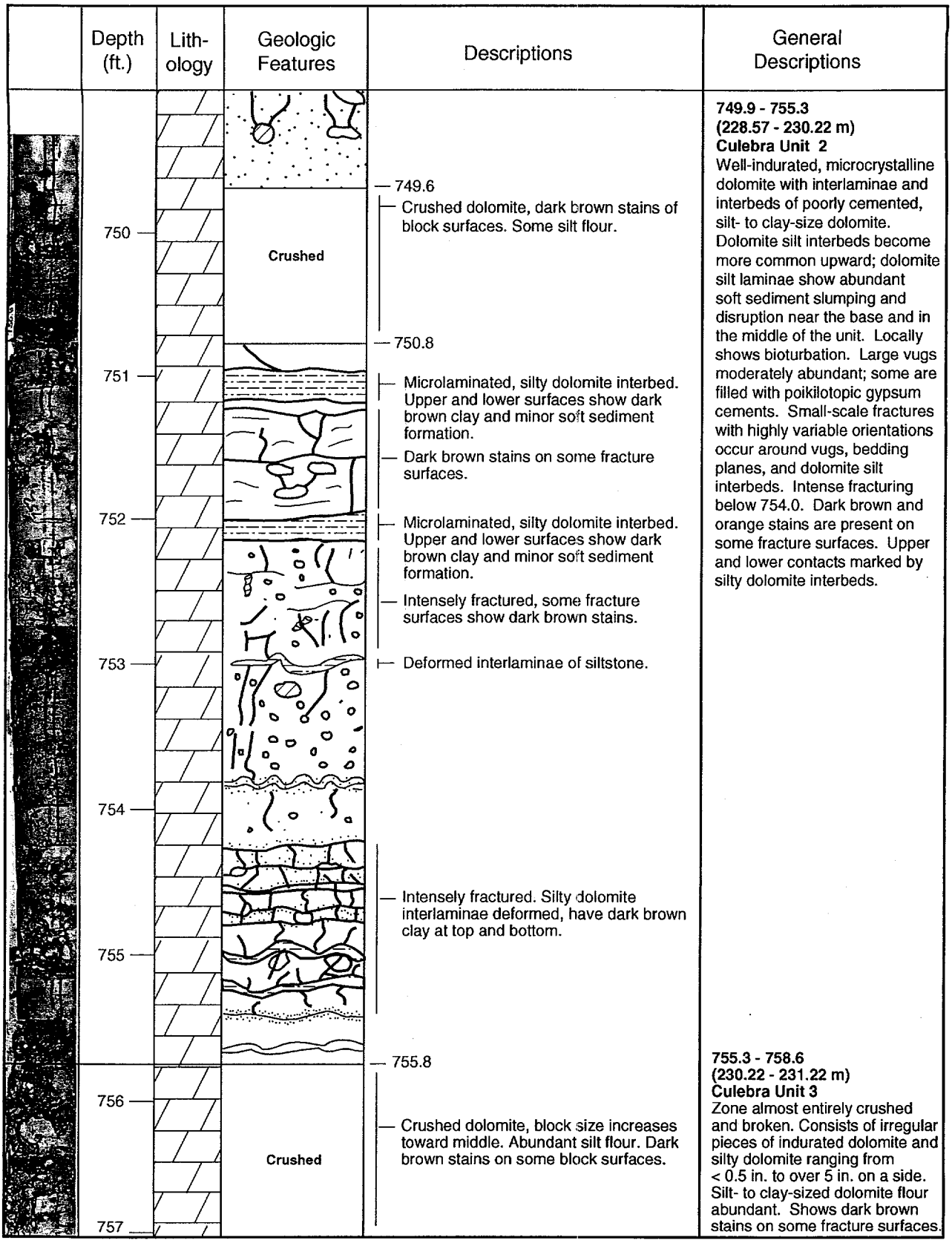

TRI-6801-23-0

Figure 2-2. Geologic description of the H-19b0 core (continued).

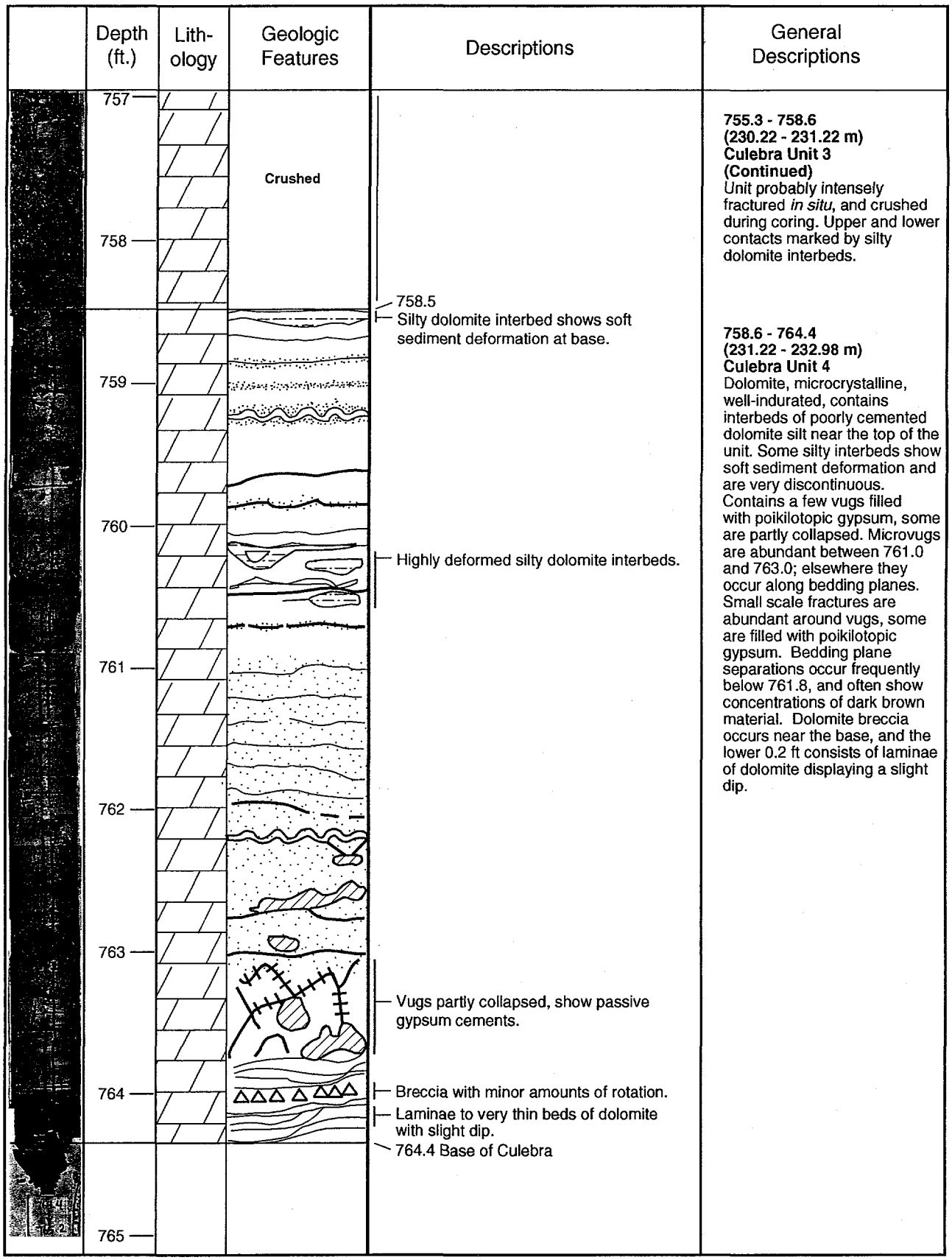

Figure 2-2. Geologic description of the H-19b0 core (continued).

TRI-6801-29-0

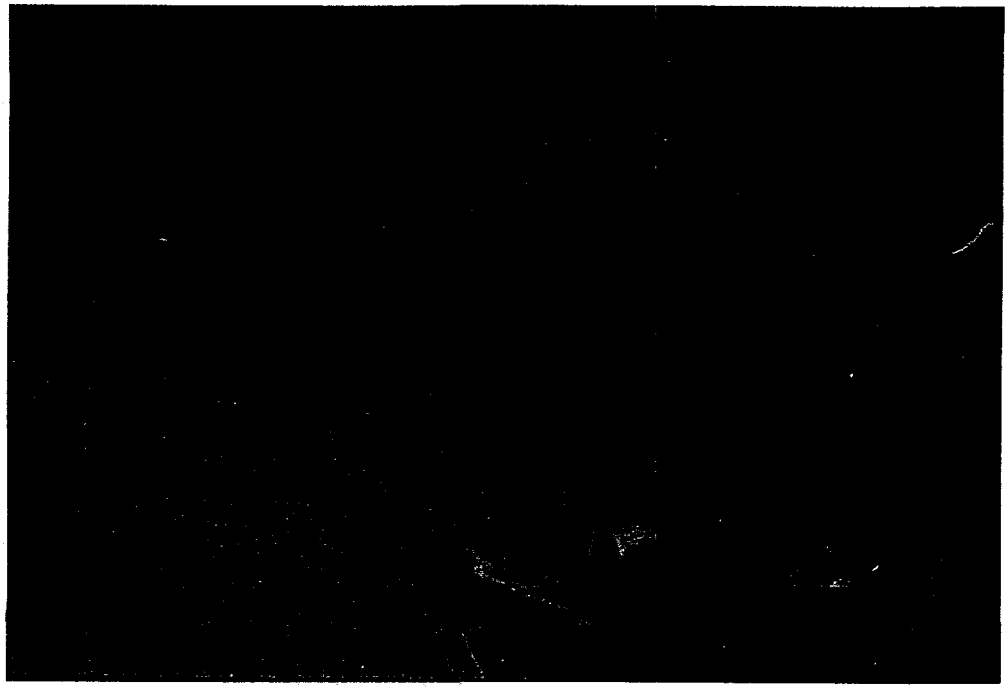

Plate 2-2. Photomicrograph of Culebra dolomite in cross-polarized light. Dolomite contains open fracture through an irregular region of silty dolomite containing interparticle porosity. Gypsum cements occur in some fractures. Note that the sample is impregnated with blue-stained epoxy, so that pore space appears blue. Scale bar equals 3.3 mm.

TRI-6801-30-0

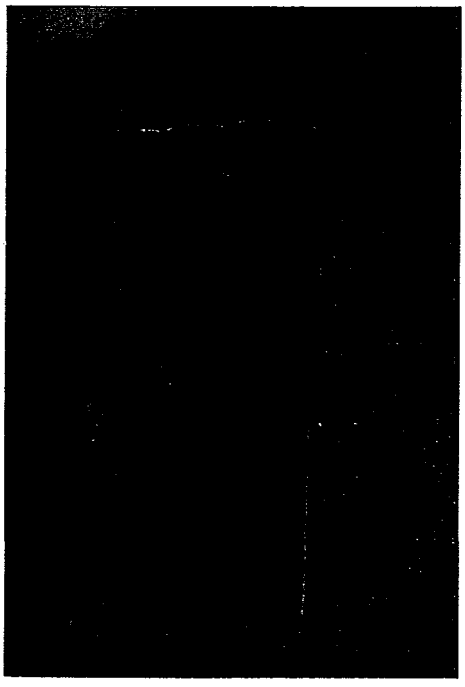

Plate 2-3. Silty dolomite interbed bounded by well-indurated dolomite. Small fracture-bounded blocks of well-indurated dolomite are concentrated near the lower boundary of the interbed. Larger subvertical fractures originate at the upper and lower boundaries of the interbed. Core width is ~5 cm.

TRI-6801-31-0

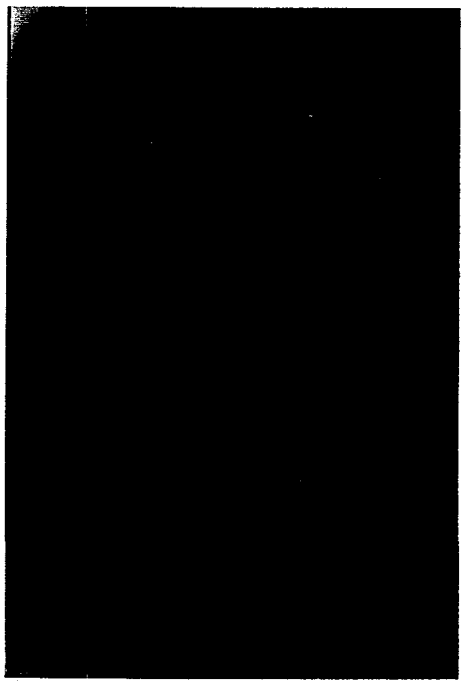

Plate 2-4. Irregular zones of silty dolomite bounded by well-indurated dolomite containing small vugs and microvugs. Discontinuous silty dolomite interbed near the base shows soft-sediment deformation. In the upper left, gypsum nodule occurs within irregular silty dolomite zone. Randomly-oriented microfractures interconnect some silty dolomite zones. Core width is ~5 cm.

do not appear to be interconnected to fractures. In these cases, small anhydrite or gypsum crystals were dissolved into fluids from interconnected, intercrystalline pore spaces. In addition, the margins of some of the vugs appear corroded in thin section, suggesting that some dolomite along their surfaces may have been dissolved by ground waters after the sulfate filling was removed.

As a porosity type, vugs and microvugs are interconnected with randomly oriented small-scale fractures, randomly oriented microfractures (Plate 2-6), and intercrystalline porosity. Therefore, they do not represent unique interconnected porosity types, and flow or transport through these features depends on interconnected fractures or intercrystalline porosity. This assertion is supported by the median values of hydraulic conductivity measured on samples. The median hydraulic conductivity for samples containing both intercrystalline and vuggy porosity is 2.3×10^{-9} m/s, slightly under one order of magnitude greater than the median value reported for samples containing only intercrystalline porosity (Table 2-1). The median value of hydraulic conductivity for samples containing intercrystalline porosity, vuggy porosity, and observable fractures is 3.9×10^{-8} m/s, over one order of magnitude greater than the samples without fractures (Table 2-1). This value is also essentially the same as reported from those samples containing intercrystalline porosity and fractures (with no vugs) (Table 2-1).

The mean porosity of samples containing both intercrystalline porosity and vuggy porosity is 0.15, while the mean porosity of samples described as containing both vugs and fractures is 0.16 (Table 2-1). Since the mean of samples containing only intercrystalline porosity is 0.11 (Table 2-1), it can be inferred that, on average, the presence of vugs increases the void volume by between 4% to 5%.

The mean formation factor of samples containing only intercrystalline porosity and vugs is 104 (Table 2-1), which suggests that the presence of vuggy porosity minimally affects the formation factor. When vugs and fractures are both present in samples, the mean formation factor is 77. This larger decrease in formation factor probably does not represent the presence of fractures alone but may also reflect the presence of larger vugs.

The specific surface area of samples containing both intercrystalline porosity and vugs has not been measured directly. The specific surface area for intercrystalline porosity with vugs ($S_{A,icv}$) can be approximated using the specific surface area for intercrystalline porosity ($S_{A,ic}$) and the average porosity for samples containing intercrystalline porosity (ϕ_{ic}) and intercrystalline porosity with vugs (ϕ_{icv}) using

$$S_{A,icv} = S_{A,ic}\left(\frac{1-\phi_{ic}}{1-\phi_{icv}}\right)\left(1+\phi_{ic}-\phi_{icv}\right) \qquad (2\text{-}1)$$

Equation 2-1 assumes that specific surface area of vugs is negligible. Using Equation 2-1, the specific surface area for intercrystalline porosity with vugs is approximated at 1.0 m^2/gm, essentially the same as intercrystalline porosity (Table 2-2).

2.1.4 Fractures

Fractures within the Culebra occur at a variety of scales (Figures 2-1 and 2-2). For the purposes of this discussion, a seven-element classification for these fractures is convenient. Bedding-plane partings are defined as large-scale (> 10 m), medium-scale (1 m to 10 m), and

TRI-6801-32-0

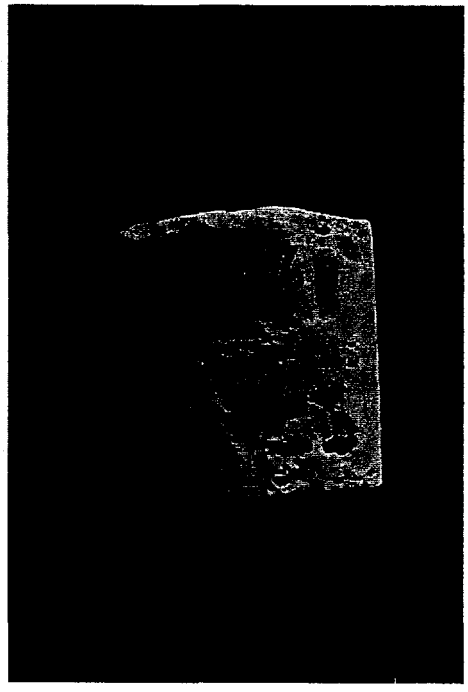

Plate 2-5. Vugs and open fractures in well-indurated dolomite. Open fractures interconnect some vugs. Core width is ~5 cm.

TRI-6801-33-0

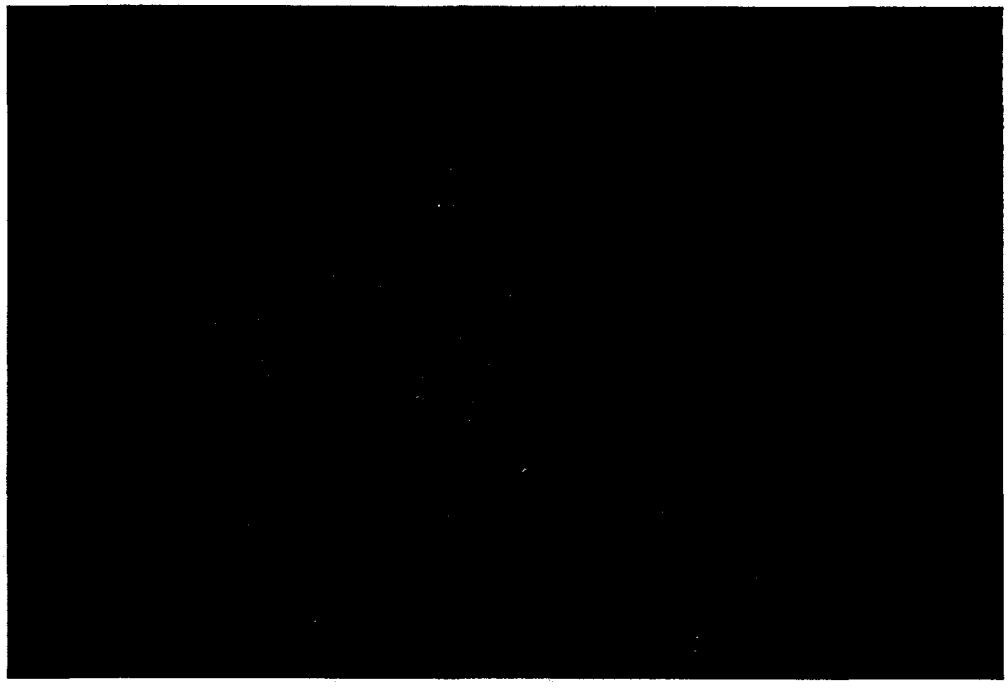

Plate 2-6. Photomicrograph of well-indurated dolomite containing microvugs and open microfractures in cross-polarized light. Some microfractures show connection with vugs. Irregular zone of laminated clay-size material in lower left corner of photomicrograph. Note that the sample is impregnated with blue-stained epoxy, so that pore space appears blue. Scale bar equals 3.3 mm.

small-scale (< 1 m). Subvertical fractures are subdivided into medium-scale (1 m to 3 m) and small-scale (0.2 m to 1 m). Randomly oriented fractures are subdivided into small-scale (0.05 m to 0.2 m) and microfractures (< 0.05 m). In general, the distribution of fracture scales in the Culebra is bimodal with most of the fractures being small-scale (Holt, 1996). Large-scale fractures, mainly bedding-plane fractures, are much less abundant but occur more frequently than medium-scale fractures. Culebra thin sections containing open and filled fractures indicate a possible range of fracture apertures from < 10 μm to 500 μm. Core samples from the Culebra frequently show fractures filled with poikilotopic gypsum with widths of > 2 mm.

Bedding-plane fractures are separations that develop along pre-existing planes of weakness formed at the top of strata (Figure 2-1 and 2-2). These planes of weakness exist because detrital material concentrated along some bedding-plane surfaces by depositional processes (e.g., settling of fine-grained materials and trapping of sediment by algal filaments) may not be adequately bridged by dolomitic cements. Separation occurs in response to regional unloading processes. In core, separations that occur along bedding planes and display either an orange or a dark stain on the separated surfaces are interpreted as natural bedding-plane fractures. Clay-size materials with interparticle porosity have been observed in thin sections of these bedding-plane partings. These bedding-plane fractures can extend the length of the individual bedding plane. Although individual strata within the Culebra, including those showing bedding-plane partings in core, can be traced for distances over 1 km; the areal persistence of bedding-plane fractures is unknown. Because strata in the uppermost part of the Culebra are relatively flat-lying and are not disrupted by soft-sediment deformation, large- to medium-scale bedding-plane partings are most common in CU-1. Large- to medium-scale bedding-plane partings do not occur in CU-2 and CU-3, because soft-sediment deformation has disrupted the bedding planes, and only small-scale bedding-plane partings occur in CU-2 and CU-3. Medium- to small-scale bedding-plane partings are common in CU-4 where the strata are undulatory with an amplitude of up to 0.5 m and a wavelength of ~1 m.

Subvertical, medium-scale fractures have been observed in WIPP shafts (Holt and Powers, 1990) and some Culebra cores. In most cases, these fractures are filled with gypsum cements. The areal extent of these fractures remains unknown. Some of these fractures follow medium-scale, subvertical, syndepositional slump planes (Holt and Powers, 1990), indicating separation along pre-existing planes of weakness. Swift (1992 [see Appendix D in current document]) found that some high-angle fractures in Culebra outcrops show a preferred orientation attributable to regional stress relief. Swift (1992) suggests that these patterns may be present in the subsurface at the WIPP. Fractures in the Culebra at WIPP shafts (Holt and Powers, 1984; 1986; 1990), however, do not show a preferred orientation, and it is not possible to reconstruct fracture orientations from Culebra cores. Thus, Swift's hypothesis is likely to remain untested.

Small-scale subvertical fractures are less common than fractures at other scales. Core and borehole video observations indicate that small-scale fractures are often subvertical and terminate at bedding-plane partings. The pressure response history of sinusoidal pumping tests in the Culebra at the H-19 hydropad suggest that the vertical connection between the upper (CU-1) and lower (CU-2, CU-3, and CU-4) parts of the Culebra varies spatially at the hydropad scale (Beauheim et al., 1997). Where a significant vertical connection is present, it is likely that flow is occurring, in part, along an interconnected series of subvertical small-scale and subhorizontal large-scale bedding-plane partings.

Randomly oriented small-scale fractures and microfractures are abundant in the Culebra, particularly in the lower Culebra units (e.g., CU-2 and CU-3) (Plate 2-7). In general, these fractures display no preferential orientation. These fractures are concentrated along and often interconnect obvious mechanical inhomogeneities within the dolomite, including, small syndepositional shear planes, collapsed and uncollapsed vugs, slumped and deformed interbeds of poorly cemented silty dolomite, and bedding planes (Plate 2-8). Because many mechanical inhomogenieties are closely spaced in the lower Culebra units, fracturing is intense in these zones, and fracture spacings and lengths range from less than 1 cm to several cm. Apparent block volumes range from 1 cm^3 to several cm^3 (Plates 2-8, 2-9, and 2-10). The apertures of individual fractures are highly variable. Some fractures show small amounts of displacement, particularly in the vicinity of collapsed large vugs. As large-scale fractures cannot propagate through an intensely fractured medium, no large-scale fractures are evident in zones containing abundant small-scale fractures. The surfaces of fractures often display concentrations of orange or dark minerals (possibly iron oxides or clay minerals) (Figure 2-2). Fractures that follow pre-existing shear planes often display dark, clay-size material that was transported or smeared along shear planes during syndepositional slumping. Thin sections of these features reveal the presence of interparticle porosity within the dark material.

Many fracture surfaces display dark or orange minerals (Figure 2-2). These stains and deposits frequently occur on the surfaces of fractures cemented with poikiolotopic gypsum, indicating that these materials pre-date the gypsum cements. Detailed descriptions of the H-19b7 core reveal that dark minerals are concentrated on approximately 7% of the total fracture surface area. Excluding CU-1, the total fracture surface area displaying dark minerals at H-19b7 is approximately 5%. A significant portion of the dark material concentrated at fracture surface is the clay mineral corrensite (Bryan,1996).

Samples of Culebra material containing fractures have the highest median hydraulic conductivity values, 3.8×10^{-8} m/s for samples containing intercrystalline porosity and fractures and 3.9×10^{-8} m/s for samples containing intercrystalline porosity, vugs, and fractures (Table 2-1). Because most reported field estimates of the vertically-averaged hydraulic conductivities for the Culebra exceed 1×10^{-8} m/s, it is likely that the vertically-averaged hydraulic conductivity of the Culebra is controlled by fractures with hydraulic conductivities that exceed the sampled median. The mean porosity of samples containing intercrystalline porosity and fractures is essentially the same as intercrystalline porosity, 0.11 (Table 2-1). This suggests that the volume associated with small fractures is negligible. The specific surface area of Culebra fractures and the dark, fine-grained materials sometimes present on their surfaces has never been directly measured. Although it is likely that clay-size materials concentrated on some fracture surfaces have a fairly large specific surface area, the specific surface area for fractures is considered negligible for the purposes of later discussions.

2.2 Vertical Distribution of Porosity Types

The Culebra can be subdivided into four Culebra units (CU) on the basis of lithologic character (Section 1.1). Although fractures are the most notable porous feature in each Culebra unit, the style and intensity of fracturing varies considerably among the units. CU-1 is dominated by bedding-plane fractures and local subvertical fractures that bound large tabular blocks. CU-2

TRI-6801-34-0

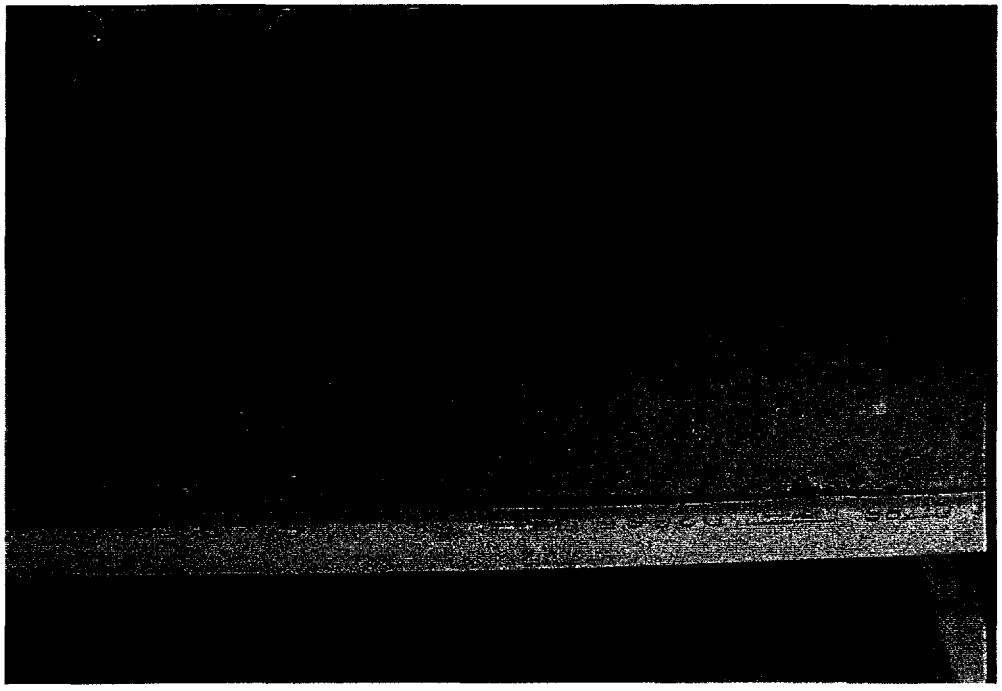

Plate 2-7. Subhorizontal core from CU-2 at the WIPP air intake shaft showing abundant, randomly oriented fractures with highly variable apparent block size. Vugs occur within well-indurated dolomite. Deformed very-thin bed of silty dolomite occurs in the lower right part of the core. Core diameter is ~14 cm.

TRI-6801-35-0

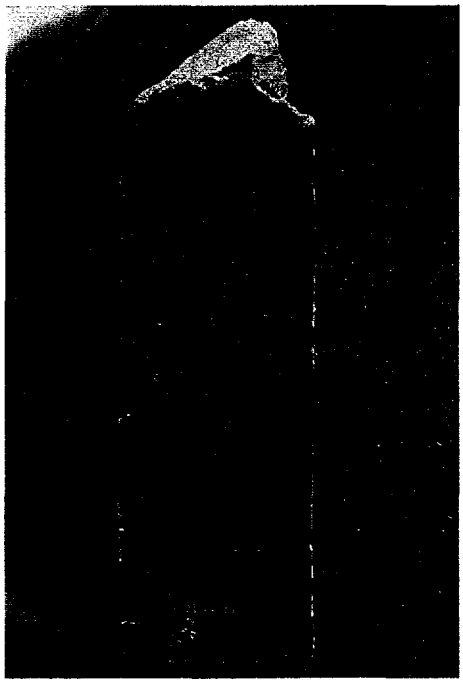

Plate 2-8. Brecciated and intensely fractured well-indurated dolomite with some clasts floating in silty dolomite. Clasts and fracture-bounded blocks of well-indurated dolomite vary significantly. Poikilotopic gypsum cements occur in the upper and lower third of the core. This fabric is interpreted to result from the collapse of large vugs. Core diameter is ~5 cm.

TRI-6801-36-0

Plate 2-9. Photomicrograph, in cross-polarized light, of partly brecciated well-indurated dolomite containing a few microvugs and open microfractures. Size varies from <1 mm to >10 mm. Orange stains occur along the boundaries of some clasts. Note that the sample is impregnated with blue-stained epoxy, so that pore space appears blue. Scale bar equals 3.3 mm.

TRI-6801-37-0

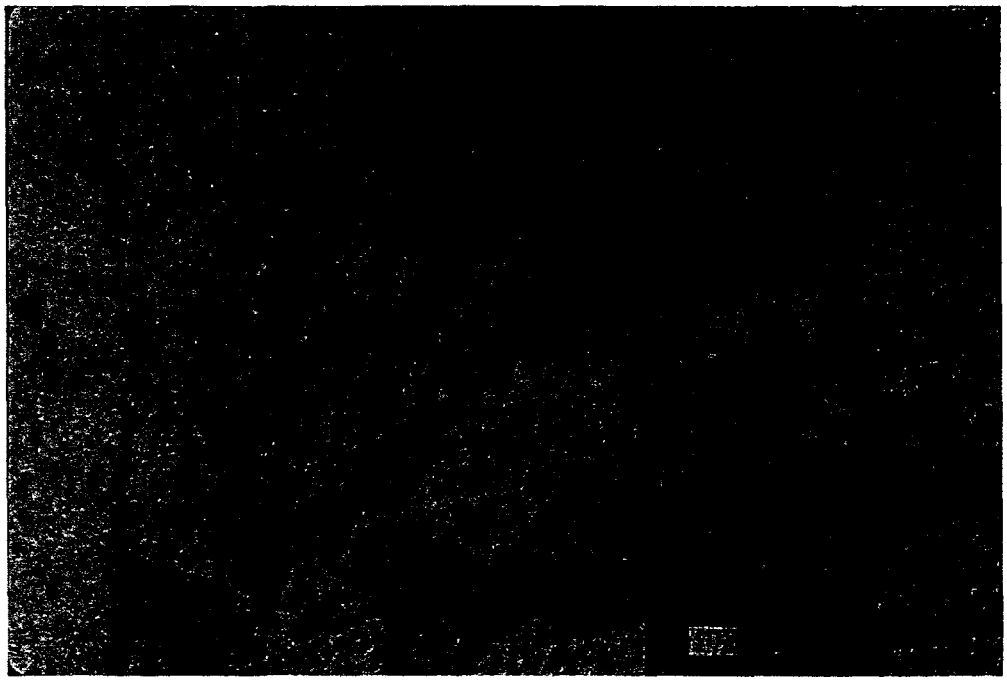

Plate 2-10. Photomicrograph, in cross-polarized light, of intensely fractured well-indurated dolomite containing a few microvugs and open microfractures. Some small fracture-bounded blocks appear to have more porosity than larger blocks. Note that the sample is impregnated with blue-stained epoxy, so that pore space appears blue. Scale bar equals 3.3 mm.

and CU-3 are intensely fractured with a hierarchy of superimposed block sizes. Although bedding-plane fractures are common in CU-4, they are of relatively short length and form medium-scale tabular blocks. CU-1 contains several continuous interbeds of silty dolomite near the top and base. CU-2 and CU-3 contain more abundant, thinner, and more discontinuous interbeds of silty dolomite, while CU-4 contains very little silty dolomite. In addition, vugs and microvugs are usually more abundant in CU-2, CU-3, and CU-4. All Culebra units contain intercrystalline porosity.

2.2.1 Culebra Unit 1

The hydraulic character of CU-1 is much different from the underlying Culebra units. Because CU-1 has suffered little syndepositional disruption, strata within the unit are continuous over much of the WIPP region. The porosity types present within CU-1 are summarized in Table 2-3. Bedding-plane partings are probably the most common form of fracture porosity within CU-1. They are spaced 10 cm to 60 cm apart. Small-scale subvertical fractures propagate from bedding plane to bedding plane. Large vugs are uncommon in CU-1; microvugs are common along bedding planes in some locations. Where gypsum fracture and pore fillings are minimal, open bedding-plane fractures may extend over large distances. Interbeds of silty dolomite occur near the top and base of CU-1 and are areally extensive and undisrupted. Microvugs and silty dolomite interbeds probably provide most of the porosity in CU-1.

Some inferences regarding the spatial connection of bedding-plane fractures and silty dolomite interbeds in CU-1 can be drawn from recent hydraulic test results at the H-19 well pad. Hydraulic tests at the H-19 well pad indicate that the upper portion of the Culebra (CU-1), which contains apparent bedding-plane fractures, is heterogeneous at the scale of the hydropad (i.e., there are several regions of very low permeability within the upper Culebra). This implies that the lateral interconnection of bedding-plane fractures and silty dolomite interbeds is weak and variable. The vertical connection between CU-1 and CU-2 depends on the presence of sufficient subvertical fractures. Hydraulic responses to sinusoidal pumping tests at the H-19 hydropad indicate that the vertical connection between CU-1 and underlying units is highly variable (Beauheim et al., 1997).

Networks of fairly widely spaced bedding-plane fractures interconnected with subvertical fractures and interbeds of silty dolomite probably provide most of the permeability in CU-1. Because bedding-plane fractures are discontinuous laterally, the permeability of CU-1 is limited by the vertical interconnection provided by widely spaced subvertical fractures. Reported vertically-averaged hydraulic conductivities for CU-1 range from 2×10^{-8} to 2×10^{-7} m/s (Beauheim, 1987; 1996). This range is consistent with median hydraulic conductivity of silty dolomite samples, 2.1×10^{-8}m/s (Table 2-1). It is likely that flow within CU-1 is dominated by silty dolomite interbeds and a few interconnected bedding-plane and subvertical fractures.

Randomly oriented microfractures and small-scale fractures are concentrated along some bedding planes and represent moderate permeability zones. Most of these permeable zones are aligned parallel to bedding planes with rare subvertical fractures cross-cutting the less permeable zones. Flow will be most restricted in low permeability zones consisting of highly elongated tabular blocks of well-indurated dolomite that vary from ~10 cm to ~1 m in thickness. Within the low permeability zones, intercrystalline and vuggy porosity interconnected to intercrystalline porosity is present.

Table 2-3. Distribution of Culebra Porosity Types within Culebra Units

Porosity Type	CU-1	CU-2 and CU-3	CU-4
Intercrystalline porosity	Abundant	Abundant	Abundant
Silty dolomite continuous interbeds interparticle porosity	Common near top and base of unit	Common near top of CU-2 and base of CU-3	Rare
Silty dolomite discontinuous interbeds interparticle porosity	Rare	Abundant	Rare
Silty dolomite blebs interparticle porosity	Rare	Common to abundant	Rare
Vugs: large to medium 3 mm – 10 cm	Rare	Abundant	Rare to common
Vugs: large collapsed vugs, 2 cm to 8 cm	Not observed	Rare to common	Rare
Microvugs <4 mm	Rare to common, depending on location	Common to abundant, depending on location	Rare to common, depending on location
Bedding-plane parting large-scale >10 m	Common, spaced 10 cm to 60 cm	Not observed	Not observed
Bedding-plane parting medium-scale 1 m – 10 m	Common, spaced 10 cm to 60 cm	Very rare	Rare, but potentially common in some locations
Bedding-plane parting small-scale <1 m	Common, spaced 10 cm to 60 cm	Common	Common.
Subvertical medium-scale gracture, 1 m – 3 m	Very rare	Very rare	Very rare
Subvertical small-scale fracture, 0.2 m – 1 m	Common, spaced 0.5 to >2 m	Common, spaced <0.5 m	Common, spaced 0.2 m to ~1 m
Randomly oriented fracture small-scale, 0.05 m – .2 m	Rare	Abundant, spaced <0.05 m to 0.2 m	Common, spaced <0.05 m to 0.5 m
Randomly oriented microfracture <0.05 m	Rare	Abundant, spaced <0.01 m to 0.2 m	Common, spaced <0.05 to 0.2 m

Data derived from core descriptions (Holt and Powers, 1988; Holt, 1996), RaaX video logs, and observations in WIPP shafts (Holt and Powers, 1984; 1986; 1990). Scale of bedding-plane fractures represents an interpretation based on the continuity of bedding-plane features.

2.2.2 Culebra Units 2 and 3

CU-2 and CU-3 are hydraulically very similar, except CU-2 contains thicker and more areally persistent silty dolomite interbeds. Because of extensive fracturing, CU-2 and CU-3 are well-interconnected hydraulically and often are not recovered in core. Core descriptions and RaaX video logs reveal the following types of porosity in CU-2 and CU-3 (Table 2-3): small-scale bedding-plane fractures, networks of randomly oriented small-scale fractures and microfractures, discontinuous silty dolomite interbeds, large vugs hydraulically connected with microfractures and small-scale fractures, microvugs hydraulically connected with microfractures and intercrystalline porosity, blebs of silty dolomite interconnected with microfractures and intercrystalline porosity, and intercrystalline porosity. Areally persistent interbeds of silty dolomite occur near the top of CU-2 and the base of CU-3. Between these zones, a dense fracture network is developed. Large-scale fractures are not found in CU-2 and CU-3 because these units are intensely fractured.

A complex hierarchy of fractures is evident at different scales. Randomly oriented microfractures are concentrated in the vicinity of vugs, microvugs, silty dolomite blebs, and bedding-plane fractures. Blocks bounded by microfractures typically range in size from ~1 cm to ~10 cm on a side, although smaller blocks of < 1 cm are common. On a slightly larger scale, randomly-oriented small-scale fractures often interconnect vugs, silty dolomite blebs, and bedding-plane surfaces. Small-scale fractures bound blocks that range from ~5 cm to ~20 cm and contain intercrystalline, vuggy, and microfracture porosity. When randomly oriented subvertical fractures are not extensive, a still larger scale of fractures is present. This largest scale is characterized by interconnected bedding-plane separations and small-scale subvertical fractures forming irregularly shaped, tabular blocks that are between 5 cm to 40 cm in thickness and may be several meters long. At any location, intercrystalline porosity and microvugs hydraulically connected to intercrystalline porosity occur within the smallest scale of fracture-bounded blocks.

Because of their abundance and high degree of interconnection, fractures probably contribute more to vertically-averaged hydraulic conductivity of CU-2 and CU-3 than do the other types of porosity. It is expected that lateral variations in the amount of fracturing and the degree of pore-filling gypsum cements varies on a scale of tens of meters. Thus, preferential flow occurs because of vertical and lateral variations in the amount of fracturing (heterogeneity), and local macrodispersion may be high. Abundant large vugs, microvugs, and silty dolomite interbeds give these units the highest total porosity in the Culebra. Although some silty dolomite interbeds are somewhat areally continuous and may provide some contribution to the volume-averaged permeability, flow through isolated masses of silty dolomite and large vugs is limited by fracture interconnections. Within CU-2 and CU-3, fracture-bounded blocks of well-indurated dolomite containing intercrystalline porosity, with or without connection to microvugs, have the lowest permeability.

Fluid logging results at the H-19 hydropad (Beauheim et al., 1997; COLOG, 1996) and observations in the AIS (Holt and Powers, 1990) suggest that at several locations CU-2 and/or CU-3 contribute most of the flow in the Culebra. This is not the case at all locations; hydraulic testing at H-14 suggests that CU-1 is the most transmissive unit in the Culebra (Beauheim, 1987).

2.2.3 Culebra Unit 4

Bedding-plane fractures are the dominant porous feature in CU-4 (Table 2-3). Bedding planes within CU-4 are typically undulatory on the scale of 1 m or more (Holt and Powers, 1990). Undulations have the greatest amplitude at the base of the unit, and the amplitude becomes damped upward. These undulations directly influence the style of fracturing in CU-4. Bedding-plane fractures terminate at the high points of these undulations, especially near the base of the Culebra. In some cases, the lowermost 0.3 m of the CU-4 is brecciated and displays randomly oriented small-scale fractures with blocks up to 15 cm on a side (Holt and Powers, 1986; Holt, 1996). Except where brecciated, most fracture blocks tend to be tabular, and the larger fracture blocks are at least 0.5 m to 1.0 m long and from 10 cm to 30 cm thick. Large collapsed vugs often occur within the lower 0.3 m (Holt, 1996). Thin interlaminae (1 to 2 cm thick) of silty dolomite occur near the top of CU-4. Intercrystalline porosity is common within the fracture-bounded blocks and is often interconnected with microvugs.

Although direct hydraulic testing of CU-4 alone has not been performed at any WIPP well, some inferences about its hydraulic character can be drawn from the geologic evidence. Where gypsum fracture-filling cements are minimal, fractures along bedding planes and with subvertical orientations probably form a relatively high-permeability network. This could be further enhanced in locations where brittle deformation of the dolomite along the lower contact of the Culebra is greatest. Microvugs and interbeds of silty dolomite provide most of the porosity within CU-4, but probably contribute little to its permeability as the microvugs are isolated features, poorly connected to fractures, and the silty interbeds are also discontinuous. Subvertical fractures in CU-4 suggest that the unit has a strong hydraulic connection to the overlying Culebra unit (CU-3).

2.3 Culebra Porosity and Solute Transport Processes

The physical transport processes expected to occur in the Culebra include advection, diffusion, and sorption. All of these processes are impacted by the character of porosity within the Culebra. The most important component of the modeling process is the conceptual link between flow and transport processes and the geologic medium. Prior to establishing the link between the medium and the physical components of transport, relevant transport processes must be identified. After relevant processes are identified, the influence the medium exerts on these processes can then be explored conceptually, and the role of each physical process within various portions of the medium can be postulated. This conceptual relationship between the medium and process provides the framework for creating a mathematical description of the expected transport processes. In this section, each of the transport processes expected to occur in the Culebra is reviewed, and the conceptual link between these processes and Culebra porosity is established.

2.3.1 Expected Transport Processes in the Culebra

All transport processes in the Culebra depend on pore size, pore shape, degree of interconnection between pores, and the spatial variation of these characteristics. The processes of advection, diffusion, and sorption are expected to be the most relevant to transport in the Culebra and are reviewed here. Advective processes are a function of the velocity of Culebra pore waters and, therefore, depend both on the character of Culebra porosity and the local

hydraulic gradient. The processes of diffusion and sorption are independent of the hydraulic gradient but, instead, primarily depend on the concentration gradient and the character of the pore-spaces containing water.

The physical transport of solutes by flowing ground water is considered advection. The processes of advection are related to the velocity of the water flowing through pores in the Culebra. Because the pore-water velocity is directly proportional to the local hydraulic conductivity, the magnitude of advective processes depends on the size of and degree of interconnection between pores within the Culebra. At the pore scale, the velocity of groundwater moving through a geologic medium varies considerably because of heterogeneity in pore size, shape, orientation, and degree of interconnection. As the solute is carried by moving water through the medium, these variations in velocity cause the solute to spread both in the direction of groundwater flow and perpendicular to average groundwater flow direction. This mechanical spreading process is referred to as dispersion. At a larger scale, additional spreading may occur as solutes are diverted around regions of low permeability and into zones of higher permeability. This effect from larger scales of heterogeneity is the process of macrodispersion. In general, the spreading attributed to macrodisperison increases as the variance of hydraulic conductivity increases.

The process of diffusion is independent of pore-water velocity. A solute in water will tend to move or diffuse from an area of greater concentration toward an area where it is less concentrated. Diffusion processes tend to spread a solute in the direction of lower concentration. Diffusion processes are active whenever a concentration gradient exists, even in flowing ground waters. The rate of diffusion is also related to the diffusion coefficient in the medium, or the apparent diffusion coefficient. The apparent diffusion coefficient for a solute will be smaller than its free-water diffusion coefficient, because diffusion cannot occur through the solid portions of the medium, diffusive pathways through the medium are tortuous, and sorption slows mass transport. The scale of solute movement and spreading by advective processes is usually several orders of magnitude greater than the spreading caused by diffusion, and the diffusion process can be neglected.

In portions of the Culebra where groundwater velocities are extremely low or absent, e.g., low-permeability regions or "dead-end" pores, groundwater may essentially be "immobile," and diffusion may be a primary mechanism for solute transport. If a large enough percentage of the total porosity is contained within low-permeability zones, solutes in porosity dominated by advection (advective porosity) can diffuse or slowly advect into the low-permeability zones (diffusive-porosity zones) significantly altering solute transport behavior. When this occurs, the zones of low-permeability material may act as a sink, or temporary storage place, for some of the solute. This process is referred to as physical retardation.

Some solutes may have a chemical affinity for materials present within the geologic medium. As solutes are transported into contact with these materials, they may be sorbed or attach to these materials. Sorption processes include adsorption, chemisorption, absorption, and ion exchange (Fetter, 1993). Adsorption occurs when the solute adheres to a solid surface. Chemisorption occurs when the solute is incorporated by chemical reaction onto the surface of the medium. Absorption occurs when solute is sorbed onto interior surfaces of minerals or particles. Ion exchange occurs when ions in the medium are replaced by some solute ions. Because these phenomena are difficult to measure and quantify in a geologic medium, they are lumped together and treated as generic "sorption" processes.

When the rate of sorption is slow relative to the rate of solute transport, sorption must be modeled as a rate-limited, or non-equilibrium process. Sorption processes that occur very rapidly relative to the time scale of solute transport can be considered as occurring instantaneously and are modeled by equilibrium sorption isotherms. In some cases, the amount of solute sorbed onto a medium shows equilibrium behavior and varies linearly with the concentration of solute in the liquid. When this happens the equilibrium sorption processes are considered linear and are described by the slope of the sorbed versus aqueous concentrations (the parameter K_d). As sorption is usually a surface reaction, the amount of sorption that will occur is proportional to the amount of reactive surface area accessible to the solute.

2.3.2 Role of Culebra Porosity in Transport

In this section, the link is established between Culebra porosity types and potential transport processes. Advective and diffusive porosity types are identified on the basis of their hydraulic conductivity values. The probable sorption behavior for advective and diffusive porosity types is discussed.

Because regions with high hydraulic conductivity bound zones with low hydraulic conductivity, pore-water velocities are likely to be bimodally (possibly multimodally) distributed in the Culebra. Advective processes are likely to dominate transport within the high hydraulic conductivity regions, while diffusion is likely to be more important in the low peremability zones. The hydraulic conductivity values reported from hydraulic tests of WIPP wells represent a vertical and spatial average of the hydraulic conductivity of all porosity types present around the well. Advection probably dominates transport processes in Culebra porosity types with hydraulic conductivities greater than roughly one order of magnitude less than the hydraulic conductivity reported for a Culebra well.

Samples containing interparticle porosity (silty dolomite) and intercrystalline porosity with fracture porosity (fractured, well-indurated dolomite) have relatively high hydraulic conductivities, with median values ranging from 2.1×10^{-8} m/s to 3.9×10^{-8} m/s (Table 2-1). These values are within one order of magnitude of most reported hydraulic conductivity values for Culebra wells. It is assumed that, where the Culebra hydraulic conductivity is about 3×10^{-7} m/s or less, most interparticle porosity and all fracture porosity are dominated by advective processes and are considered advective porosity. Evidence for this may be found in Culebra hydraulic tests that show double-porosity hydraulic response and a high storativity ratio. In these locations, silty dolomite, containing approximately 22% interparticle porosity, may respond to pressure changes on about the same time scale as fracture porosity, causing the apparent "fracture" storage coefficient to be larger. Interparticle porosity, small-scale fractures, and microfractures may not always participate in advective processes. At Culebra wells with interpreted hydraulic conductivity values greater than 3×10^{-7} m/s, some regions containing silty dolomite and small-scale fractures may be bypassed by preferential flow.

Culebra core samples containing intercrystalline porosity and intercrystalline porosity with vugs have relatively low hydraulic conductivities (Table 2-1). These porosity types are considered to be diffusive porosity, because pore-water velocities will be much smaller in these materials than in more conductive materials and diffusion may be a significant mechanism for solute transport. In addition, interparticle porosity and microfractures that are bypassed by preferential flow may locally act as diffusive porosity. Zones of diffusive porosity within the

Culebra are contained within blocks bounded by fractures that participate in advection. These diffusive-porosity zones greatly vary in size and volume, as the length dimensions of fracture-bounded blocks within the Culebra vary from a sub-millimeter scale to over 50 cm, with a myriad of scales in between.

Based upon the results of batch sorption isotherm tests on relatively clay- and iron oxide-free Culebra dolomite samples, actinides, except americium, have been shown to have a moderate tendency for sorption on Culebra dolomite and can be shown to follow a linear sorption isotherm (Brush, 1996). Because sorption is a surface reaction, the K_d for a particular solute will vary with the surface area of the pore spaces in a geologic medium. Batch K_d values can be applied in the field only when the medium has essentially the same specific surface area as the samples used in the batch experiments. Samples used in Culebra batch sorption isotherm experiments have an average specific surface area of 1.53 m^2/gm (Appendix C). Because the specific surface area of intact samples of Culebra dolomite range from 0.5 to 2.6 m^2/gm (Appendix C), K_d values determined from the batch experiments are appropriate for modeling chemical sorption in diffusive porosity within the Culebra.

Under most circumstances, the specific surface area per unit mass of the advective porosity will be smaller than the specific surface area of the diffusive porosity. In a chemically homogeneous rock, therefore, we should expect that more sorption will occur in the diffusive porosity. Advective porosity within the Culebra is not, however, chemically homogeneous. Clay minerals (e.g., corrensite) and iron oxides occur along fracture surfaces in the Culebra and have a greater sorption potential for actinides than does dolomite (Lappin et al., 1989). Culebra diffusive porosity is chemically more homogeneous than the fracture surfaces, because clays and iron oxides are less abundant and more widely distributed. During later calculations (Sections 4 and 5), however, it is assumed that the Culebra is chemically homogeneous and sorption occurs only on dolomite.

2.4 Idealized Hydrogeologic Framework for the Culebra at the H-19 Hydropad

At a location where geologic information is relatively complete, the linkages established between transport processes and Culebra porosity types can be used to construct an idealized hydrogeologic framework. Using location-specific geologic information regarding the distribution and amount of each porosity type present in each Culebra unit, advective porosity for each unit can be estimated, and diffusive-porosity zones of different scales defined. The result is a location-specific hydrogeologic framework that can be used to conceptualize transport processes.

In the following discussion, a hydrogeologic framework is constructed for the Culebra at the H-19 hydropad (see Figure 1-10 for the location of the H-19 hydropad). The H-19 hydropad was chosen because of its relevance to recent tracer tests and the high quality of core recovered from wells on the hydropad. The geologic description and photographs of the core from H-19b0 provided the basis for this effort (Figure 2-2). From the core photographs and descriptions, the percentage of each unit containing intercrystalline porosity, intercrystalline porosity with vugs, and interparticle porosity is estimated. Several average fracture-bounded block sizes are identified. Average fracture-bounded block sizes are selected to most simply represent the character of each Culebra unit. The number of average block sizes could be increased by defining new block ranges and estimating the percentage of each from H-19b0 core photographs.

For this exercise, no vertical or spatial variations are considered within Culebra units, and all diffusive porosity zones are considered to be equally well connected to advective porosity. Relevant aspects of the geology of the Culebra at the H-19 hydropad are discussed below.

At the H-19 hydropad, the advective porosity within CU-1 consists of bedding-plane fractures interconnected to subvertical fractures that extend from bedding plane to bedding plane and silty dolomite interbeds near the top and base of the unit. Advective porosity also includes smaller-scale fractures. Advection in CU-1 is expected to be dominantly horizontal along high permeability features. Diffusive porosity consists of well-indurated dolomite containing intercrystalline porosity and intercrystalline porosity connected to microvugs. Examination of the H-19b0 core reveals that approximately 18% of CU-1 consists of silty dolomite.

Intercrystalline porosity occupies roughly 57% of the diffusive porosity in CU-1 and can be subdivided into three different average block sizes. Roughly 7% of the intercrystalline porosity is contained within angular blocks that are less than 4 cm across. Approximately 54% of the intercrystalline porosity is located in tabular zones about 10 cm thick, and about 38% of the intercrystalline porosity occurs within tabular zones 30 cm thick. Intercrystalline porosity containing vugs occupies 25% of CU-1 and occurs in tabular zones roughly 30 cm thick.

Advective porosity within CU-2 and CU-3 consists of a complex network of small-scale bedding-plane fractures, subvertical fractures, randomly oriented fractures, fractures that interconnect vugs, and interbeds and zones of silty dolomite. In the H-19b0 core, approximately 28% of CU-2/CU-3 consists of silty dolomite.

In CU-2/CU-3, diffusive porosity includes intercrystalline porosity and intercrystalline porosity with vugs. Intercrystalline porosity occupies roughly 38% of CU-2/CU-3. About 45% of the intercrystalline porosity is contained within angular fracture-bounded blocks less than or equal to 2 cm across. The remaining 55% of intercrystalline dolomite occurs within larger, ~5-cm-wide, angular blocks of intercrystalline dolomite. Intercrystalline dolomite containing vugs occupies 34% of CU-2/CU-3. It is contained within angular blocks ≤ 2 cm wide (23% of all intercrystalline dolomite with vugs), angular blocks ~10 cm wide (33% of all intercrystalline dolomite with vugs), and tabular blocks ~20 cm thick (44% of all intercrystalline dolomite with vugs).

Advective porosity within CU-4 consists of a network of medium-scale bedding-plane fractures, medium-scale subvertical fractures, local small-scale fractures and microfractures, and rare irregular zones of silty dolomite. Silty dolomite occupies approximately 6% of CU-4.

Diffusive porosity within CU-4 consists of intercrystalline porosity and intercrystalline porosity with vugs. Well-indurated dolomite containing intercrystalline porosity occupies roughly 36% of CU-4 and is contained within angular blocks ≤ 4 cm on a side (17% of intercrystalline porosity) and tabular blocks ~10 cm thick (83% of intercrystalline porosity). Dolomite containing intercrystalline porosity and vugs is contained within approximately 58% of CU-4. Dolomite containing intercrystalline porosity and vugs is occurs within tabular blocks 10 cm (31%) and 30 cm (69%) thick.

For each Culebra unit, estimates of advective porosity and definitions of diffusive-porosity zones are presented in Table 2-4 and Table 2-5, respectively. Bulk densities for zone j, advective porosity or a diffusive porosity zone, are calculated using

$$\rho_{b,j} = \rho_d\left(1-\phi_j\right) \tag{2-2}$$

where ρ_d is the Culebra grain density, assigned to be 2.82 gm/cm^3 (Kelley and Saulnier, 1990), and ϕ_j is the porosity of zone j. Advective porosity is characterized by several estimated parameters. First, the total advective porosity for the unit is estimated by scaling the interparticle porosity (Table 2-1) by the fraction of silty dolomite present in the unit. This assumes that the contribution of fracture porosity to the advective porosity is negligible when compared to the porosity contribution from silty dolomite. Second, an advective bulk density is estimated using Equation 2-2. Since the specific surface area of fractures is assumed to be negligible, the specific surface area of the advective porosity is estimated using

$$S_{A,a} = \frac{S_{A,ip} f_{ip} \rho_{b,ip}}{\rho_{b,a}} \tag{2-3}$$

where $S_{A,ip}$ is the specific surface area of the interparticle porosity (L^2/M) (Table 2-2), f_{ip} is the fraction of the unit containing silty dolomite, $\rho_{b,ip}$ is the bulk density of the interparticle porosity, and $\rho_{b,a}$ is the bulk density of the advective porosity.

Diffusive-porosity zones are defined (Table 2-5) on the basis of (1) the porosity type contained within the zone, (2) the average half-block size associated with the zone, (3) the total porosity of the diffusion zone (void volume in diffusive zone/total volume of the unit), (4) an idealized geometry for the zone, (5) a specific surface area for the zone, (6) the formation factor of the porosity type within the zone, and (7) the bulk density of the material within the zone. Porosity types and half-block sizes are determined by geologic description. The total porosity of the diffusion zone is calculated by scaling the porosity of the diffusion zone porosity type (Table 2-1) with the fraction of the unit containing the diffusive porosity zone. The idealized geometry used for tabular zones and blocky zones is considered layered and spherical, respectively. The formation factor and specific surface area for a diffusive porosity zone is considered to be the average sample value reported for the porosity type contained within the zone (Tables 2-1 and 2-2). The bulk density for each zone is estimated using Equation 2-2.

Table 2-4. Estimated Hydraulic Parameters for Advective Porosity in Culebra Units at the H-19 Hydropad

	CU-1	**CU-2/CU-3**	**CU-4**
Advective porosity	0.04	0.06	0.01
Specific surface area (m^2/gm)	0.2	0.3	0.06
Advective bulk density (gm/m^3)	2.71×10^6	2.64×10^6	2.78×10^6

Table 2-5. Estimated Hydraulic Parameters for Diffusive Porosity Zones at the H-19 Hydropad

Culebra Unit	Porosity Type	Half-Block Size (m)	Geometry	Diffusive Porosity	Specific Surface Area (m^2/gm)	Bulk Density (gm/m^3)	Formation Factor
CU-1	Intercrystalline	0.02	spherical	0.004	1	2.81×10^6	111
	Intercrystalline	0.05	layered	0.034	1	2.72×10^6	111
	Intercrystalline	0.15	layered	0.024	1	2.75×10^6	111
	Intercrystalline/ vugs	0.15	layered	0.038	1	2.71×10^6	104
CU-2/ CU-3	Intercrystalline	0.01	spherical	0.019	1	2.77×10^6	111
	Intercrystalline	0.05	spherical	0.023	1	2.76×10^6	111
	Intercrystalline/ vugs	0.01	spherical	0.012	1	2.79×10^6	104
	Intercrystalline/ vugs	0.05	spherical	0.017	1	2.77×10^6	104
	Intercrystalline/ vugs	0.1	layered	0.022	1	2.76×10^6	104
CU-4	Intercrystalline	0.02	spherical	0.007	1	2.80×10^6	111
	Intercrystalline	0.05	layered	0.033	1	2.73×10^6	111
	Intercrystalline/ vugs	0.05	layered	0.027	1	2.74×10^6	104
	Intercrystalline/ vugs	0.15	layered	0.060	1	2.65×10^6	104

In general, CU-1 is interpreted to have an advective porosity of 0.04 and to contain primarily layered diffusive porosity zones from 10 cm to 30 cm thick. CU-2/CU-3 has an estimated advective porosity of 0.06 and primarily spherical diffusive porosity zones from 2 cm to 10 cm in diameter. CU-4 has an estimated advective porosity of 0.01 and contains mainly layered diffusive porosity zones from 10 cm to 30 cm thick. It is important to note that the definitions of the diffusive zones are examples that are intended to preserve the general geologic character of each Culebra unit. The number of diffusive zones could be increased to provide greater resolution of diffusive porosity zones.

The approach demonstrated in this section illustrates how detailed geologic information can be used to construct a quantitative tie between geology and transport processes in a hydrogeologic framework. This approach can be applied at other locations where Culebra geologic data are sufficient. Although the hydrogeologic framework presented here applies only to the H-19 hydropad, some generalizations to other locations can be made. Because Culebra

units have excellent stratigraphic continuity across the WIPP area, the proportions of each porosity type observed in Culebra units at the H-19 hydropad are likely to be representative of the WIPP area.

Where the Culebra displays a transmissivity much higher than at the H-19 hydropad (Figure 1-10), the increase in transmissivity is probably due to the presence of more areally extensive fracture networks within CU2, CU3, and CU4. Areally extensive fracture networks may act as fast paths that bypass other portions of the Culebra, and smaller-scale fractures and some silty dolomite zones may best be considered as diffusive porosity. It is likely that the fracture density in Culebra units at these locations is similar to or larger than at the H19 hydropad.

Where the Culebra displays a transmissivity much lower than at the H-19 hydropad (Figure 1-10), fewer well-interconnected fracture networks are present, and most advection occurs through silty dolomite zones. Where gypsum cements are not extensive, the advective porosity for each Culebra unit is likely to be similar to the estimates for the H-19 hydropad. Where gypsum cements are extensive, it can be assumed that gypsum cements reduce all porosity uniformly, and ratios of diffusive to advective porosity will remain about the same within Culebra units. Where transmissivities are lower than at the H-19 hydropad, fewer fractures are present because overburden thickness is greater or more gypsum cements fill fractures. In either case, the size of fracture-bounded blocks will increase as the number of fractures is reduced.

3. MATHEMATICAL MODEL FOR SOLUTE TRANSPORT IN THE CULEBRA

3.1 Multiple-Rate, Double-Porosity Model

Transport processes in the Culebra are expected to be very complex. Advection is expected to be the dominant process in fractures and, in many locations, silty dolomite interbeds. These feature are heterogeneously distributed both vertically and horizontally through the Culebra. The vertical scale of heterogeneity changes at the boundaries of Culebra units, and it is expected that advective processes are most similar within individual Culebra units. The horizontal scales of heterogeneity within units remain unknown, but they are probably greater than the unit thickness. Fracture-bounded blocks of dolomite within each of these units contain intercrystalline porosity and intercrystalline porosity with vugs, vary greatly in size and shape, and are heterogeneously distributed vertically through the Culebra at a scale roughly defined by the boundaries of Culebra units. Within these blocks, diffusion is probably an important mechanism for solute transport. Because advectively-dominated porosity is chemically inhomogeneous, sorption processes are expected to be complicated. The level of complexity present in the Culebra cannot be practically incorporated into an advection-dispersion transport model. Therefore, an alternative model that is easier to construct and preserves the physical behavior of transport processes expected in the Culebra must be selected.

A multiple-rate, double-porosity transport model preserves the physical behavior of expected transport processes in the Culebra. Multiple-rate, double-porosity models differ conceptually from the classic single-rate, double-porosity model (Figure 3-1). In a single-rate double-porosity model, diffusion is assumed to occur into only one diffusive-porosity zone described by a constant size, geometry, and diffusion characteristics. A multiple-rate model is more general, because it allows diffusive mass transfer into a number of diffusive-porosity zones of varying size, geometry, and diffusion characteristics. In the absence of chemical decay or non-sorption chemical reaction, a double-porosity, multiple-rate model with equilibrium chemical sorption and diffusion in and out of N zones of diffusive porosity can be expressed as (Haggerty and Gorelick, 1995)

$$\frac{\partial C}{\partial t} + \sum_{n=1}^{N} \beta_n^* \frac{\partial C_n^*}{\partial t} = \nabla \bullet \left(\frac{\mathbf{D}}{R} \nabla C \right) - \frac{\mathbf{v}}{R} \nabla C \qquad (3\text{-}1)$$

where C [M/L^3] is the aqueous concentration in the advective porosity, C_n^* [M/L^3] is the aqueous concentration in the diffusive-porosity zone n, $\mathbf{D}$ [L^2/T] is the hydrodynamic dispersion tensor, $\mathbf{v}$ [L/T] is the average pore-water velocity in the advective porosity, and R [dimensionless] is the retardation coefficient due to equilibrium chemical sorption in the advective porosity. The term β_n^* [dimensionless] is a capacity coefficient. In this model, it is important to note that all N diffusive porosity zones are assumed to have equal access to advective porosity.

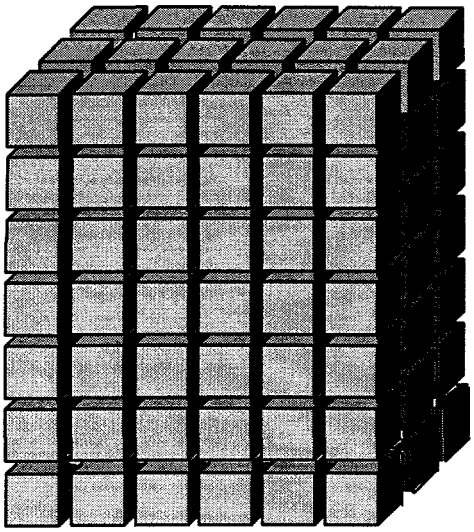

Classical Single-Rate Diffusion

- Constant Matrix Block Size

  (i.e., surface area for diffusion and diffusion distance)

- Constant tortuosity

  (tortuous nature of "matrix" pores)

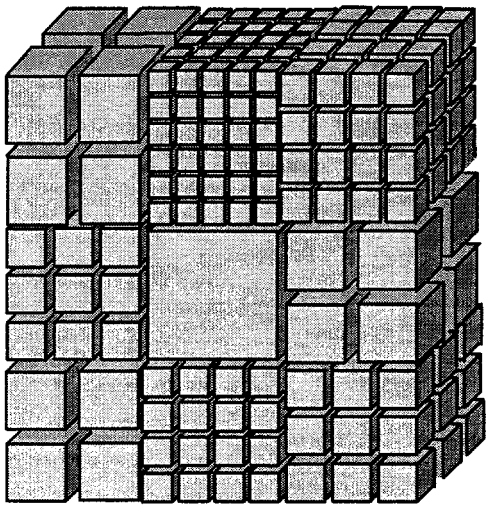

Multirate Diffusion

- Multiple Rates of Diffusion

Distribution of mass transfer rates attributed to variations in matrix block size and tortuosity

TRI-6801-007-0

Figure 3-1. Schematic of double porosity models: a) single-rate–all rates equal and b) multiple-rate.

The retardation coefficient is defined as the relation

$$R = 1 + \frac{\rho_b K_d}{\phi} \tag{3-2}$$

where K_d [L^3/M] is the equilibrium, linear sorption, distribution coefficient. The K_d can be related to a surface equilibrium constant (K_a) through the expression (Neretnieks, 1980)

$$K_d = K_a S_A \tag{3-3}$$

The capacity coefficient, β_n^*, is a ratio of the total amount of solute mass in the diffusive-porosity zone n with the total amount of solute mass in advective porosity, when mass transfer between the advective porosity and the diffusive-porosity type n is in equilibrium [i.e., $C(t) = C_n^*(t)$]. The capacity coefficient is defined as

$$\beta_n^* = \frac{R_n^* \phi_n^*}{R\phi}, \tag{3-4}$$

where R_n^* [dimensionless] is the retardation coefficient in the diffusive-porosity zone n, ϕ_n^* [dimensionless] is the porosity in diffusive-porosity zone n, and ϕ [dimensionless] is the advective porosity. The value of β_n^* reflects the maximum potential contribution of diffusive-porosity zone n to physical retardation of the breakthrough curve. When $\beta_n^* < 1$, the amount of solute mass that can be contained within diffusive-porosity zone n is less than the amount of solute mass that can be contained within the advective porosity. When $\beta_n^* > 1$, diffusive-porosity zone n can contain more mass than the advective porosity. If β_1^* is very small compared to the sum of the remaining β_n^*, the maximum amount of mass contained within diffusive-porosity zone 1 will be a very small fraction of that contained in the other diffusive-porosity zones, and diffusive-porosity zone 1 can be neglected with a mean error

$$Error \le 1 - \left(1 + \sum_{n=2}^{N} \beta_n^* \Big/ 1 + \sum_{n=1}^{N} \beta_n^* \right) \tag{3-5}$$

The capacity coefficient is important because it provides a metric for comparing the maximum potential influence of each diffusive-porosity zone and, therefore, gives a basis for reducing the total number of diffusive zones in a multiple-rate model (Figure 3-1). Because potential diffusive-porosity types at any one location in the Culebra are distributed in zones of widely varying size, the number of diffusive zones, N, present at any one location in the Culebra is very large. By ranking the values of capacity coefficients for Culebra diffusive-porosity zones and eliminating those zones with very small capacity coefficients, the number of zones could be substantially reduced, and the multiple-rate model simplified.

Two different approaches are used to describe the change in concentration within diffusive-porosity zone n. In the first approach, diffusion into and out of each diffusive-porosity zone is explicitly modeled using the diffusion equation

$$\frac{\partial C_n^*}{\partial t} = \nabla \bullet \left(\mathbf{D}_{a,n} \nabla C_n^* \right) \tag{3-6}$$

where $\mathbf{D}_{a,n}$ is the apparent diffusion coefficient [L^2/T] for the porous media contained within diffusive zone n, given by

$$D_{a,n} = D_v \left(F_n R_n \right)^{-1} \tag{3-7}$$

where D_v is the diffusion coefficient in water [L^2/T], F_n is the formation factor [dimensionless] for diffusive-porosity zone n, and R_n [dimensionless] is the retardation coefficient for equilibrium chemical sorption in the diffusive-porosity zone n.

While this approach is theoretically satisfying and precisely preserves the physics of transport, it is very cumbersome because the initial distribution of solute must be known, and the boundary conditions are complicated because of the irregular shapes of diffusive-porosity zones. In practical applications of diffusion models, the shape and dimensionality of the surfaces bounding each diffusive-porosity zone are simplified by assuming that the surface of each diffusive-porosity zone is a regular geometric form (e.g., parallelogram, cube, sphere, cylinder, or parallel plate). With this assumption, Equation 3-6 is solved analytically or numerically with the appropriate boundary conditions for the concentration in diffusive zones.

Often, further simplifications are made by assuming that all of the diffusive-porosity zones have the same geometric form (e.g., all regions are spheres), that the diffusive-porosity zones are of the same size (e.g., all regions are spheres of the same radius), and, finally, that the hydraulic characteristics of all diffusive zones are the same (e.g., all regions are spheres of the same radius with the same apparent diffusion coefficient). When all of these assumptions are made, the resulting model is a single-rate formulation of Equation 3-1, where $N = 1$ (Figure 3-1a).

A mathematically simpler approach for modeling rate-limited mass transfer between advective and diffusive porosity is similar to the treatment of sorption processes and employs the following first-order approximation for the rate of mass transfer into diffusive zones (Coats and Smith, 1964; van Genuchten and Wierenga, 1976; Bear and Verruijt, 1987; Sardin et al., 1991; Haggerty and Gorelick, 1995):

$$\frac{\partial C_n^*}{\partial t} = \alpha_n \left(C - C_n^* \right) \tag{3-8}$$

where α_n [1/T] is the mass-transfer coefficient for diffusion. In this approach, the unknown, often unknowable, physical aspects of the diffusion processes are lumped into a single parameter (α_n). It is assumed that all solute mass contained in the diffusive-porosity zone n is equally

distributed through the zone at all times; thus C_n^* represents the volumetric average concentration in diffusive zone n. This type of model is a "lumped" parameter model, which can be thought of as a "continuously stirred reactor" or a "mixing cell" of uniform composition. It is important to note that $1/\alpha_n$ [T] is a characteristic time (time constant) for diffusion.

Haggerty and Gorelick (1995) showed that special multiple-rate models incorporating the first-order approximation (Equation 3-8) were equivalent to single-rate models of diffusion (Equation 3-6) from layers, cylinders, and spheres. In all of these multiple-rate equivalents to geometric diffusion models, the mass-transfer coefficients α_n can be described by

$$\alpha_n = B_n \frac{D_{a,n}}{l_n^2} \tag{3-9}$$

where B_n is a geometry-dependent term and l_n is the distance from the center to the edge of an diffusive zone n in a diffusion model. For single-rate, first-order approximations to diffusion models, the geometry term B_n is always greater than one. For spherical diffusion, $B_n \approx \pi^2$; for cylindrical diffusion, $B_n \approx 5.78$; and $B_n \approx \pi^2/4$ for layered diffusion.

Although the first-order model does not precisely preserve the physics of diffusive mass transfer, it offers some practical advantages over diffusion models. The mathematics describing diffusion processes are simple (first-order, ordinary differential equation) and analytical or numerical solutions are more readily obtained. The first-order rate approximation is also convenient for examining the behavior of multiple-rate models and connecting the geologic characteristics of the medium to mass transport.

Using the first-order approximation for diffusion processes, we can show how the general form of the governing equation for mass transport (Equation 3-1) can be simplified, if the rate of mass transfer attributable to diffusion is either very large or very small relative to the rate of advection. For the purpose of this discussion, the rate of advection is defined as

$$\frac{v}{L} \tag{3-10}$$

where L is the advective travel length. For a constant pore water velocity (v), the rate of advection is inversely proportional to the advective travel length.

If the mass-transfer coefficient for a particular zone of diffusive porosity (α_n) is very small when compared to the rate of advective mass transfer, then diffusive mass transport occurs very slowly compared to advective mass transport, and

$$\frac{\partial C_n^*}{\partial t} \approx 0 \tag{3-11}$$

If the mass-transfer coefficients for all N of the diffusive-porosity zones are sufficiently small when compared to the rate of advection, essentially no solute mass is transferred into the diffusive porosity, and the governing equation (Equation 3-1) reduces to

$$\frac{\partial C}{\partial t} = \nabla \bullet \left(\frac{\mathbf{D}}{R} \nabla C \right) - \frac{\mathbf{v}}{R} \nabla C \tag{3-12}$$

which is a single-porosity form of the advection dispersion equation in which only the advective porosity participates in mass transport processes. Similarly, if the mass-transfer coefficient α_n is very large relative to the rate of advective mass transfer, then diffusive solute transport occurs very quickly compared to advective transport, and

$$C_n^* \approx C \tag{3-13}$$

If all N of the mass-transfer coefficients are very large, it can be assumed that the mass transfer between the advective porosity and all diffusive-porosity zones is in equilibrium and occurs instantaneously. This assumption is commonly referred to as the local equilibrium assumption (LEA). When the LEA is valid, the simplest form of the governing equation becomes

$$\left(1 + \sum_{n=1}^{N} \beta_n^* \right) \frac{\partial C}{\partial t} = \nabla \bullet \left(\frac{\mathbf{D}}{R} \nabla C \right) - \frac{\mathbf{v}}{R} \nabla C \tag{3-14}$$

Equation 3-14 is also a single-porosity form of the advection dispersion equation with a physical retardation coefficient equal to

$$1 + \sum_{n=1}^{N} \beta_n^* \tag{3-15}$$

It is important to note that slow advective mass transfer can be simulated using a first-order approximation. Mass transfer coefficients for slow advection are proportional to $v/2l$, and all principles here applied to first-order diffusion also apply to first-order approximations of slow advective transport processes.

Because $1/\alpha_n$ [T] is a characteristic time for diffusion and the advective travel length (L) divided by the retarded velocity is the mean advective travel time, a scaled ratio of the advective travel time versus the time for diffusion (a Damkohler Type I number [Damkohler, 1936]) can be used to determine whether diffusion occurs very slowly or very rapidly when compared to advection.

3.2 Damkohler Type I Number as a Metric for Transport Processes

Bahr and Rubin (1987), by direct comparison of the mathematical formulation for transport under LEA conditions and non-equilibrium conditions, developed a procedure for determining a Damkohler number for double-porosity models. The Damkohler Type I number for the diffusive-porosity zone n (Haggerty and Gorelick, 1995) is

$$DaI_n = \alpha_n \left(\beta_n^* + 1\right) \frac{LR}{v} \qquad (3\text{-}16)$$

For a given mass-transfer coefficient, capacity coefficient, and mean advective travel time (all terms to the right of the parentheses in Equation 3-16), the Damkohler number indicates the importance of advection versus diffusion processes. During one-dimensional transport, diffusion essentially occurs instantaneously relative to advection when the Damkohler number approaches 100 (Haggerty and Gorelick, 1995). Although the minimum Damkohler number at which multiple-rate behavior begins to occur has not been explicitly defined, Bahr and Rubin (1987) indicate that for Damkohler numbers less than ~ 10^{-2} that the rate of reaction (e.g., diffusion) is so slow that virtually no reaction (diffusion into diffusive porosity) occurs in a finite time.

It is important to note that the Damkohler number is directly proportional to the advective travel length (L) when all other parameters remain constant. For a short advective length, a small Damkohler number indicates that the time for diffusion is much larger than the time required to advect solutes a distance of L through the medium. If Damkohler numbers for all N diffusive-porosity zones in a multiple-rate model are very small ($<10^{-2}$), then breakthrough curves observed at distance L will reflect single-porosity behavior, and mass transport can be described mathematically by Equation 3-12. If the Damkohler number is between 10^{-2} and 100, the time for diffusion is roughly of the same order as the time required to advect solutes a distance of L. When the Damkohler numbers of one or more diffusive-porosity zones in a multiple rate model are between 10^{-2} and 100, breakthrough curves observed at L will show double-porosity behavior. When the Damkohler number is ≥ 100, diffusion appears to occur instantaneously relative to the time required to advect solutes a distance L through the medium. When the Damkohler numbers for all of the diffusive-porosity zones in a multiple-porosity model are greater than 100, breakthrough curves observed at a distance L from the source will show single-porosity behavior, and observed mass transport at L can be mathematically described by Equation 3-14.

An example of how increasing Damkohler numbers or advective travel length affects breakthrough curves at the advective distance (L) is shown in Figure 3-2. Figure 3-2 shows the simulated breakthrough curves for one-dimensional transport through a double-porosity, single-rate medium. For reference, a single-porosity simulation using Equation 3-12 and a single-porosity (LEA) simulation using Equation 3-14 are included. The inlet boundary condition for all simulations is an infinite duration, unit step increase in concentration. The advective travel length (L) and the Damkohler number increase an order of magnitude for each successive simulation. Simulations with Damkohler numbers of less than 10^{-2} fall on the single-porosity breakthrough curve, indicating that at short advective travel lengths (L) diffusion occurs too slowly when compared with advection to alter the breakthrough curve. For simulations where the Damkohler number was 0.1 or 1.0, the breakthrough curves are substantially different, indicating that diffusion is significant at these time and length scales. The lower part of these breakthrough curves, which primarily reflect advection of the solute, is also physically retarded (shifted to the right of the single-porosity breakthrough curve) due to diffusion. Above the lower advectively-dominated parts of these curves, a marked decrease in slope occurs at the point when diffusion begins to dominate transport. In this dimensionless time region, mass transfer of

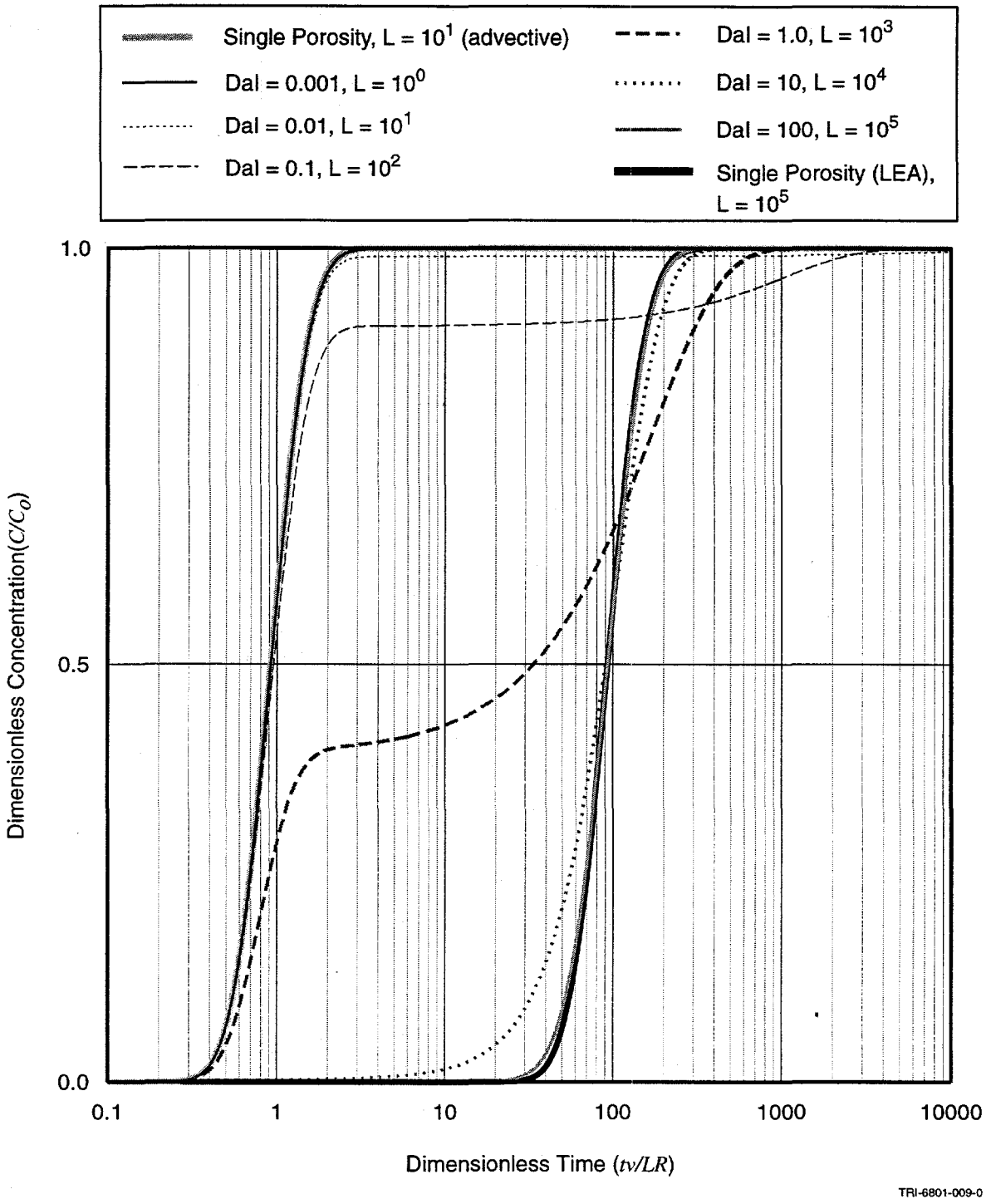

Figure 3-2. Simulated breakthrough curves for one-dimensional transport in a double-porosity, single-rate medium. To provide reference, single porosity breakthrough curves equivalent to Equations 3-12 and 3-14 are shown. The boundary condition at the inlet is an infinite duration, step increase in concentration.

solutes into the diffusive porosity exceeds the rate of advective transport, so the breakthrough curves flatten. Once the concentration in the diffusive porosity approaches that of the advective porosity, all of the diffusive porosity is saturated with solute, and the slope of the breakthrough curves again rises.

The breakthrough curves for the simulations with Damkohler numbers of 10 and 100 show substantial physical retardation from diffusion. The shape of the breakthrough curves resembles a single-porosity breakthrough curve. Because the mass transfer rate for diffusion is much greater than the rate advective mass transfer, solutes must access nearly all of the diffusive porosity before advection can occur. The breakthrough curve from the simulation with a Damkohler number of 100 falls on the single-porosity (LEA) breakthrough curve, indicating that diffusion occurs nearly instantaneously relative to advection and all of the diffusive porosity is fully participating in the transport process.

The breakthrough curves shown in Figure 3-2 illustrate how transport processes in a double-porosity medium can show single-porosity behavior, where only advective porosity participates in transport, during transport over a short distance (L). As the length scale (L) progressively increases, the breakthrough curves begin to show the effects of diffusion, and finally the breakthrough curves "roll-up," showing single-porosity (LEA) behavior, where all of the diffusive porosity "instantaneously" participates in transport. This type of behavior is not limited to first-order diffusion models. Using a one-dimensional numerical implementation of Equations 3-1 and 3-6 with $N = 1$, Reeves et al. (1987) show that models that treat diffusion explicitly also tend to show LEA behavior at large advective travel times.

In a double-porosity medium, the total amount of mass that can be chemically sorbed depends on how much solute moves into the diffusive porosity. As we have previously shown in Figure 3-2, mass transfer into the diffusive porosity can be considered a function of the advective travel length. Figure 3-3 illustrates how the mass contained within the diffusive porosity increases with time. All of the curves shown in Figure 3-3 reflect the dimensionless mass contained within the one-dimensional column of Figure 3-2.

For the case of the single-porosity (advective porosity only) curve (Equation 3-12), solutes are denied access to the diffusive porosity, and the total mass in the system rises until all of the advective porosity (10^{-2}) is filled. At this point, the mass remaining in the column does not change with time, because solutes are not allowed to access the diffusive porosity. The mass remaining for a Damkohler number of 0.001 essentially follows the single-porosity (advective porosity only) curve until a critical time is reached at a dimensionless time of ~40. At this threshold time, significant solute mass begins to diffuse into and accumulate in the diffusive porosity. As the Damkohler number or the problem length scale increases, this threshold time occurs earlier on a dimensionless time scale, indicating that the time for diffusion is decreasing relative to the time for solutes to advective a distance length (L). At a Damkohler number of 100, the mass remaining in the column follows the single-porosity (LEA) curve (Equation 3-14) indicating that diffusive mass transfer occurs instantaneously relative to the time required to advect a distance (L). All of these curves show that the amount of solute contained in diffusive porosity (including sorbed solute) increases with time, and the amount of time required to diffuse significant solute mass into the diffusive porosity, relative to the advective travel time, will decrease as the advective travel length increases.

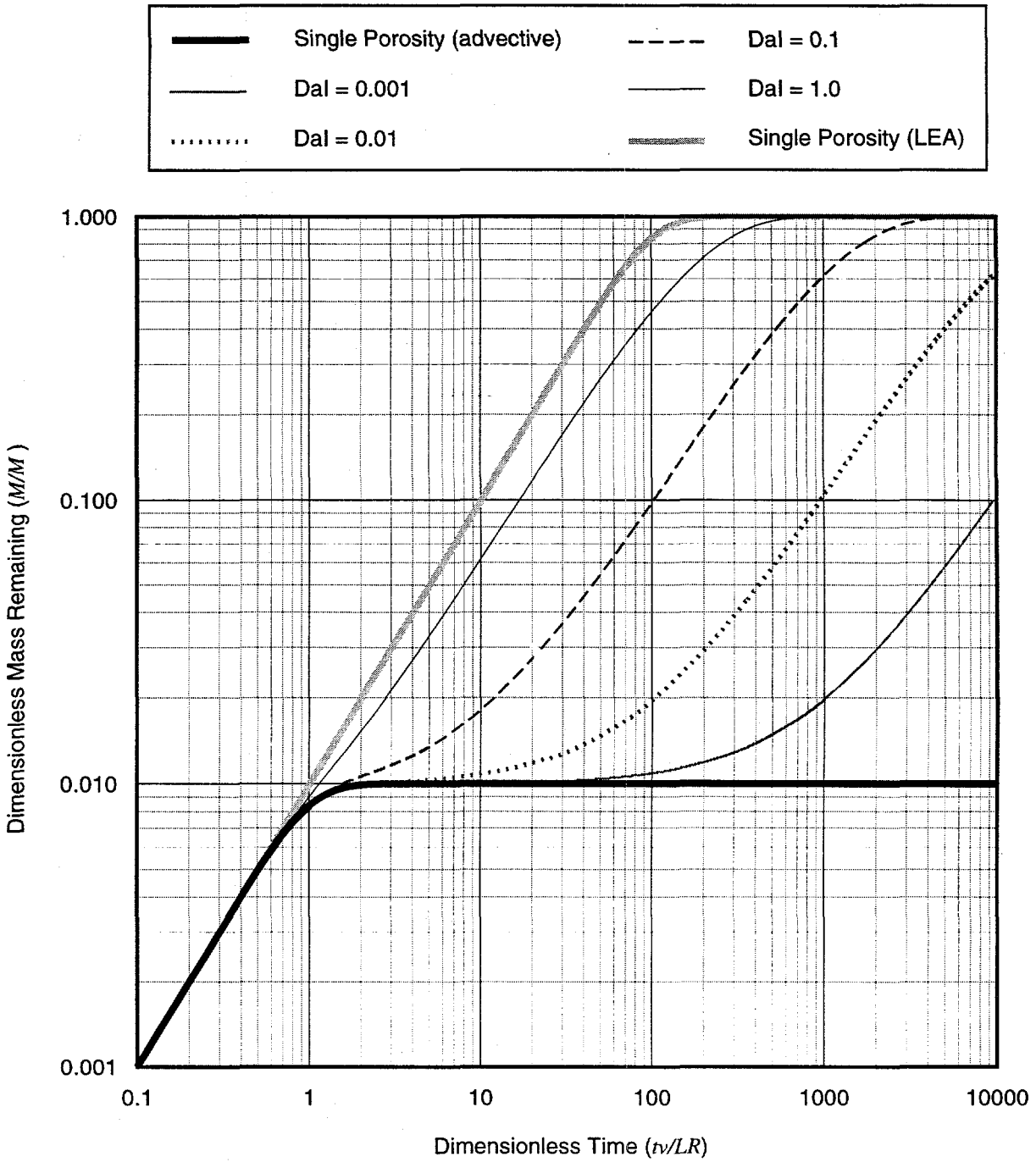

Figure 3-3. Simulations of the dimensionless mass remaining in a one-dimensional column containing a double-porosity, single-rate medium. The boundary condition at the inlet is an infinite duration, step increase in concentration. To provide reference, single-porosity mass remaining curves equivalent to Equations 3-12 and 3-14 are shown.

For a finite-duration pulse at the inlet boundary, the maximum amount of mass contained within the diffusive porosity will increase as the Damkohler number or advective travel length increases. If the pulse passes through the column before the threshold time for diffusion, little mass will diffuse into diffusive porosity. As the Damkohler number increases, the critical time for diffusion becomes smaller relative to the advective travel time, and more mass will diffuse into the diffusive porosity. Tailing behavior in the breakthrough curve occurs as mass slowly diffuses back out of diffusive porosity. At a Damkohler number of 100, diffusion into and out of the diffusive porosity occurs instantaneously relative to the advective travel time, and the breakthrough curve will be physically retarded because all of the porosity participates in mass transport. If this occurs, the LEA is a valid assumption.

3.3 Sub-Models within the Multiple-Rate, Double-Porosity Model

The preceding discussion (Section 3.2) shows how knowledge of the Damkohler numbers for each diffusive porosity type can be used to predict general breakthrough curve behavior. This knowledge can also be used to simplify the multiple-rate model (Haggerty and Gorelick, 1995). At different length and time scales, one of four simplified sub-models may be used to simulate transport processes:

- **Sub-Model 1**. Single-porosity, zero-rate, advection-dispersion model (Equation 3-12) is applied when the Damkohler numbers for all possible diffusive-porosity zones are less than 10^{-2}.

- **Sub-Model 2**. Double-porosity, single-rate advection-dispersion model (Equations 3-1 and 3-6, or 3-8, with N=1) is applied when the Damkohler numbers of all diffusive-porosity zones are approximately equal and between 10^{-2} and 100. This model is also applied when only one diffusive-porosity zone has a Damkohler number between 10^{-2} and 100. In this case, diffusive-porosity zones with Damkohler numbers $< 10^{-2}$ are excluded from the problem, and a physical retardation factor containing the capacity coefficients from all of those porosity zones with Damkohler numbers ≥ 100 is used.

- **Sub-Model 3**. Double-porosity, multiple-rate, advection-dispersion model (Equations 3-1 and 3-6, or 3-8) is applied when the Damkohler number of more than one diffusive-porosity zone is between 10^{-2} and 100. In this case, diffusive-porosity zones with Damkohler numbers $< 10^{-2}$ are excluded from the problem, and a physical retardation factor containing the capacity coefficients from all of those porosity types with Damkohler numbers ≥ 100 is applied. In this case, diffusive-porosity zones with Damkohler numbers $< 10^{-2}$ or ≥ 100 are treated as Sub-Model 2.

- **Sub-Model 4**. Single-porosity, LEA, advection-dispersion model (Equation 3-14) is applied when the Damkohler numbers of all diffusive-porosity zones are ≥ 100.

For a given geologic medium and groundwater velocity, it is possible that each of the preceding models could be relevant at different problem scales (Figure 3-4). As the advective travel length increases, the time for advection increases proportionally, but the mass-transfer

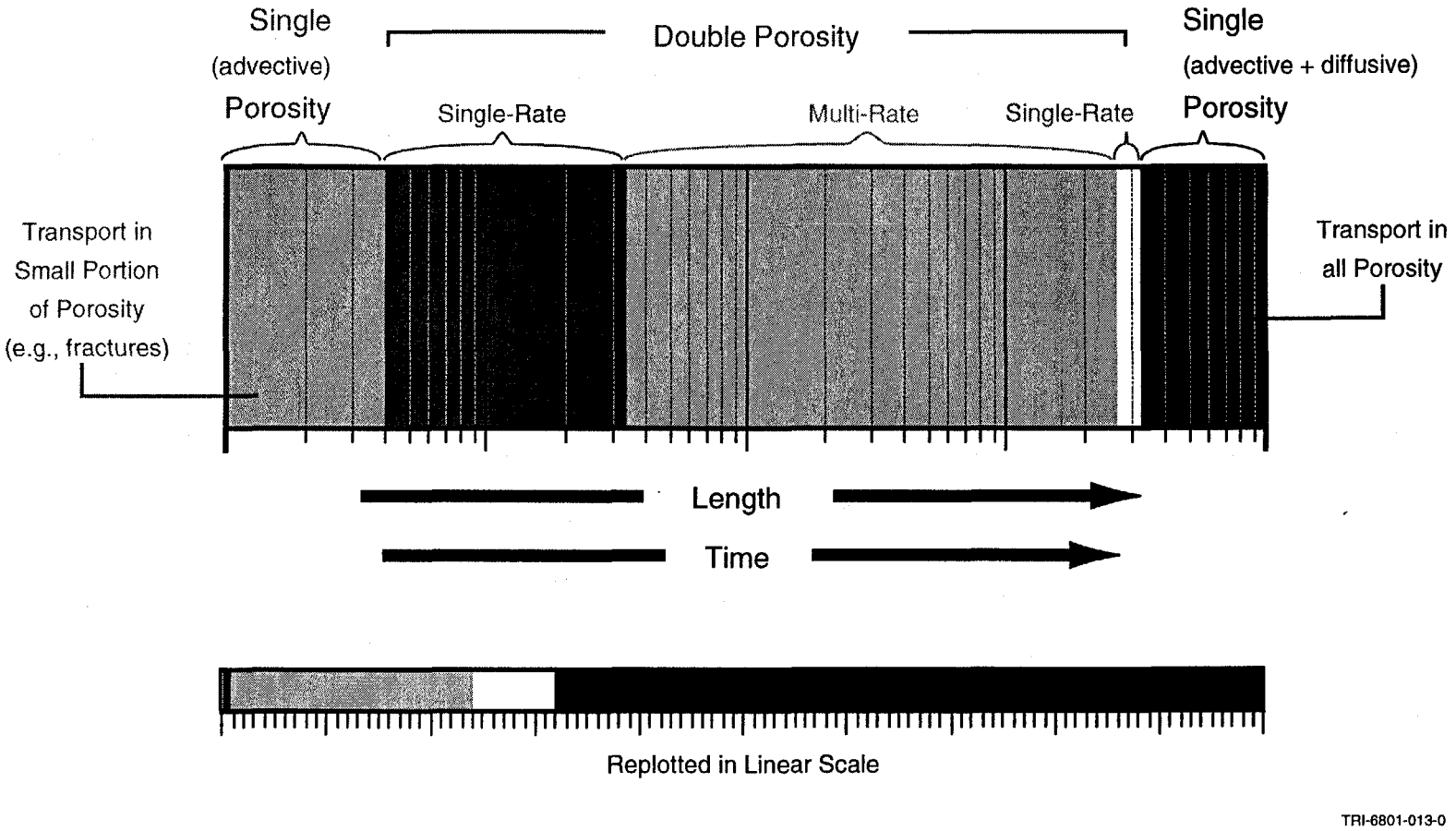

Figure 3-4. Expected Culebra transport behavior as a function of distance and time.

coefficients for diffusion and the capacity coefficients remain the same. Consequently, the Damkohler number for a particular porosity type will increases as the advective travel length increases. For example, the breakthrough curve from a core-scale sample of porous medium may be approximately modeled using Sub-Model 1, because all Damkohler numbers may be $< 10^{-2}$. As the advective travel length increases, the Damkohler number of the diffusive-porosity zone with the largest mass-transfer coefficient will rise above 10^{-2}, while the Damkohler numbers of the remaining diffusive-porosity zones will remain below 10^{-2}. Under these circumstances, Sub-Model 2 is the simplest mathematical model for transport. A field-scale tracer test may best be modeled using Sub-Model 3, if the Damkohler number of several diffusive-porosity zones is between 10^{-2} and 100. At an even larger scale, all but one of the diffusive-porosity zones may be in equilibrium with the advective porosity, and Sub-Model 2 is again the simplest mathematical model for transport. At a regional scale, all diffusive-porosity zones may be in equilibrium with the advective porosity, and Sub-Model 4 will adequately describe transport processes.

3.4 Estimates of Critical Culebra Length Scales

As previously indicated (Sections 3-2 and 3-3), the multiple-rate, double-porosity model can be simplified to a single-porosity model (Equation 3-12) or a single-porosity LEA model (Equation 3-14) when the Damkohler numbers for all possible diffusive-porosity zones is either very small (10^{-2}) or very large (100), respectively. For conditions defined by a constant pore-water velocity and a homogeneous distribution of diffusive-porosity zones, the Damkohler number is a function of advective travel length only. By identifying the critical lengths at which the Damkohler numbers equal 10^{-2} or 100 for each diffusive-porosity zone, the length scales over which each of the four sub-models (Section 3.3) apply can be estimated.

Before the critical length scales can be estimated, relevant parameters must be known, including the advective porosity, the advective retardation coefficient, the number of diffusive-porosity zones, their mass-transfer coefficients, and their capacity ratios. In most circumstances, it is not possible to know all of the required parameters to undertake this exercise. These parameters can be estimated, however, using information from samples and geologic descriptions. Because this type of first-order approximation provides estimates of expected transport behavior independent of transport experiments or numerical simulation, it is potentially useful for both experimental design and conceptual model validation.

For the following analyses, the Culebra is considered a multiple-rate, double-porosity medium and is assumed to be homogeneous with characteristics described by the idealized hydrogeologic framework for the H-19 hydropad (Section 2-4). Diffusion is assumed to follow a first-order model (Equation 3-8), and critical lengths are estimated for both non-reactive and reactive transport using

$$L_{i,n} = \frac{v}{R_{p,n} R \alpha_n \left(\beta^*_n + 1\right)} DaI_i \qquad (3\text{-}17)$$

where DaI_i equals 10^{-2} or 100 for $i = 1, 2$, $R_{p,n}$ is the physical retardation coefficient for the advective porosity, and R is the chemical retardation coefficient for the advective porosity. The mass transfer coefficient is described by Equation 3-9 with a free-water diffusion coefficient

arbitrarily assumed to be 3×10^{-10} m^2/s. For all calculations, an arbitrary average pore-water velocity of 1 m/yr (~3×10^{-8} m/s) is assumed. Advective porosity and advective specific surface area for each Culebra unit are given in Table 2-1. Half-block size, idealized geometry, specific surface area, and porosity for diffusive-porosity zones are also defined in Table 2-2.

Capacity coefficients that apply over short time and length scales are calculated using Equation 3-4. Capacity coefficients used in the calculations for critical lengths, however, must reflect physical retardation as diffusive porosity zones reach LEA conditions. Under these circumstances, the capacity coefficients are determined by scaling the result from Equation 3-4 with a physical retardation factor

$$\beta^*_{L,n} = \frac{\beta^*_n}{R_{p,n}} \tag{3-18}$$

As the LEA is reached for preceding porosity types, the physical retardation coefficient for the advective porosity that is applied in Equation 3-18 is determined from

$$R_{p,n} = R_{p,n-1}\left(1+\sum_{n=1}^{I}\beta^*_{LEA,n}\right) \tag{3-19}$$

where I is the number of diffusive porosity zones, with capacity coefficients of $\beta^*_{LEA,n}$, that have $DaI > 100$ and $R_{p,0} = 1$. For reactive transport, chemical retardation is assumed to occur in both the advective and diffusive porosity, and chemical retardation coefficients are calculated using

$$R = 1+\frac{\rho_b K_a S_A}{\phi} \tag{3-20}$$

with an arbitrary K_a equal to 6.5×10^{-5} m (equal to a K_d of ~100 cm^3/gm when the specific surface area equals 1.5 m^2/gm).

Table 3-1 contains estimates of capacity coefficients for both reactive and non-reactive transport at short time and length scales for $DaI = 0.01$ in all Culebra units at the H-19 hydropad. Careful examination of Table 3-1 yields some insight into short-scale transport processes within the Culebra units. For each Culebra unit, non-reactive capacity coefficients vary by up to an order of magnitude, reflecting porosity variations between diffusive-porosity zones. For reactive-transport, however, the capacity coefficients are all approximately the same, suggesting that the ratio of the diffusive versus advective specific surface area controls the capacity coefficient. This can be illustrated by comparing the short-scale capacity coefficient for non-reactive transport

$$\beta^*_n = \frac{\phi^*_n}{\phi} \tag{3-21}$$

Table 3-1. Estimated Capacity Coefficients Valid for Short Time and Length Scales (β^*) (Equation 3-4) and Large Time and Length Scales (β_L^*) (Equation 3-18 with 3-19)

Culebra Unit	Porosity Type	Half-Block Size/ Geometry	Non-reactive β^*	Non-reactive β_L^*	Reactive β^*	Reactive β_L^*
CU-1	Intercrystalline	2 cm/ spherical	0.1	0.1	5	5
		5 cm/layered	0.8	0.8	5	0.8
	Intercrystalline with vugs	15 cm/ layered	0.9	0.5	5	0.5
	Intercrystalline	15 cm/ layered	0.6	0.3	5	0.3
CU-2/ CU-3	Intercrystalline	1 cm/ spherical	0.3	0.3	4	4
	Intercrystalline with vugs	1 cm/ spherical	0.2	0.2	4	4
	Intercrystalline	5 cm/ spherical	0.4	0.2	3	0.4
	Intercrystalline with vugs	5 cm/ spherical	0.3	0.2	4	0.4
		10 cm/ layered	0.3	0.2	3	0.2
CU-4	Intercrystalline	2 cm/ spherical	0.5	0.5	16	16
		5 cm/layered	2	2	16	0.9
	Intercrystalline with vugs	5 cm/layered	2	1	16	0.9
		15 cm/ layered	4	0.7	15	0.3

with the short-scale capacity coefficient for reactive transport

$$\beta_n^* = \frac{\phi_n^* + K_a S_{A,n} \rho_{b,n}}{\phi + K_a S_A \rho_b} \tag{3-22}$$

where S_A is the specific surface area of the advective porosity; $S_{A,n}$ is the specific surface area of the diffusive-porosity zone n; ρ_b is the advective bulk density (Equation 2-2), a function of the

advective porosity; and $\rho_{b,n}$ is the diffusive bulk density (Equation 2-2), a function of the porosity in diffusive zone n. When the product of the bulk density and K_a is approximately one or greater, the capacity coefficient for reactive transport can be approximated by

$$\beta_n^* \approx \frac{S_{A,n}}{S_A} \tag{3-23}$$

Since the specific surface area of Culebra porosity types is essentially the same, the values of reactive capacity coefficients for all Culebra diffusive porosity zones will be essentially the same at short time and length scales.

At larger time and length scales, at least one diffusive porosity zone has reached *DaI* = 100 (LEA conditions). When this occurs, physical retardation slows the movement of an advecting plume, allowing more time for solutes to diffuse into diffusive-porosity zones. As more diffusive-porosity zones reach LEA conditions, the effect of physical retardation will increase. Because physical retardation processes are incorporated into capacity coefficients for each diffusive-porosity zone (Equations 3-18 and 3-19), the capacity coefficients at larger time and length scales will tend to decrease as more diffusive porosity zones reach LEA conditions.

Table 3-1 contains estimates of capacity coefficients used for calculating the maximum critical lengths for Culebra units at the H-19 hydropad. These capacity coefficients are valid at larger time and length scales and are determined using Equations 3-18 and 3-19. Therefore, these capacity coefficients are valid only at length scales greater than the maximum length scale of preceding diffusive porosity zones that have reached LEA conditions.

The median value of mass-transfer coefficients for CU-1 and CU-4 is approximately the same (Table 3-2), while the median value for mass-transfer coefficients in CU-2/CU-3 is about one order of magnitude larger. These differences confirm that the Culebra should be considered vertically heterogeneous with respect to diffusion properties and indicate that processes governing reactive and non-reactive transport in the Culebra are different.

Table 3-3 contains the reactive and non-reactive critical lengths corresponding to the assumed pore-water velocity for each zone of diffusive porosity within Culebra units. Most of the critical lengths at which the $DaI = 10^{-2}$ are very small, suggesting that, at the assumed velocity, multiple-rate, double-porosity transport behavior will begin by an advective travel distance of roughly 0.1 m. CU-1 has the largest critical lengths for *DaI* = 100; the average values are about one order of magnitude greater than those for the other Culebra units. It is important to note that the resulting critical lengths vary linearly with velocity and can be scaled by multiplying the calculated critical lengths by a new average pore-water velocity with units of m/yr.

Using the criteria outlined in Section 3.3 for Sub-Models 2 and 4, the critical lengths at which *DaI* = 100 can be used to delineate the approximate scales at which the Culebra could be modeled using a single-rate, double-porosity model and a single-porosity LEA model. Single-rate, double-porosity behavior can be expected in CU-2/CU-3 at an advective travel length of ~200 m for non-reactive transport and ~300 m for reactive transport. At advective travel lengths of ~300 m for reactive and non-reactive transport, single-rate, double-porosity behavior can be

Table 3-2. Mass Transfer Coefficients (Equation 3-9) for Diffusive Porosity Zones in Culebra Units at the H-19 Hydropad

Culebra Unit	Porosity Type	Half-Block Size (m) Geometry	Non-Reactive Mass Transfer Coefficient (1/s)	Reactive Mass Transfer Coefficient (1/s)
CU-1	Intercrystalline	0.02 (m)/spherical	7×10^{-8}	2×10^{-12}
		0.05 (m)/layered	3×10^{-9}	5×10^{-13}
	Intercrystalline with vugs	0.15 (m)/layered	3×10^{-10}	7×10^{-14}
	Intercrystalline	0.15 (m)/layered	3×10^{-10}	4×10^{-14}
CU-2/ CU-3	Intercrystalline	0.01 (m)/spherical	3×10^{-7}	3×10^{-11}
	Intercrystalline with vugs	0.01 (m)/spherical	3×10^{-7}	2×10^{-11}
	Intercrystalline	0.05 (m)/spherical	1×10^{-8}	1×10^{-12}
	Intercrystalline with vugs	0.05 (m)/spherical	1×10^{-8}	1×10^{-12}
		0.1 (m)/layered	7×10^{-10}	9×10^{-14}
CU-4	Intercrystalline	0.02 (m)/spherical	7×10^{-8}	2×10^{-12}
		0.5 (m)/layered	3×10^{-9}	5×10^{-13}
	Intercrystalline with vugs	0.5 (m)/layered	3×10^{-9}	4×10^{-13}
		0.15 (m)/layered	3×10^{-10}	1×10^{-13}

expected in CU-4. In CU-1, however, single-rate, double-porosity transport behavior will not occur before ~3 km for reactive transport. This suggests that transport over advective transport distances of greater than ~300 m in CU-2/CU-3 and CU-4 could be modeled using a single-rate, double-porosity model, if the pore-water velocity is ~1m/yr. Because these critical lengths vary linearly with velocity, the critical lengths for another pore water velocity could be estimated by scaling these results (Table 3-3) with the other velocity (m/yr). For reactive transport, the LEA will not apply at scales less than 0.6 km for CU-4, 2 km for CU-2/CU-3, and 4 km for CU-1.

When the critical lengths for different diffusive-porosity zones are approximately the same, this indicates that the Damkohler numbers for the zones are also approximately the same. The critical lengths for similar size diffusive-porosity zones containing intercrystalline porosity and intercrystalline porosity with vugs in both CU-2/CU-3 and CU-4 are similar, indicating that the Damkohler numbers for these porosity types are very close at all scales. Because the Damkohler numbers are similar in these units, these porosity types can be lumped together for

Table 3-3. Critical Lengths (Equation 3-17) for Nonadvective Porosity Zones within Culebra Units at the H-19 Hydropad Assuming a Pore Water Velocity of 1 m/yr

Culebra Unit	Porosity Type	Half-Block Size/ Geometry	Non-reactive L (m) $DaI = 10^{-2}$	Non-reactive L (m) $DaI = 100$	Reactive L (m) $DaI = 10^{-2}$	Reactive L (m) $DaI = 100$
CU-1	Intercrystalline	2 cm/ spherical	0.004	40	0.04	400
		5 cm/ layered	0.06	600	0.1	600
	Intercrystalline with vugs	15 cm/ layered	0.5	4,000	1	3,000
	Intercrystalline	15 cm/ layered	0.7	4,000	2	4,000
CU-2/ CU-3	Intercrystalline	1 cm/ spherical	0.0009	9	0.003	30
	Intercrystalline with vugs	1 cm/ spherical	0.0009	9	0.005	50
	Intercrystalline	5 cm/ spherical	0.02	200	0.07	300
	Intercrystalline with vugs	5 cm/ spherical	0.02	200	0.08	300
		10 cm/ layered	0.3	2,000	1	2,000
CU-4	Intercrystalline	2 cm/ spherical	0.003	30	0.01	100
		5 cm/ layered	0.04	300	0.05	200
	Intercrystalline with vugs	5 cm/ layered	0.04	300	0.06	300
		15 cm/ layered	0.2	1,000	0.2	600

Values rounded to one significant figure.

some applications, simplifying the multiple-rate, double-porosity model for transport. This is not the case, however, for CU-1.

The non-reactive and reactive critical lengths within Culebra units vary over a wide range. For example, the non-reactive critical lengths for $DaI = 100$ are relatively small (~9 m) for the smallest diffusive-porosity zones (half-block size of 0.01 m) within CU-2/CU-3. For the intermediate-size diffusive-porosity zones (half-block size of 0.05 m), the critical lengths are

much larger (~200 m to ~ 300 m). The non-reactive critical length for the largest diffusive porosity zone is ~2000 m. This suggests that each Culebra unit will display a multimodal distribution of volume-averaged diffusion rates.

It is important to emphasize that the quantitative results presented in this section represent only first-order approximations that are based on an assumed pore-water velocity and also assume that the distribution of advective and diffusive porosity within the Culebra is everywhere the same as at the H-19 hydropad. These results also reflect chemical sorption in the advective porosity, which will reduce the values of estimated critical lengths by retarding the advective transport. These calculations assume a chemically homogeneous Culebra. If sorption from clay minerals and iron oxides present in many Culebra fractures (advective porosity) were included, these critical lengths would be reduced substantially.

Because the proportions of each porosity type observed in Culebra units is likely to remain about the same across the WIPP area, the results from the H-19 hydropad can be conceptually extended to other locations characterized by transmissivity values higher or lower than those reported for the H-19 hydropad. The results of this extension are general and qualitative and apply only at large time and length scales, where slow advective porosity has reached LEA conditions.

Where the Culebra has a significantly higher transmissivity than at the H-19 hydropad, it is unlikely that half-block sizes of diffusive-porosity zones containing intercrystalline porosity and intercrystalline porosity with vugs will be larger than that observed at the H-19 hydropad, and mass transfer coefficients for these diffusive-porosity zones will be the same or smaller. Advection in more areally extensive fracture networks, however, may bypass a significant portion of the interparticle porosity. If this occurs, the silty dolomite will reach the LEA condition in all Culebra units very quickly, possibly on a hundred-meter scale. For transport at scales of approximately a hundred meters, a physical retardation factor due to the silty dolomite would be applied, and the results from Table 3-3 would be approximately valid for the other types of diffusive porosity. Under steady-flow conditions, the average pore-water velocities will be larger, and the critical lengths where $DaI = 100$ will increase linearly with the velocity.

Where the Culebra transmissivity is significantly lower than at the H-19 hydropad and fewer areally extensive open fractures are present, advection appears to be primarily through zones containing interparticle porosity. Half-block sizes for diffusive porosity zones will increase, resulting in smaller mass transfer coefficients and larger critical lengths. The impact of larger blocks is assessed by recalculating the critical lengths at which $DaI = 100$ with all block sizes doubled except for the largest block sizes which represent the bedding-plane scale (Table 3-4). Under these conditions, the critical lengths at which single-rate, double-porosity behavior can be expected remain the same for CU-1, are increased by a factor of roughly four for CU-2/CU-3. The critical lengths a which single-rate, double porosity behavior will occur in CU-4 is actually decreased to about 100 m, because the critical lengths for the other porosity types are all about 1,000 m. Lower velocities, however, will tend to counteract increases in critical lengths due to smaller mass transfer coefficients.

Despite the nature of the approximation, some results can be generalized. The Culebra can be expected to show vertically heterogeneous diffusion behavior. At field scales, transport in the Culebra will show multiple rates of diffusion because of the different size diffusive-porosity zones. The length scales at which transport through CU-2/CU-3 and CU-4 can be modeled as single-rate, double-porosity medium are approximately the same. Differences between

Table 3-4. Critical Lengths (Equation 3-17) at which *DaI* = 100 for Culebra Units at the H-19 Hydropad with All Block Sizes Doubled, Except the Largest Blocks which Represent the Bedding-Plane Scale

Culebra Unit	**Porosity Type**	**Half-Block Size/ Geometry**	**Non-Reactive *L* (m) *DaI* = 100**	**Reactive *L* (m) *DaI* = 100**
CU-1	Intercrystalline	4 cm/ spherical	200	2,000
		10 cm/ layered	2,000	3,000
	Intercrystalline with vugs	15 cm/ layered	3,000	3,000
	Intercrystalline	15 cm/ layered	4,000	4,000
CU-2/ CU-3	Intercrystalline	2 cm/ spherical	40	100
	Intercrystalline with vugs	2 cm/ spherical	40	200
	Intercrystalline	10 cm/ spherical	700	1,000
	Intercrystalline with vugs	10 cm/ spherical	600	1,000
		10 cm/ layered	2,000	2,000
CU-4	Intercrystalline	0.04 cm/ spherical	100	400
		10 cm/ layered	1,000	1,000
	Intercrystalline with vugs	10 cm/ layered	1,000	1,000
		15 cm/ layered	1,000	1,000

Values rounded to one significant figure.

intercrystalline porosity and intercrystalline porosity containing vugs may be negligible for these units. The strong multimodality in the distribution of fracture-bounded blocks within Culebra units will affect tracer test results. It is likely that at the relatively small scales, e.g., scale of a convergent flow tracer test, the Damkohler numbers of smaller diffusive zones may approach 100, while the larger blocks will still have relatively low Damkohler number. At the WIPP-site scale, it is likely that transport processes in CU-2/CU-3 and CU-4 can be modeled adequately with a physically-retarded, single-rate, double-porosity model.

4. REVIEW OF CULEBRA TRACER EXPERIMENTS

Although it is never possible to validate a conceptual model completely, it can be checked for consistency with existing experimental results. Transport experiments in the Culebra have been conducted at two different length scales. Both reactive and non-reactive tracer tests have been conducted on intact core samples from the Culebra. The length scales of these tests were ~10 cm to ~50 cm. In addition, several types of non-reactive field tracer tests have been conducted in the Culebra with advective transport lengths as large as the well spacing (tens-of-meter scale).

4.1 Core-Column Experiments

Reactive transport experiments, with dissolved actinides in WIPP-relevant brines, have been performed on intact horizontal cores of the Culebra from the WIPP AIS (Lucero, 1996). For these experiments, five intact, 14.5 cm-diameter cylindrical columns were obtained from horizontal cores from CU-2. The columns used for the retardation experiments range in length from 10.2 to 50.9 cm. After cutting to length, each core was encapsulated in a urethane rubber sleeve and then mounted in an aluminum core holder equipped with brass end fittings. During flow experiments, the intact cores were subjected to hydrostatic pressure of the same magnitude as the natural lithostatic pressure of rock in CU-2.

Figure 4-1 depicts the apparatus used for the retardation experiments (Lucero, 1996). In these experiments, brine was pumped from an accumulator (a simple cylinder and piston sealed at both ends) into the core. The dual high-pressure syringe pumps drive water into one end of the accumulator, forcing brine out the other end. Flow rates included 0.05, 0.1, and 0.5 mL/min, with most experiments performed at 0.1 mL/min. Effluent was collected with a fraction collector set to collect ~5 ml per sample. Samples were collected and analyzed using either a germanium solid-state detector or liquid scintillation counting (LSC). Analysis permitted measurement of activity in the effluent as a function of total volume collected (or of time, given the constant flow rate).

Either tritium (as tritiated water) or ^{22}Na was used as a conservative (non-sorbing) tracer in these experiments (Lucero, 1996). ^{22}Na was used for most experiments because its positron emission produces 511-keV γ rays that are readily quantified with either the germanium detector or by LSC. Actinide tracers selected were ^{241}Am, ^{239}Np, ^{241}Pu, ^{228}Th, and ^{232}U. To date, only U and Np have been observed to elute from the columns, even though experiments for Am, Pu, and Th have been carried out for very long periods, indicating that rather high minimum retardation values can be estimated for these species. A typical tracer breakthrough curve is shown in Figure 4-2.

Core samples used for these experiments are very heterogeneous. Core surface maps (Figures 4-3, 4-4, and 4-5) indicate that open fractures and zones of silty dolomite are heterogeneously distributed throughout these cores. Silty dolomite zones are typically irregular and discontinuous. The scale of silty dolomite zones and fractures is much smaller than the scale of the cores, indicating that heterogeneities are present within the core that are not visible on the core exterior. Based on the core surface maps, advective porosity appears to consist of interparticle porosity in the silty dolomite and microfractures. Diffusive porosity consists of intercrystalline porosity within indurated dolomite, intercrystalline porosity with vugs, dead-end

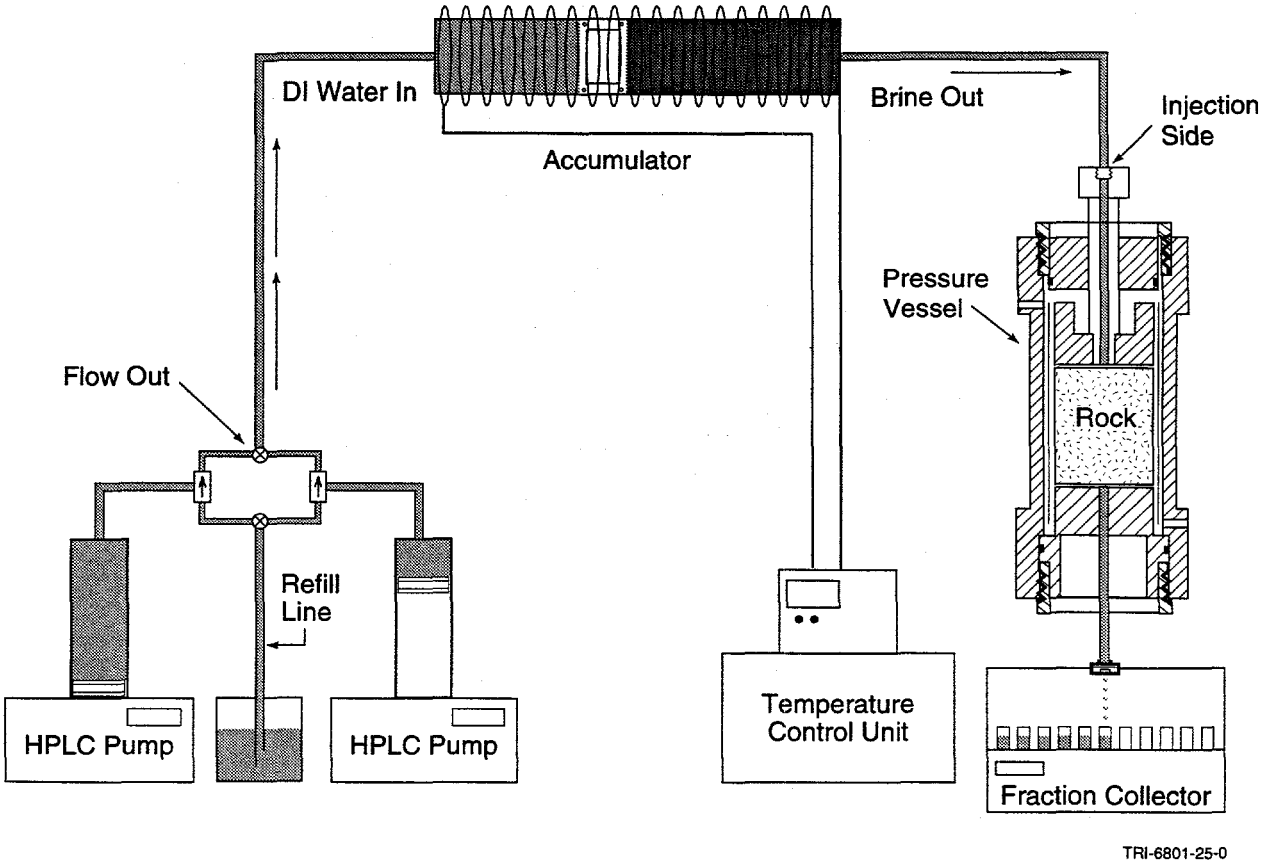

Figure 4-1. Schematic diagram of apparatus used for retardation experiments.

microfractures that are connected to vugs, and intragranular porosity. Several of the cores display unique features. Core D contains clay along some subhorizontal fractures, and Core E has continuous, irregular, subhorizontal zones of silty dolomite.

For each core, the percentage of core surface area associated with each porosity type can be estimated from core surface maps (Table 4-1). Assuming that these percentages are valid throughout the core, the volumetric porosity associated with each porosity type can be estimated (Table 4-1) using the average laboratory porosity values for each porosity type. The estimated total porosity for each core compares well with the total porosity determined from bulk density analyses (Table 4-2). Estimated Damkohler numbers for each porosity type are shown in Table 4-3 and Appendix E. All of the Damkohler numbers are small. In all cores, Damkohler numbers are above 10^{-2}. However, the estimated time for diffusion ($1/\alpha$) is over three orders of magnitude larger than the peak arrival time, so the fluid was not in the column long enough for significant diffusion to occur. Thus transport through these cores could be modeled using a single-porosity model, where only the advective porosity participates in mass transport. In addition, chemical retardation observed in these cores should reflect sorption processes in the advective porosity.

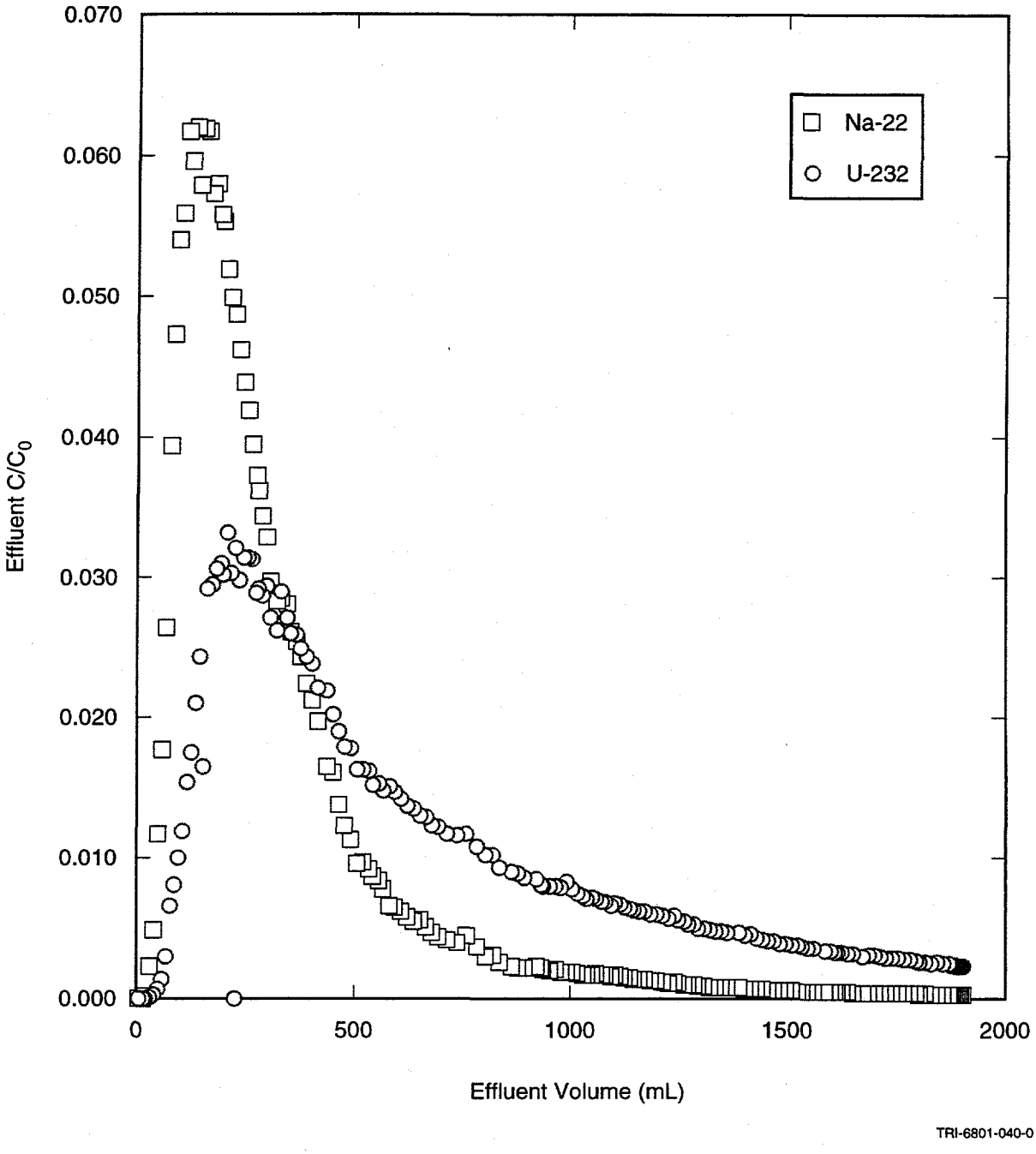

Figure 4-2. Results of a typical elution experiment using ^{22}Na and ^{232}U as conservative and sorbing tracers, respectively.

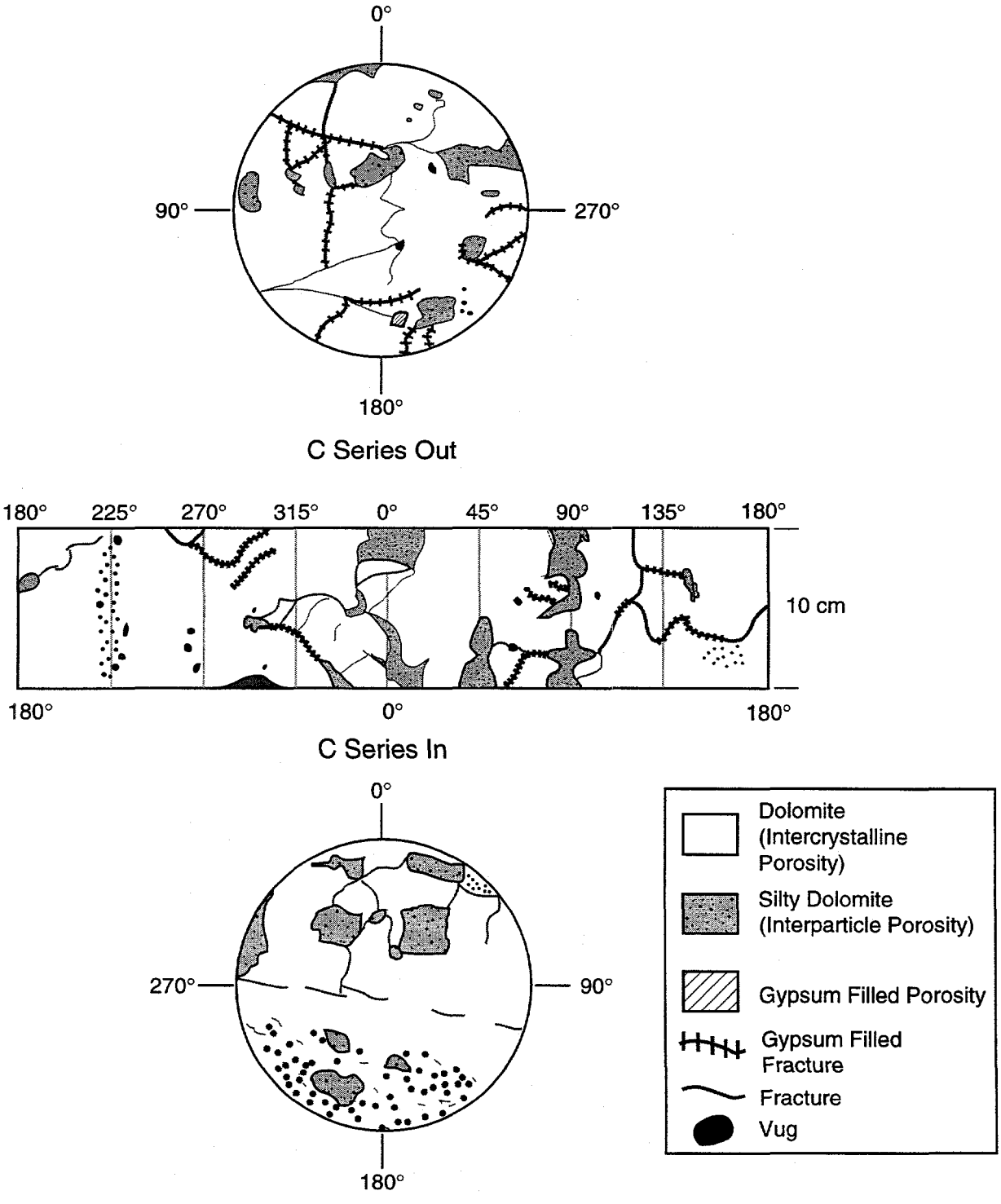

Figure 4-3. Core C surface map.

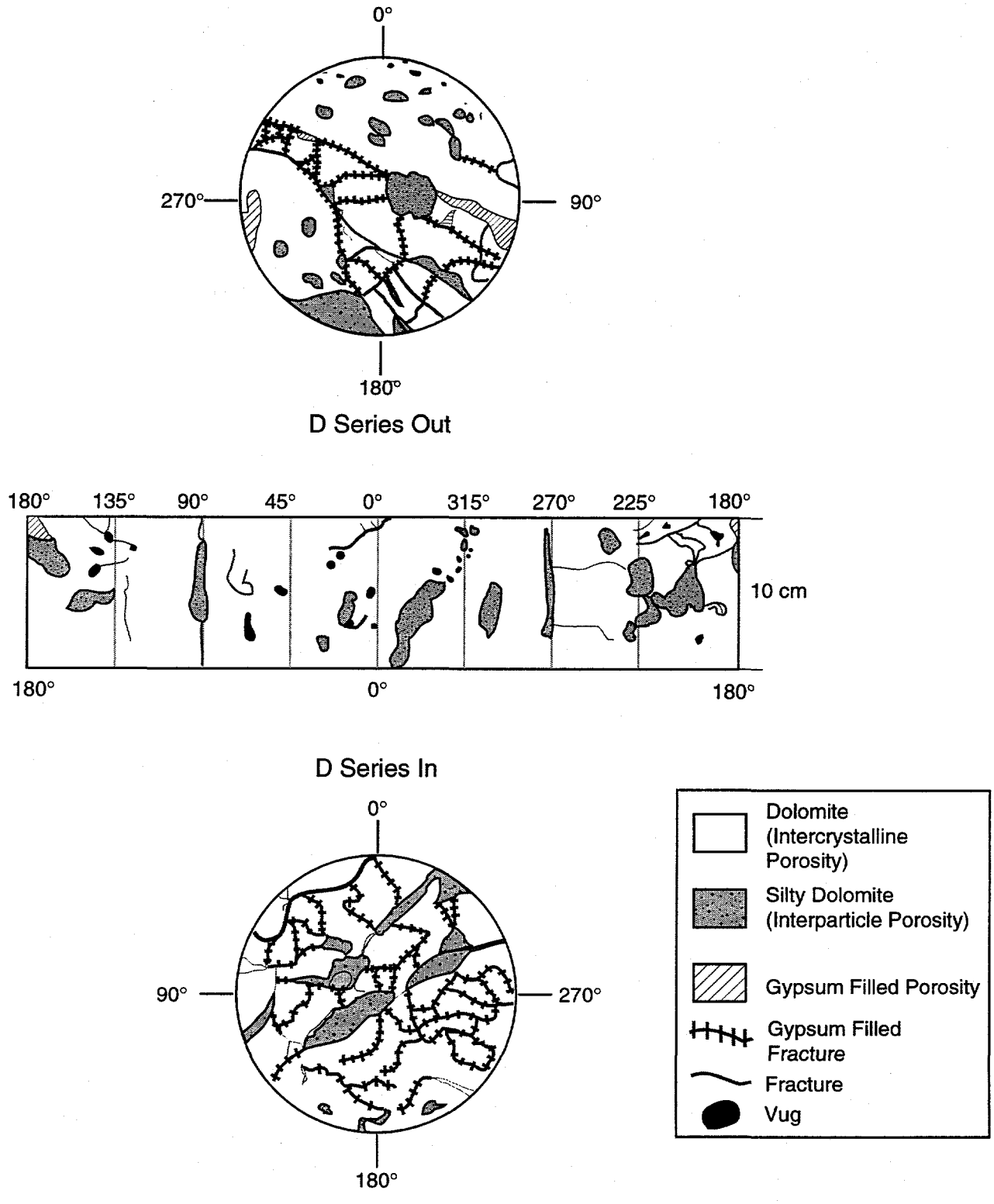

Figure 4-4. Core D surface map.

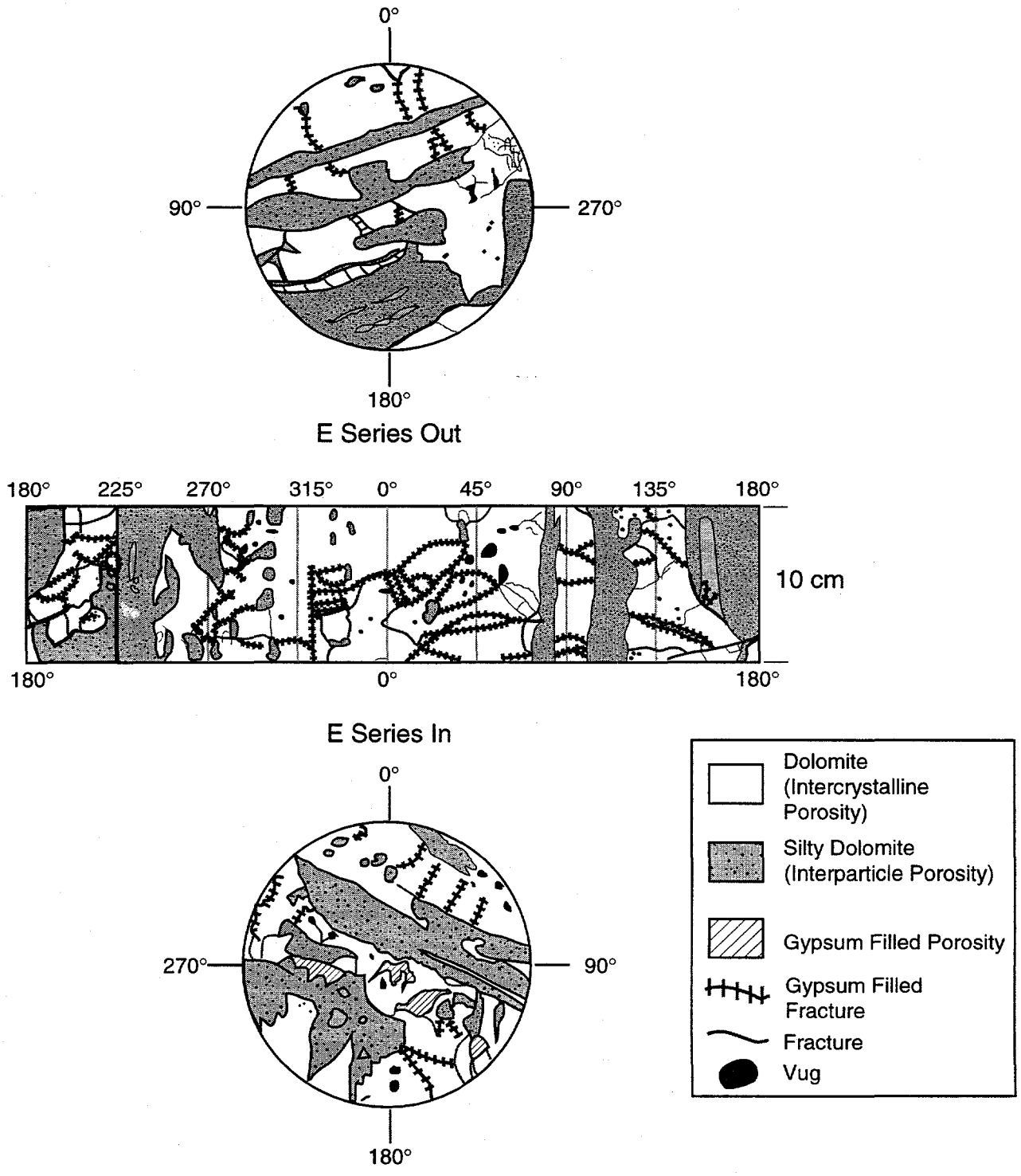

Figure 4-5. Core E surface map.

Table 4-1. Porosity Estimates for Cores C, D, and E

Core	Porosity Type	Percentage of Core Surface Area Containing Porosity Type	Porosity Estimate from Core Maps	Porosity Estimate from Breakthrough Curve Peaks
C	Intercrystalline	93%	0.10	-
	Intercrystalline with vugs	1%	0.001	-
	Interparticle (advective porosity)	6%	0.01	0.02
D	Intercrystalline	84%	0.09	-
	Intercrystalline with vugs	1%	0.002	-
	Interparticle (advective porosity)	15%	0.03	0.04
E	Intercrystalline	58%	0.06	-
	Intercrystalline with vugs	7%	0.01	-
	Interparticle (advective porosity)	35%	0.08	0.08

Table 4-2. Total Porosity Estimates for Cores C, D, and E

Core	Total Porosity Estimated from Core Maps	Total Porosity Estimated from Bulk Density*
C	0.12	0.14
D	0.13	0.14
E	0.15	0.15

*From Lucero (1996).

Table 4-3. Estimated Damkohler Numbers for Diffusive Porosity Zones within Cores C, D, and E (Appendix E)

Core	Porosity Type	Non Reactive *DaI*
C	Intercrystalline	0.1
	Intercrystalline with vugs	0.003
D	Intercrystalline	0.06
	Intercrystalline with vugs	0.02
E	Intercrystalline	0.03
	Intercrystalline with vugs	0.02

Detailed analyses of the core-column experiments have not yet been performed. However, some simple observations yield insight regarding transport processes within these cores. Because estimates for the advective porosity from the peak arrival time for the non-reactive tracers vary little from the estimates based upon the core surface maps (Table 4-1), it is likely that only the advective porosity is participating in mass transport processes, and apparent retardation coefficients for actinide tracers primarily reflect chemical sorption in the advective porosity.

4.2 Field Tracer Tests

A series of tracer tests has been conducted in the vicinity of the WIPP site, to define the processes that might govern radionuclide transport in the Culebra and to evaluate the transport properties of the Culebra dolomite. These tests were conducted, in part, to evaluate whether the Culebra should be modeled as a single-porosity medium with transport only in the fractures or whether modeling should incorporate the participation of other types of porosity in advective or diffusive mass transport. Convergent-flow tracer tests were conducted within the Culebra at three locations (H-3, H-6, and H-11 hydropads) between 1981 and 1988. These tests showed that solute transport was strongly dependent on flow direction and suggested that a physical retardation mechanism was affecting transport. The tracer-breakthrough curves from these tests were simulated using a homogeneous double-porosity, single-rate continuum model. These simulations showed that the observed transport behavior could be explained by a combination of anisotropy in horizontal hydraulic conductivity and by diffusion into porosity not participating in advective mass transport. These tests ruled out conceptualizing the Culebra as a homogeneous single-porosity medium.

Additional tracer tests have recently been conducted at the H-11 and H-19 hydropads (Meigs et al., 1997). Elements in the design of these tests focused on characterizing diffusion into diffusive porosity. First, single-well, injection-withdrawal (SWIW) tracer tests are used to identify diffusion into diffusive porosity. Tracers are injected into the formation, and following a short rest period they are pumped back out. Because advection is presumed to occur along the same pathways during injection and withdrawal, the effects of heterogeneity are believed to be minimized during a SWIW tracer test. When the tracer is pumped back out of the formation, the tracer recovery curve will show tailing if diffusion has occurred.

Second, two different conservative tracers having different free-water diffusion coefficients were injected simultaneously during convergent-flow tests. These tests can help to distinguish between diffusion and other mechanisms (e.g., advection) as the cause of physical retardation. If diffusion into diffusive porosity is an important mechanism for mass transport, the tracer with the highest free-water diffusion coefficient should travel farther into diffusive porosity, and its breakthrough curve will be different from the tracer with the lower free-water diffusion coefficient. In addition, tracer injections during convergent-flow tests were repeated at different pumping rates. In these tests, the advective travel time is increased when the pumping rate is lowered, increasing the Damkohler number, and the time for diffusion is increased. SWIW test data from both the H-11 and H-19 hydropads show evidence that multiple-rate diffusion processes affect the recovery curves (Meigs et al., 1997). Cumulative mass recovery during the withdrawal phase of the tracer test should be very rapid if either homogeneous or heterogeneous single-porosity models apply. The H-11 and H-19 data, however, show slow mass

recovery consistent with diffusion. Figure 4-6 shows the mass recovery from the H-11 SWIW test compared to heterogeneous single-porosity and double-porosity, single-rate simulations with two different advective porosities. These results also indicate that SWIW data cannot be adequately fit with either homogeneous or heterogeneous double-porosity, single-rate models. With a single-rate, double-porosity model, the tracer recovery concentration will approach a constant slope of -3/2 on a log-log plot of normalized tracer concentration (C/C_o) versus elapsed time (t) (Figure 4-7). The late-time slope of the data from the H-11 and H-19 SWIW tests was approximately -5/2 rather than -3/2. An excellent fit to the data can be obtained using a multiple-rate diffusion model that uses a statistical distribution of mass-transfer rates (α_n) and capacity coefficients (β_n) (Figure 4-8). Figure 4-9 shows the distributions of diffusion rates used to match the data in Figure 4-8. These diffusion-rate distributions are not unique because similar fits could be obtained using different values of advective and diffusive porosity (yielding different distributions of diffusion rates).

Multiple-well, convergent-flow data appear to exhibit evidence of heterogeneity and diffusion into diffusive porosity (Meigs et al., 1997). Preliminary attempts to match the convergent-flow data with an anisotropic, single-porosity model failed. Heterogeneity is required to capture the variations in the six tracer breakthrough curves. Numerical simulations of tracer-test data with heterogeneous single- and double-porosity models suggested that the data cannot be adequately modeled without diffusion into diffusive porosity (Figure 4-10). Heterogeneous single-porosity models cannot simultaneously match the peak concentrations and arrival times of multiple tracer-recovery curves. Heterogeneous single-rate, double-porosity models can match individual breakthrough curves quite well. However, when the parameters used to match data from one pumping rate are used simulate the breakthrough curve for another pumping rate the match is not satisfactory (Figure 4-11). With a single-rate, double-porosity model, peak heights will be lower for lower pumping rates, unless the diffusion rates are relatively fast, so that the effects of the center of the matrix block (non-infinite diffusion) are felt. A model with multiple rates of diffusion can produce peak heights that are similar for the two pumping rates used for the H-19 testing.

In summary, the Culebra displays non-uniform hydraulic and transport properties both horizontally and vertically. This has been demonstrated with both hydraulic and tracer tests (Beauheim et al., 1997; Meigs et al., 1997). In some locations (e.g., H-19), the upper portion of the Culebra has a much lower permeability and does not appear to provide pathways for rapid transport. There are multiple scales of porosity within the Culebra, including fractures ranging from micro-scale to large, vuggy zones, and interparticle porosity. Flow occurs within fractures, within vugs where they are connected by fractures, and, in some locations, within interparticle porosity (e.g., interbeds of silty dolomite). Variability in peak arrival time in breakthrough curves between the H-11 and the H-19 hydropads suggests that the types of porosity contributing to rapid advective transport may vary spatially. The tracer test data show slow cumulative mass recovery consistent with diffusion into diffusive porosity. The simulations further suggest that both the single- and multiple-well data cannot adequately be explained using a single-rate, double-porosity model with heterogeneous permeability fields. This suggests that, at the time and length scales of field tracer tests, the Culebra behaves as a heterogeneous, double-porosity, multiple-rate medium.

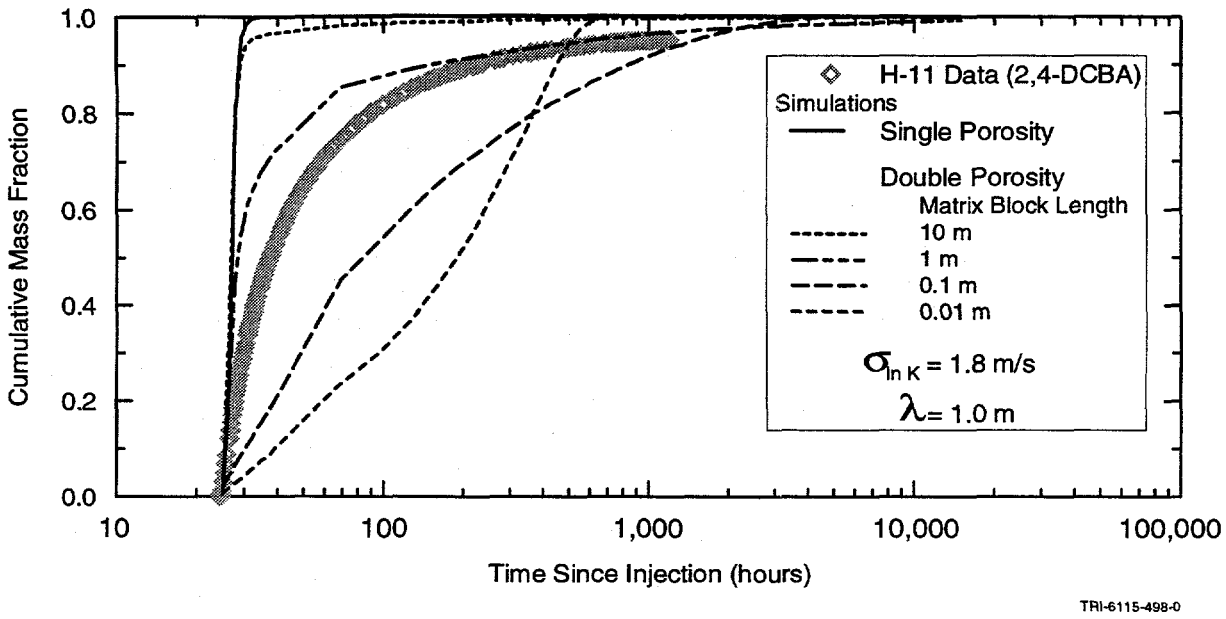

Figure 4-6. Simulated mass recovery curves for H-11 SWIW test for different advective porosities and matrix block lengths compared to observed data (Meigs et al., 1997).

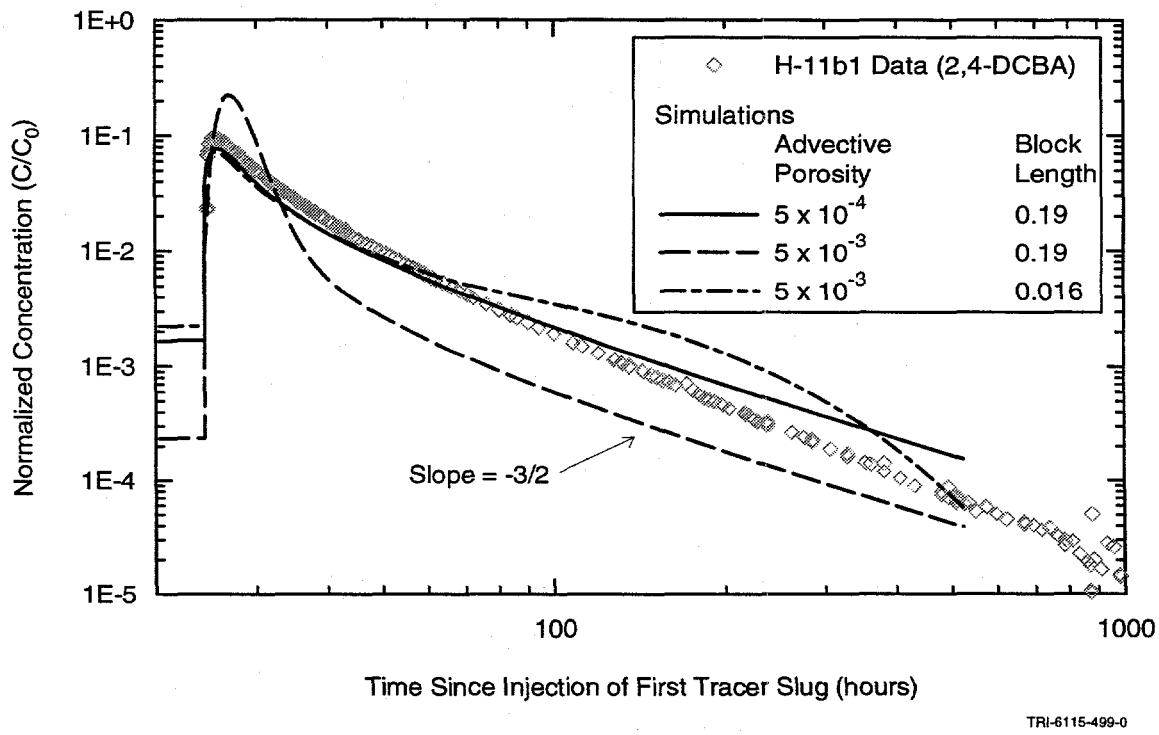

Figure 4-7. Simulated concentration vs. time curves for H-11 SWIW test for different advective porosities and matrix block lengths compared to observed data (Meigs et al., 1997).

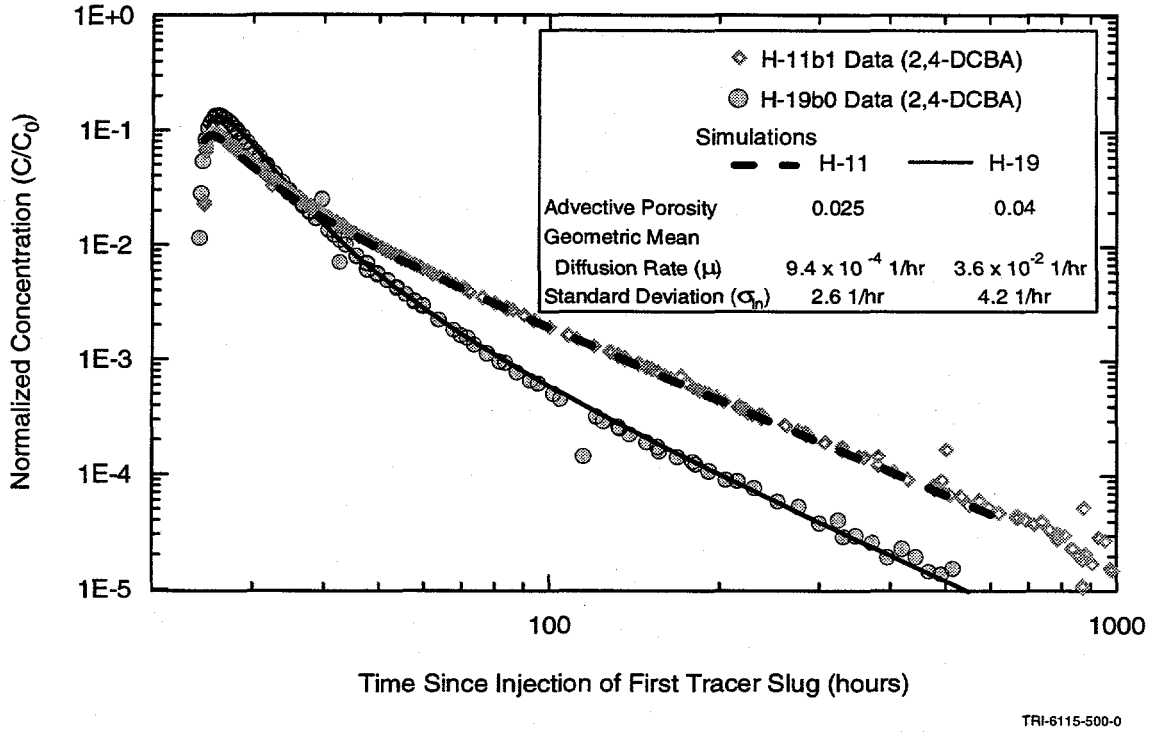

Figure 4-8. Simulated concentration vs. time curves for H-11 and H-19 SWIW tests with the multirate, double-porosity model plotted with observed data (Meigs et al., 1997).

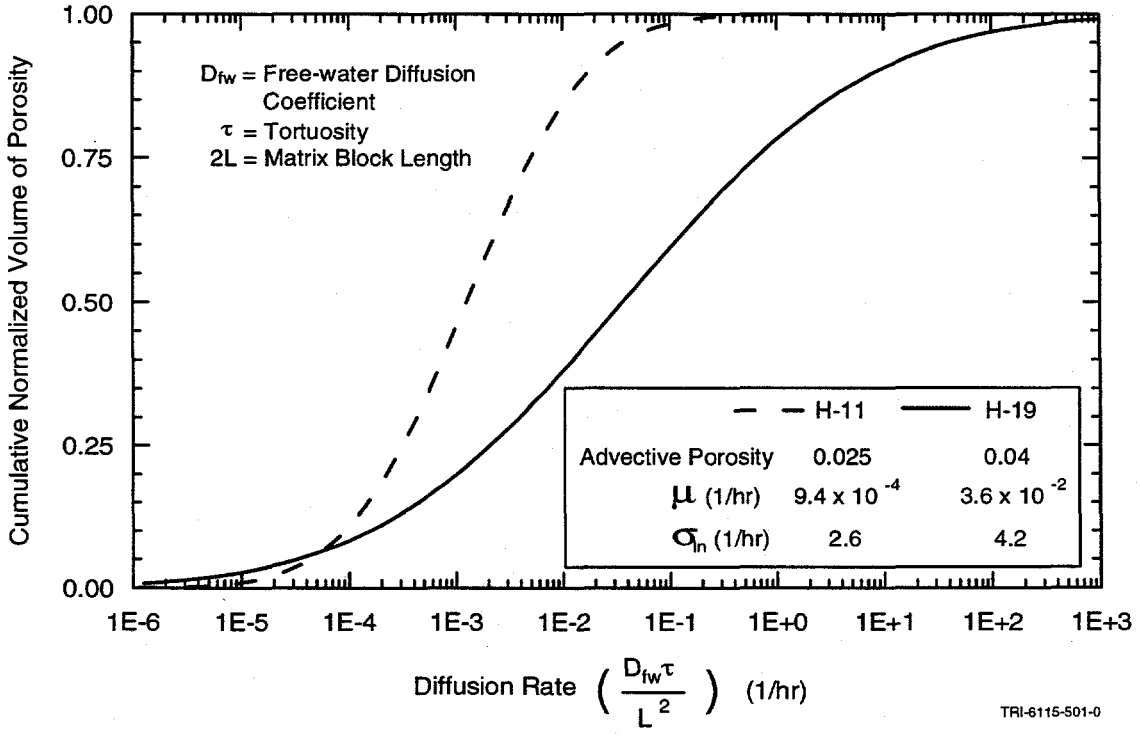

Figure 4-9. Diffusion rate coefficient cumulative distribution function for H-11 and H-19 SWIW test simulations shown in Figure 4-8 (Meigs et al., 1997).

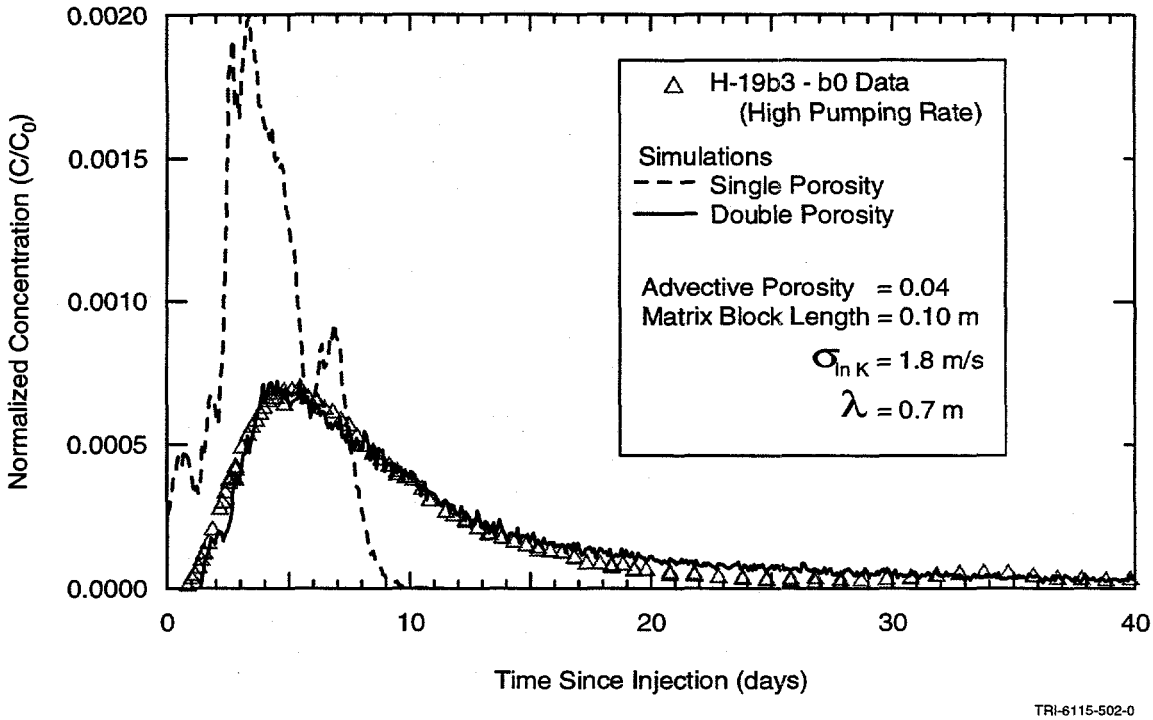

Figure 4-10. Simulated breakthrough curves for multiple-well convergent-flow test data, H-19b3-b0 path, using heterogeneous, single- and double-porosity models (Meigs et al., 1997).

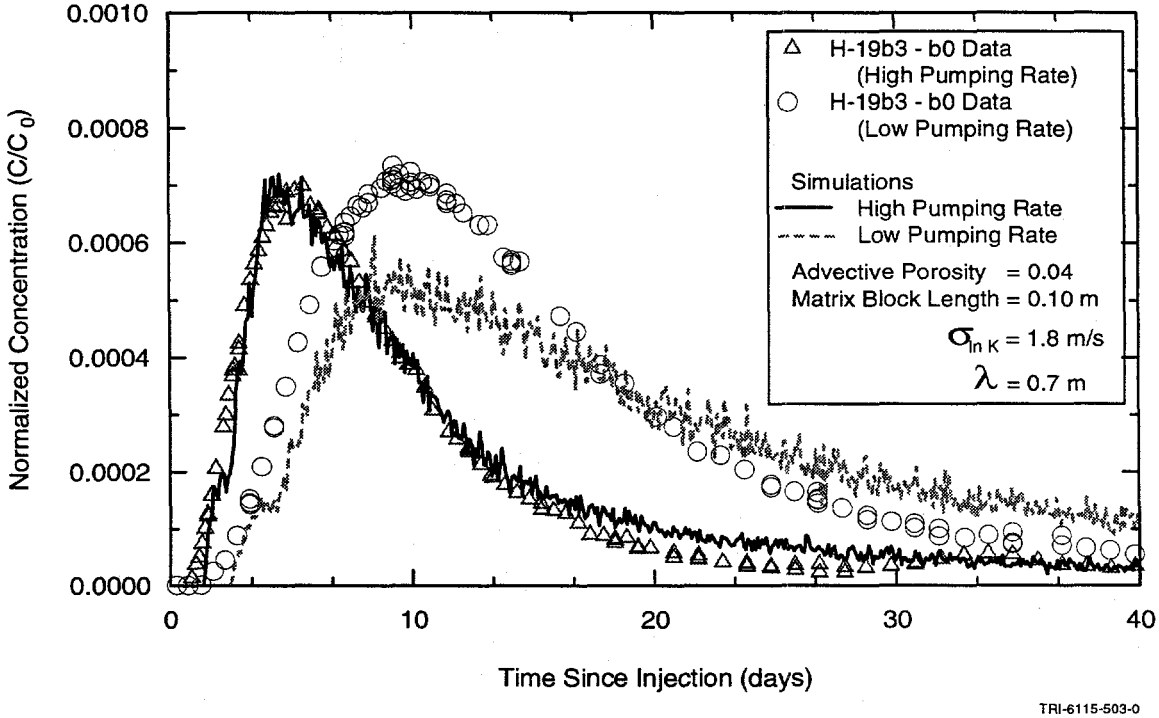

Figure 4-11. Simulated breakthrough curves for multiple-well convergent-flow test data, H-19b3-b0 path, using heterogeneous, single-rate double-porosity model for two different pumping rates.

5. CONCLUSIONS

Across most of the WIPP area, Culebra stratigraphy changes very little. Spatial variations in the hydraulic character of the Culebra primarily reflect variations in post-depositional fracturing and pore-filling cements. Transport processes within the Culebra are complicated by this geologic heterogeneity.

Advective transport occurs mainly in fractures and irregular interbeds of silty dolomite, and the distribution of these features changes vertically through the Culebra. The uppermost Culebra unit, CU-1, is dominated by bedding-plane fractures and local subvertical fractures that bound large tabular blocks. The middle Culebra units, CU-2 and CU-3, are intensely fractured with a hierarchy of superimposed block sizes. The lower Culebra unit, CU-4, displays bedding-plane fractures that form intermediate-scale tabular blocks. CU-1 contains several continuous interbeds of silty dolomite near the top and base. CU-2 and CU-3 contain more abundant, thinner, and more discontinuous interbeds of silty dolomite, while CU-4 contains very little silty dolomite. Fracture-bounded blocks containing well-indurated dolomite with intercrystalline porosity and intercrystalline porosity with vugs can be conceptualized as diffusive porosity zones.

Because the size of fracture-bounded blocks within the Culebra is so variable at a single location, the simplest mathematical model of Culebra transport, valid over all scales, is a double-porosity, multiple-rate model. Multiple-rate, double-porosity models differ conceptually from the classic single-rate, double-porosity model. A single-rate model allows only one diffusive-porosity zone described by a constant size, geometry, and diffusion characteristics, while a multiple-rate model allows diffusive mass-transfer into a number of diffusive-porosity zones described by varying size, geometry, and diffusion characteristics.

The character of transport in a double-porosity medium varies with advective travel length or advective travel time. At short advective travel lengths or advective travel times, diffusion occurs too slowly when compared with advection, and breakthrough curves at the advective travel length will show single-porosity behavior, where only the advective porosity participates in transport. As the advective travel length or advective travel time increases, significant diffusion will occur. The leading edge of breakthrough curves from a pulse input will show physical retardation from mass loss into the diffusive porosity, and the trailing edge of breakthrough curves will show tailing as solutes diffuse out of the diffusive porosity more slowly than they advect. As the advective travel distance increases further, diffusion becomes more significant. At very large advective travel distances or advective travel times, solutes appear to diffuse into and out of diffusive porosity zones instantaneously when compared with the advective travel time. Under these circumstances, breakthrough curves will show single-porosity behavior consistent with the local equilibrium assumption (LEA). When the LEA is valid, both advective and diffusive porosity fully participate in transport.

A dimensionless ratio of the advective travel time and a scaled-time constant for diffusion, the Damkohler number, can be used as a metric to assess the behavior of any diffusive-porosity zone described in a multiple-rate model. At a Damkohler number of less than 10^{-2}, diffusion into the diffusive zone occurs too slowly to affect transport significantly. At a Damkohler number of 100, diffusion occurs instantaneously relative to advection, and the LEA is valid.

Critical length scales at which the Damkohler number equals 10^{-2} or 100 are calculated using estimated parameters for the Culebra units at the H-19 hydropad and an arbitrary pore-water velocity of 1 m/yr. Although the results are qualitative, critical length-scales estimates yield insight into the general transport behavior in the Culebra. Based upon these analyses, the Culebra can be expected to show vertically heterogeneous diffusion behavior. At field scales, transport in the Culebra will reflect multiple rates of diffusion from the different sizes of diffusive-porosity zones. The length scales at which transport through CU-2/CU-3 and CU-4 can be modeled as single-rate, double-porosity medium are approximately the same. Critical length scales for CU-1 are much larger. Culebra length scales for differences between intercrystalline porosity and intercrystalline porosity containing vugs may be negligible for these units. At relatively small scales, e.g., scale of a convergent flow tracer test, the Damkohler numbers of smaller diffusive zones may approach 100, while the larger blocks will still have relatively low Damkohler numbers. Finally, a physically-retarded, single-rate, double-porosity model may adequately simulate transport through CU-2/CU-3 and CU-4 at the WIPP-site scale.

Culebra transport experiments have been conducted at laboratory and field-length scales. Both reactive and non-reactive tracer tests have been conducted on intact core samples from the Culebra. At the length and time scale of these tests, evidence of significant diffusion was not observed, suggesting that at the laboratory scale the Culebra behaves as a single-porosity medium where only the advective porosity participates in transport. Non-reactive field tracer tests conducted in the Culebra show strong double-porosity behavior. In addition, most of the data from these tests cannot be interpreted with a single-rate, double-porosity model, and a multiple-rate, double-porosity model provides the best mathematical and conceptual match to the data.

6. REFERENCES

Atkinson, B.K., and P.G. Meredith. 1987. "The Theory of Subcritical Crack Growth with Applications to Minerals and Rocks," *Fracture Mechanics of Rock*. Ed. B.K. Atkinson. London; New York, NY: Academic Press. 111-166. (Copy on file in the Sandia WIPP Central Files (SWCF), Sandia National Laboratories, Albuquerque, NM as WPO#43880.)

Bahr, J.M., and J. Rubin. 1987. "Direct Comparison of Kinetic and Local Equilibrium Formulations for Solute Transport Affected by Surface Reactions," *Water Resources Research*. Vol. 23, no. 3, 438-452.

Bear, J., and A. Verruijt. 1987. *Modeling Groundwater Flow and Pollution: With Computer Programs for Sample Cases*. Dordrecht; Boston: D. Reidel Publishing Company; Norwell, MA: Sold and Distributed in the U.S. and Canada by Kluwer Academic Publishers. 414 pp.

Beauheim, R.L. 1987. *Interpretations of Single-Well Hydraulic Tests Conducted at and Near the Waste Isolation Pilot Plant (WIPP) Site, 1983-1987*. SAND87-0039. Albuquerque, NM: Sandia National Laboratories. (Available from the National Technical Information Service (NTIS), Springfield, VA as DE88012110/XAB.)

Beauheim, R.L. 1996. "Culebra Transmissivity Data." Records Package. Albuquerque, NM: Sandia National Laboratories. (Copy on file in the Sandia WIPP Central Files (SWCF), Sandia National Laboratories, Albuquerque, NM as WPO#35406.)

Beauheim, R.L., and R.M. Holt. 1990. "Hydrogeology of the WIPP Site," *Geological and Hydrological Studies of Evaporites in the Northern Delaware Basin for the Waste Isolation Pilot Plant (WIPP), New Mexico, Field Trip #14 Guidebook, November 1-4, 1990*. Leaders: D. Powers, R. Holt, R.L. Beauheim, and N. Rempe. SAND90-2035J. Dallas, TX: Dallas Geological Society. 131-179. (SAND90-2035J is on file in the Sandia WIPP Central Files (SWCF), Sandia National Laboratories, Albuquerque, NM as WPO#29377.)

Beauheim, R.L., L.C. Meigs, and P.B. Davies. 1997. "Rationale for the H-19 and H-11 Tracer Tests at the WIPP Site," *Disposal of Radioactive Waste, Field Tracer Transport Experiments, Proceedings of the First GEOTRAP Workshop, Cologne, Germany, August 28-30, 1996*. SAND96-2735C. Albuquerque, NM: Sandia National Laboratories. (SAND96-2735C is available from the National Technical Information Service (NTIS), Springfield, VA as DE97002648/XAB.)

Braitsch, O. 1971. *Salt Deposits, Their Origin and Composition*. Translated by P.J. Burek and A.E.M. Nairn in consultation with A.G. Herrmann and R. Evans. Berlin; New York: Springer-Verlag. 297 pp.

Brush, L.H. 1996. "Culebra Dissolved Actinide Coefficients (Kd's)." Albuquerque, NM: Sandia National Laboratories. (Copy on file in the Sandia WIPP Central Files (SWCF), Sandia National Laboratories, Albuquerque, NM as WPO#38231.)

Bryan, C. 1996. "Non-Salado Adsorption Studies." Albuquerque, NM: Sandia National Laboratories. (Copy on file in the Sandia WIPP Central Files (SWCF), Sandia National Laboratories, Albuquerque, NM as WPO#38473.)

Cauffman, T.L., A.M. LaVenue, and J.P. McCord. 1990. *Ground-Water Flow Modeling of the Culebra Dolomite. Volume II: Data Base*. SAND89-7068/2. Albuquerque, NM: Sandia National Laboratories. (Available from the National Technical Information Service (NTIS), Springfield, VA as DE91007903/XAB.)

Coats, K.H., and B.D. Smith. 1964. "Dead-End Pore Volume and Dispersion in Porous Media," *Society of Petroleum Engineers Journal*. Vol. 4, no. 1, 73-84. (Copy on file in the Sandia WIPP Central Files (SWCF), Sandia National Laboratories, Albuquerque, NM as WPO#46379.)

COLOG. 1996. "Fluid Logging Results." Albuquerque, NM: Sandia National Laboratories. (Copy on file in the Sandia WIPP Central Files (SWCF), Sandia National Laboratories, Albuquerque, NM as WPO#38402.)

Corbet, T.F., and P.M. Knupp. 1996. *The Role of Regional Groundwater Flow in the Hydrogeology of the Culebra Member of the Rustler Formation at the Waste Isolation Pilot Plant (WIPP), Southeastern New Mexico*. SAND96-2133. Albuquerque, NM: Sandia National Laboratories. (Available from the National Technical Information Service (NTIS), Springfield, VA as DE97002327/XAB.)

Crawley, M.E. 1988. *Hydrostatic Pressure and Fluid Density Distribution of the Culebra Dolomite Member of the Rustler Formation near the Waste Isolation Pilot Plant, Southeastern New Mexico*. DOE/WIPP 88-030. Carlsbad, NM: Westinghouse Electric Corporation. (Available from the National Technical Information Service (NTIS), Springfield, VA as DE89003550/XAB.)

Damkohler, G. 1936. "Einflüsse der Strömung, Diffusion und des Wärmeüberganges auf die Leistung von Reaktionsöfen. I. Allgemeine Gesichtspunke für die Übertragung eines chemischen Prozesses aus dem Kleinen ins Große," *Zeitschrift für Elektrochemie und Angewandte Physikalische Chemie*. Vol. 42, no. 12, 846-862. (In German.) (Copy on file in the Sandia WIPP Central Files (SWCF), Sandia National Laboratories, Albuquerque, NM as WPO#46380.)

Davies, P.B. 1989. *Variable-Density Ground-Water Flow and Paleohydrology in the Waste Isolation Pilot Plant (WIPP) Region, Southeastern New Mexico*. Open-File Report 88-490. Albuquerque, NM: U.S. Geological Survey. (Copy on file in the Sandia WIPP Central Files (SWCF), Sandia National Laboratories, Albuquerque, NM as WPO#38854.)

Durney, D.W., and J.G. Ramsay. 1973. "Incremental Strains Measured by Syntectonic Crystal Growths," *Gravity and Tectonics*. Eds. K. A. DeJong and R. Scholten. New York, NY: John

Wiley & Sons. 67-96. (Copy on file in the Sandia WIPP Central Files (SWCF), Sandia National Laboratories, Albuquerque, NM as WPO#43882.)

Engelder, T. 1987. "Joints and Shear Fractures in Rock," *Fracture Mechanics of Rock*. Ed. B.K. Atkinson. London; Orlando, FL: Academic Press. 27-69. (Copy on file in the Sandia WIPP Central Files (SWCF), Sandia National Laboratories, Albuquerque, NM as WPO#46355.)

Fetter, C.W. 1993. *Contaminant Hydrogeology*. New York, NY: Macmillan Publishing Company. 458 pp.

Haggerty, R., and S.M. Gorelick. 1995. "Multiple-Rate Mass Transfer for Modeling Diffusion and Surface Reactions in Media with Pore-Scale Heterogeneity," *Water Resources Research*. Vol. 31, no. 10, 2383-2400.

Holt, R.M. 1993. *Sedimentary Textures, Structures, and Lithofacies in the Salado Formation: A Guide for Recognition, Classification, and Interpretation*. DOE/WIPP 93-056. Carlsbad, NM: Westinghouse Electric Corporation. (opy on file in the Sandia WIPP Central Files (SWCF), Sandia National Laboratories, Albuquerque, NM as WPO#43752.)

Holt, R.M. 1996. "Hydrostratigraphy of the Culebra Dolomite Member of the Rustler Formation in the WIPP Region." Records Package. Albuquerque, NM: Sandia National Laboratories. (Copy on file in the Sandia WIPP Central Files (SWCF), Sandia National Laboratories, Albuquerque, NM as WPO#38231.)

Holt, R.M., and D.W. Powers. 1984. *Geotechnical Activities in the Waste Handling Shaft Waste Isolation Pilot Plant (WIPP) Project Southeastern New Mexico*. WTSD-TME 038. Carlsbad, NM: U.S. Department of Energy, Waste Isolation Pilot Plant. (Available from the National Technical Information Service (NTIS), Springfield, VA as DE86004328/XAB.)

Holt, R.M., and D.W. Powers. 1986. *Geotechnical Activities in the Exhaust Shaft*. DOE-WIPP 86-008. Carlsbad, NM: U.S. Department of Energy. (Copy on file in the Sandia WIPP Central Files (SWCF), Sandia National Laboratories, Albuquerque, NM as WPO#41696.)

Holt, R.M., and D.W. Powers. 1988. *Facies Variability and Post-Depositional Alteration Within the Rustler Formation in the Vicinity of the Waste Isolation Pilot Plant, Southeastern New Mexico*. DOE/WIPP 88-004. Carlsbad, NM: Westinghouse Electric Corporation. (Available from the National Technical Information Service (NTIS), Springfield, VA as DE88013969/XAB.)

Holt, R.M., and D.W. Powers. 1990. *Geologic Mapping of the Air Intake Shaft at the Waste Isolation Pilot Plant*. DOE-WIPP 90-051. Carlsbad, NM: Westinghouse Electric Corporation. (Available from the National Technical Information Service (NTIS), Springfield, VA as DE91017780/XAB.)

Jones, T.L., V.A. Kelley, J.F. Pickens, D.T. Upton, R.L. Beauheim, and P.B. Davies. 1992. *Integration of Interpretation Results of Tracer Tests Performed in the Culebra Dolomite at the Waste Isolation Pilot Plant Site.* SAND92-1579. Albuquerque, NM: Sandia National Laboratories. (Available from the National Technical Information Service (NTIS), Springfield, VA as DE93003235/XAB.)

Kelley, V.A., and G.J. Saulnier, Jr. 1990. *Core Analyses for Selected Samples from the Culebra Dolomite at the Waste Isolation Pilot Plant Site.* SAND90-7011. Albuquerque, NM: Sandia National Laboratories. (Available from the National Technical Information Service (NTIS), Springfield, VA as DE91006752/XAB.)

Lappin, A.R. 1988. *Summary of Site-Characterization Studies Conducted from 1983 Through 1987 at the Waste Isolation Pilot Plant (WIPP) Site, Southeastern New Mexico.* SAND88-0157. Albuquerque, NM: Sandia National Laboratories. (Available from the National Technical Information Service (NTIS), Springfield, VA as DE88013140.)

Lappin, A.R., R.L. Hunter, D.P. Garber, and P.B. Davies, eds. 1989. *Systems Analysis, Long-Term Radionuclide Transport, and Dose Assessments, Waste Isolation Pilot Plant (WIPP), Southeastern New Mexico; March 1989.* SAND89-0462. Albuquerque, NM: Sandia National Laboratories. (Available from the National Technical Information Service (NTIS), Springfield, VA as DE89014586/XAB.)

LaVenue, A.M., A. Haug, and V.A. Kelley. 1988. *Numerical Simulation of Ground-Water Flow in the Culebra Dolomite at the Waste Isolation Pilot Plant (WIPP) Site: Second Interim Report.* SAND88-7002. Albuquerque, NM: Sandia National Laboratories. (Available from the National Technical Information Service (NTIS), Springfield, VA as DE8809795/XAB.)

LaVenue, A.M., T.L. Cauffman, and J.F. Pickens. 1990. *Ground-Water Flow Modeling of the Culebra Dolomite. Volume I: Model Calibration.* SAND89-7068/1. Albuquerque, NM: Sandia National Laboratories. (Available from the National Technical Information Service (NTIS), Springfield, VA as DE91004924/XAB.)

Lucero, D. 1996. "Results of Core-Column Tests." Records Package. Albuquerque, NM: Sandia National Laboratories. (Copy on file in the Sandia WIPP Central Files (SWCF), Sandia National Laboratories, Albuquerque, NM as WPO#40975.)

Meigs, L. 1996. "H-19 Tracer Test Data." Records Package. Albuquerque, NM: Sandia National Laboratories. (Copy on file in the Sandia WIPP Central Files (SWCF), Sandia National Laboratories, Albuquerque, NM as WPO#37452.)

Meigs, L.C., R.L. Beauheim, J.T. McCord, Y.W. Tsang, and R. Haggerty. 1997. "Design, Modeling, and Current Interpretations of the H-19 and H-11 Tracer Tests at the WIPP Site," *Disposal of Radioactive Waste, Field Tracer Transport Experiments, Proceedings of the First GEOTRAP Workshop, Cologne, Germany, August 28-30, 1996.* SAND96-2796C.

Albuquerque, NM: Sandia National Laboratories. (Available from the National Technical Information Service (NTIS), Springfield, VA as DE97004035.)

Mercer, J.W., and B.R. Orr. 1979. *Interim Data Report on the Geohydrology of the Proposed Waste Isolation Pilot Plant Site, Southeast New Mexico.* USGS Water-Resources Investigations Report 79-98. Albuquerque, NM: U.S. Geological Survey. p. 92. (Available from the National Technical Information Service (NTIS), Springfield, VA as PB80-128762.)

Morrow, D.W. 1982. "Descriptive Field Classification of Sedimentary and Diagenetic Breccia Fabrics in Carbonate Rocks," *Bulletin of Canadian Petroleum Geology.* Vol. 30, no. 3, 227-229. (Copy on file in the Sandia WIPP Central Files (SWCF), Sandia National Laboratories, Albuquerque, NM as WPO#44071.)

Neretnieks, I. 1980. "Diffusion in the Rock Matrix: An Important Factor in Radionuclide Retardation?," *Journal of Geophysical Research.* Vol. 85, no. B8, 4379-4397. (Copy on file in the Sandia WIPP Central Files (SWCF), Sandia National Laboratories, Albuquerque, NM as WPO#43884.)

Powers, D.W., and R.M. Holt. 1990. "Sedimentology of the Rustler Formation Near the Waste Isolation Pilot Plant (WIPP) Site," *Geological and Hydrological Studies of Evaporites in the Northern Delaware Basin for the Waste Isolation Pilot Plant (WIPP), New Mexico, Field Trip #14 Guidebook, November 1-4, 1990.* Leaders: D. Powers, R. Holt, R.L. Beauheim, and N. Rempe. Dallas, TX: Dallas Geological Society. 79-106. (Copy on file in the Sandia WIPP Central Files (SWCF), Sandia National Laboratories, Albuquerque, NM as WPO#41633.)

Powers, D.W., and R.M. Holt. 1995a. "Gatuna Formation (Miocene to Pleistocene), Geology and Paleohydrology." Prepared for Westinghouse Electric Corporation, Carlsbad, New Mexico.

Powers, D.W., and R.M. Holt. 1995b. "Regional Geological Processes Affecting Rustler Hydrogeology." Prepared for Westinghouse Electric Corporation, Carlsbad, New Mexico. (Copy on file in the Sandia WIPP Central Files (SWCF), Sandia National Laboratories, Albuquerque, NM as WPO#44173.)

Reeves, M., V.A. Kelley, and J.F. Pickens. 1987. *Regional Double-Porosity Solute Transport in the Culebra Dolomite: An Analysis of Parameter Sensitivity and Importance at the Waste Isolation Pilot Plant (WIPP) Site.* SAND87-7105. Albuquerque, NM: Sandia National Laboratories. (Available from the National Technical Information Service (NTIS), Springfield, VA as DE8804730/XAB.)

Sardin, M., D. Schweich, F.J. Leij, and M.T. van Genuchten. 1991. "Modeling the Nonequilibrium Transport of Linearly Interacting Solutes in Porous Media: A Review," *Water Resources Research.* Vol. 27, no. 9, 2287-2307.

Sewards, T. 1991. *Characterization of Fracture Surfaces in Dolomite Rock, Culebra Dolomite Member, Rustler Formation*. SAND90-7019. Albuquerque, NM: Sandia National Laboratories. (Available from the National Technical Information Service (NTIS), Springfield, VA as DE91014548/XAB.)

Swift, P. 1992. "Fracture Orientations in Outcrops of the Rustler Formation and Dewey Lake Red Beds, WIPP Area." Internal Memoranda to File. Albuquerque, NM: Sandia National Laboratories. (Reprinted in Appendix D of this report.)

van Genuchten, M.T., and P.J. Wierenga. 1976. "Mass-Transfer Studies in Sorbing Porous Media. 1. Analytical Solutions," *Soil Science Society of America Journal*. Vol. 40, no. 4, 473-480. (Copy on file in the Sandia WIPP Central Files (SWCF), Sandia National Laboratories, Albuquerque, NM as WPO#43879.)

Zaitsev, Y.V. 1985. "Inelastic Properties of Solids with Random Cracks," *Mechanics of Geomaterials: Rocks, Concretes, Soils*. Ed. Z.P. Bazant. Chichester, England; New York: John Wiley & Sons. 89-128.

APPENDIX A
Formation Factor

The formation factor referred to in this report is a media property that is the ratio of the resistance of a sample containing an electrolyte solution (R_s) to the resistance of an equivalent volume of electrolyte solution with the same dimensions (R_w) (Dullien, 1992)

$$F = \frac{R_s}{R_w} \tag{A-1}$$

Equation A-1 is considered to be an analog to the diffusive formation factor. For a particular solute, the diffusive formation factor is defined as the ratio between the diffusion coefficient through the porous medium and the diffusion coefficient in water. The formation factor is often related to the medium by

$$F = \frac{1}{\phi_v \xi} \tag{A-2}$$

where ϕ_v is the volumetric porosity and ξ is the "diffusive tortuosity" (e.g., Kelley and Saulnier, 1990). The diffusive tortuosity term, ξ, accounts for the tortuous and constrictive nature of the pathways through the medium.

An alternative expression for the formation factor can be derived using Equation A-1. The resistivity of the sample can be described by

$$R_s = r_e \int_0^L \frac{(\tau)^{1/2}}{A_p(x)} dx \tag{A-3}$$

where r_e is the resistivity of the electrolyte, L is the sample length, $A_p(x)$ is the cross-sectional area of the pore spaces perpendicular to the direction that current is applied (x), and τ is the hydraulic tortuosity: the square of the effective flow distance divided by the actual flow distance. The resistivity of an equivalent size and volume of electrolyte solution is (Dullien, 1992)

$$R_w = r_e \frac{L}{A} \tag{A-4}$$

where A is the total area of the sample perpendicular to the applied current. Because this ratio is independent of parameters related to the resistivity of the electrolyte solution, the formation factor depends only on media characteristics and, for a hydraulic tortuosity independent of x, can be written as

$$F = \frac{(\tau)^{\frac{1}{2}}}{\phi_A^H} \tag{A-5}$$

where $\phi_A{}^H$ [L^2/L^2] is the harmonic mean of the areal porosity along the direction x. Within a particular geologic medium, the tortuosity term, τ [L^2/L^2], can readily be visualized and qualified for different types of porosity present in the geologic medium. The harmonic mean of the areal porosity, however, is more difficult to conceptualize.

A simple example of the behavior of ϕ_A^H can be constructed to help visualize how this parameter will vary in a porous geologic material. If we consider the areal porosity to be randomly distributed within a block of geologic material with a log-normal distribution, a mean of $P = E[\ln(\phi_A)]$, and a variance of $\ln(\phi_A)$ equal to σ_p^2, the geometric mean of the areal porosity from 0 to L would be

$$\phi_A^G = \exp\left\{\frac{1}{L}\int_0^L \ln[\phi_A(x)]dx\right\} \tag{A-6}$$

The arithmetic mean would be

$$\phi_A^A = \phi_A^G \exp\left(\frac{\sigma_p^2}{2}\right) \tag{A-7}$$

and the harmonic mean would be

$$\phi_A^H = \phi_A^G \exp\left(-\frac{\sigma_p^2}{2}\right) \tag{A-8}$$

This series of equations illustrates that the harmonic mean of the areal porosity in a block of geologic material will decrease rapidly as the variance of the areal porosity increases. Therefore, large formation factors reflect a very heterogeneous porosity distribution within the rock and a tortuous solute pathway.

References

Dullien, F.A.L. 1992. *Porous Media: Fluid Transport and Pore Structure*. 2nd ed. San Diego, CA: Academic Press, Inc. 574 pp.

Kelley, V.A., and G.J. Saulnier, Jr. 1990. *Core Analyses for Selected Samples from the Culebra Dolomite at the Waste Isolation Pilot Plant Site.* SAND90-7011. Albuquerque, NM: Sandia National Laboratories. (Available from the National Technical Information Service (NTIS), Springfield, VA as DE91006752/XAB.)

APPENDIX B
Hydraulic Properties for Culebra Samples Determined from Laboratory Core Tests

Table B-1 contains data used to estimate the mean and median values of hydraulic properties for Culebra porosity types. All hydraulic property data, except those from the well H-19b4, are derived from Kelley and Saulnier (1990). H-19b4 samples were recently (1996) analyzed by Terra Tek and are reported here for the first time. Hydraulic conductivity values are determined from reported permeability values and location-specific fluid density measurements. Sample descriptors are:

IC - intercrystalline porosity (well-indurated dolomite)

F - fracture porosity

V - vuggy porosity

IP - interparticle porosity (silty dolomite)

MV - microvugs

GV - gypsum-cemented vugs

GF - gypsum-cemented fractures.

Descriptors for data from Kelley and Saulnier (1990) are based on their geologic descriptions. Descriptors for data from H-19b4 are based on geologic descriptions by the author.

Table B-1. Hydraulic Properties for Culebra Samples Determined from Laboratory Core Tests

Well ID	Test	Sample ID	Sample Description	Porosity	Formation Factor	Horizontal Hydraulic Conductivity (m/s)	Vertical Hydraulic Conductivity (m/s)
H-2a	core	H-2a-1	IC,F,GV	0.116		2.5E-09	
H-2a	core	H-2a-2	IC,GF	0.131		9.8E-11	
H-2b	core	1-1	IC,MV	0.141		2.0E-09	2.0E-09
H-2b	core	2-1/3-1	IC,V,GF	0.154		6.8E-10	9.8E-11
H-2b	core	1-2	IC,V,IP?	0.118			
H-2b	core	2-2/3-2	IC,V	0.103		1.9E-10	3.6E-09
H-2b	core	H-2b1-1	IC,V,GV	0.082		2.4E-09	
H-2b	core	H-2b1-1F	IC,V,GV	0.105	326.77	3.0E-10	
H-2b	core	H-2b1-2	IC,V,GV	0.142		6.0E-09	
H-2b	core	H-2b1-3	IC,V	0.153		2.7E-09	
H-3b2	core	1-3	IP?	0.188			4.2E-08
H-3b2	core	1-4	IC,V	0.168			3.3E-08
H-3b3	core	2-3/3-3	IC,V,GV,F	0.18		1.0E-07	
H-3b3	core	2-4/3-4V	IC,V,GV	0.202			1.2E-08
H-3b3	core	1-6/3-6V	IP,MV	0.244			5.3E-09
H-3b3	core	2-5/3-5	IC,IP,MV,GV	0.205		2.1E-08	5.6E-09
H-4b	core	1-9	IP	0.297			5.2E-07

Table B-1. Hydraulic Properties for Culebra Samples Determined from Laboratory Core Tests

Well ID	Test	Sample ID	Sample Description	Porosity	Formation Factor	Horizontal Hydraulic Conductivity (m/s)	Vertical Hydraulic Conductivity (m/s)
H-4b	core	2-6/3-6V	IP,IC	0.208			5.2E-08
H-5b	core	H-5b-1a	IC,V	0.128		5.3E-10	
H-5b	core	H-5b-1b	IC,V	0.155		8.5E-10	
H-5b	core	H-5b-2	IC,MV,F	0.228		3.9E-08	
H-5b	core	H-5b-2F	IC,MV,F	0.248	12.2	1.4E-07	
H-5b	core	H-5b-3	IC,V	0.133		2.9E-09	8.5E-10
H-6b	core	2-7	IC	0.108		5.0E-10	
H-6b	core	2-8	IC	0.116		8.0E-10	7.0E-10
H-6b	core	1-7	IC	0.107		4.0E-10	5.0E-10
H-6b	core	1-8/3-8V	IP?	0.255			1.7E-08
H-7b1	core	H-7b1-1	IC,V	0.177		1.1E-09	
H-7b1	core	H-7b1-1F	IC,V	0.149	73.49	9.7E-10	
H-7b1	core	H-7b1-2a	IC,V	0.206		9.7E-10	
H-7b1	core	H-7b1-2b	IC,V	0.278			
H-7b2	core	H-7b2-1	IC,V	0.159		3.0E-09	
H-7b2	core	H-7b2-2	IC,V	0.118		9.7E-10	2.4E-09
H-7c	core	H-7c-1a	IC,V	0.13		6.7E-10	
H-7c	core	H-7c-1b	IC,V	0.165			
H-7c	core	H-7c-1F	IC,V	0.138	79.61	1.1E-09	
H-10b	core	H-10b-1	IC	0.089		4.0E-10	
H-10b	core	H-10b-2	IC,F	0.115		7.9E-08	
H-10b	core	H-10b-2F	IC,F	0.066	406.78	1.4E-09	
H-10b	core	H-10b-3	IC,V	0.112		6.4E-09	2.2E-09
H-11 (pad)	core	H-11-1	IC,MV	0.155		5.2E-10	1.5E-09
H-11 (pad)	core	H-11-2	IC,GV,GF	0.105		2.1E-10	
H-11 (pad)	core	H-11-2F	IC,GV,GF	0.104	94.82	4.1E-10	
H-11 (pad)	core	H-11b3-1	IP	0.303		4.8E-08	
H-11 (pad)	core	H-11b3-1F	IP	0.223	36.35	1.7E-08	
H-11 (pad)	core	H-11b3-2	IC,V,F	0.099		5.2E-10	
H-11 (pad)	core	H-11b3-2F	IC,V,F	0.123	101.93	3.5E-09	
H-11 (pad)	core	H-11b3-3	IC,V,GF	0.13		6.1E-08	2.5E-08
H-11 (pad)	core	H-11b3-4	IC,MV	0.152		2.9E-09	
H-11 (pad)	core	H-11b3-4F	IC,MV	0.224	32.74	8.3E-08	
H-19b4	core	C-1	IC,GV	0.147	42.98	5.1E-10	9.5E-10
H-19b4	core	C-2	IC	0.137	60.3	2.2E-10	7.0E-10
H-19b4	core	C-3	IC	0.134	63.57	1.1E-10	1.6E-10

Table B-1. Hydraulic Properties for Culebra Samples Determined from Laboratory Core Tests

Well ID	Test	Sample ID	Sample Description	Porosity	Formation Factor	Horizontal Hydraulic Conductivity (m/s)	Vertical Hydraulic Conductivity (m/s)
H-19b4	core	C-4	IC,V	0.174	53.03	4.8E-10	7.5E-10
H-19b4	core	C-5	IC,V	0.133	77.61	4.3E-09	1.7E-10
H-19b4	core	C-6	IC	0.1	112.73	2.5E-10	4.0E-10
H-19b4	core	C-7	IC,GV,GF	0.109	111.51	1.1E-09	1.0E-08
H-19b4	core	C-8	IC,F	0.1	124.47	1.4E-10	6.0E-07
H-19b4	core	C-9	IC,GF	0.098	139.85	2.1E-11	3.9E-08
H-19b4	core	C-10	IC	0.086	121.08	3.0E-11	3.4E-11
H-19b4	core	C-11	IC	0.102	119.87	1.4E-10	3.6E-11
H-19b4	core	C-12	IC	0.094	134.28	8.9E-09	5.1E-11
H-19b4	core	C-13	IP	0.281	17.56	2.1E-10	6.9E-08
H-19b4	core	C-14	IC,IP	0.091	218.79	8.9E-10	7.8E-11
H-19b4	core	C-15	IC,V	0.195	126.77	3.4E-10	3.1E-08
H-19b4	core	C-16	IC,V	0.152	392.18		3.1E-10
H-19b4	core	C-17	IC,V	0.266	45.16	7.8E-11	3.9E-07
H-19b4	core	C-18	IC,V,F	0.138	150.74	1.2E-08	1.6E-07
H-19b4	core	C-19	IC,V,F	0.197	82.33	1.4E-07	1.3E-08
H-19b4	core	C-20	IC,V,GV	0.199	38.14	4.1E-08	5.8E-08
H-19b4	core	C-21	IC,V,F,GF	0.15	66.59	9.5E-08	2.5E-08
WIPP-12	core	W-12-1a	N/A	0.028			
WIPP-12	core	W-12-1b	IC,V	0.114		1.7E-09	
WIPP-12	core	W-12-2	IC,V,GV,F	0.126		9.8E-09	
WIPP-12	core	W-12-2F	IC,V,GV,F	0.135	47.3	5.9E-07	
WIPP-12	core	W-12-3	IC,F	0.134		2.5E-07	1.6E-08
WIPP-13	core	W-13-1	IC,F	0.143		6.0E-08	
WIPP-13	core	W-13-2	IC,V	0.219		3.6E-08	
WIPP-13	core	W-13-2F	IC,V	0.26	13.26	4.6E-08	
WIPP-13	core	W-13-3a	IP,IC,V	0.179		3.7E-08	
WIPP-13	core	W-13-3b	IP,IC,V	0.097			
WIPP-25	core	W-25-1	IC,F?	0.115		3.6E-06	1.9E-09
WIPP-26	core	W-26-1	IC,MV	0.124		3.9E-10	
WIPP-26	core	W-26-1F	IC,MV	0.112	68.77	3.9E-10	
WIPP-26	core	W-26-2	IC,V	0.126		2.9E-07	5.0E-07
WIPP-26	core	W-26-3	IC,V	0.127		4.8E-10	
WIPP-28	core	W-28-1a	IC,V	0.142			
WIPP-28	core	W-28-1b	IC,V	0.13		5.0E-10	
WIPP-28	core	W-28-2	IP	0.187		3.6E-08	2.0E-08

Table B-1. Hydraulic Properties for Culebra Samples Determined from Laboratory Core Tests

Well ID	Test	Sample ID	Sample Description	Porosity	Formation Factor	Horizontal Hydraulic Conductivity (m/s)	Vertical Hydraulic Conductivity (m/s)
WIPP-28	core	W-28-3	IP	0.17		3.1E-09	2.7E-09
WIPP-28	core	W-28-3F	IP	0.179	26.3	4.0E-09	
WIPP-30	core	W-30-1	IC,V,F	0.128		7.8E-07	4.6E-09
WIPP-30	core	W-30-2	IC,MV	0.15		3.9E-09	3.2E-09
WIPP-30	core	W-30-3a	IC,V	0.176			
WIPP-30	core	W-30-3b	IC,V	0.149		5.4E-09	
WIPP-30	core	W-30-3F	IC,V	0.149	31.49	2.5E-08	
WIPP-30	core	W-30-4	IP,IC,V	0.239		8.2E-08	
AEC-8	core	AEC-8-1	IC,MV	0.079		2.7E-09	
AEC-8	core	AEC-8-1F	IC,MV	0.122	90.09	6.1E-10	
AEC-8	core	AEC-8-2	IC,V	0.109		3.2E-09	

APPENDIX C
Specific Surface Area Measurements on Intact Dolomite Samples

Appendix C errata

Page	Reference	Correction
C-7	Brush, 1996	Brush and Storz, 1996
C-7	Brush, L.H., and L.J. Storz	document title: "Revised Ranges and Probability Distributions of K_ds for Dissolved Pu, Am, U, Th, and Np in the Culebra for the PA Calculations to Support the WIPP CCA."
C-8	(see Brush, 1996)	(see Brush and Storz, 1996)

Specific surface area measurements on intact samples of Culebra materials are reported in Table C-1. These samples were collected by the author and analyzed by J.W. Kelly. Sample descriptions are based on the following descriptors:

IC - intercrystalline porosity (well-indurated dolomite)

IP - interparticle porosity (silty dolomite).

As further documentation of methods and the average value of specific surface area for samples used during Culebra batch-sorption experiments, memoranda from J. W. Kelly and L. Brush are provided.

Table C-1. Specific Surface Area Measurements on Intact Dolomite Samples

Sample	Description	Specific Surface Area (m^2/g)
VPX 25-8-1	IC	0.9
VPX 25-8-1	IC	0.9
VPX 27-7-2	IC	0.5
VPX 27-7-2	IC	0.5
VPX 25-8-3	IC	1.3
VPX 25-8-3	IC	1.3
VPX 26-11B-1	IC	0.9
VPX 26-11B-1	IC	0.9
VPX 28-6-1	IC	1.2
VPX 28-6-1	IC	1.2
VPX 25-8-2	IP	2.6
VPX 25-8-2	IP	2.6
VPX 25-6-2	IP	1.3
VPX 25-6-2	IP	1.3
VPX 27-7-1	IP	0.6
VPX 27-7-1	IP	0.7
VPX 27-7-3	IP	0.7
VPX 27-7-3	IP	0.7

Average value for dolomite used in batch sorption experiments: 1.5

Sandia National Laboratories
Albuquerque, New Mexico 87185

date: 8/19/96

to: Hans W. Papenguth, 6832

from: John W. Kelly, 6832

subject: Surface Area Analysis Results

Attached are results of the surface area analyses that you requested.

The samples were dried/degassed overnight under vacuum at 50 °C and were analyzed for surface area twice using the Micromeritics ASAP-2000 as per TOP-537.

When necessary, samples were broken in order to fit them down the 1 cm-diameter sample tube. Any pieces <3mm generated by doing this were separated and not included in the analyzed portion.

Copy to:
MS 1324 Bob Holt, 6115
MS 1341 Larry Brush, 6832

SAMPLE	Description	m^2/g	5-point r^2
10.9 m2/g standard	NIST lot# 492206	10.7216	0.999994
VPX25-8-2	Silty Dolomite	2.6163	0.999868
VPX25-8-2	Silty Dolomite	2.6103	0.999869
VPX25-8-1	Well Indurated Dolomite	0.8934	0.999863
VPX25-8-1	Well Indurated Dolomite	0.9112	0.999845
VPX28-6-2	Silty Dolomite	1.2826	0.999888
VPX28-6-2	Silty Dolomite	1.2757	0.999883
10.9 m2/g standard	NIST lot# 492206	10.6735	0.999993
VPX27-7-2	Well Indurated Dolomite	0.5005	0.999729
VPX27-7-2	Well Indurated Dolomite	0.5001	0.999558
VPX27-7-1	Fragile Silty Dolomite	0.6478	0.999984
VPX27-7-1	Fragile Silty Dolomite	0.6714	0.999963
VPX27-7-3	Moderately Indurated Silty Dolomite	0.6690	0.999891
VPX27-7-3	Moderately Indurated Silty Dolomite	0.6739	0.999921
10.9 m2/g standard	NIST lot# 492206	10.5824	0.999987
VPX25-8-3	Well Indurated Dolomite with dark gray to	1.2970	0.999794
VPX25-8-3	black material on fracture surfaces	1.3083	0.999784
VPX26-11B-1	Well Indurated Dolomite from between	0.9393	0.999896
VPX26-11B-1	sample locations C-2A-V,C-1-VA,C-3A-V	0.9449	0.999889
VPX28-6-1	Well Indurated Dolomite with Clay and	1.2051	0.999851
VPX28-6-1	FeO_2 stains on fracture surfaces	1.2107	0.999823
10.9 m2/g standard	NIST lot# 492206	10.7927	0.999997

Sandia National Laboratories
Albuquerque, New Mexico 87185

date: 8/22/96

to: Larry Brush, 6832, MS 1341

from: John W. Kelly, 6832

subject: Surface Area Analysis Results

Listed below are results of the surface area analyses that you requested.

The samples were dried/degassed overnight under vacuum at 50 °C, divided into 3 lots and were then analyzed for surface area using the Micromeritics ASAP-2000 as per TOP-537.

SAMPLE	Description	m^2/g	5-point r^2
10.9 m2/g standard	NIST lot# 492206	10.6194	0.999988
VPX25-8, lot# 1a	75 to 500 micron, acid-washed	1.5521	0.999934
VPX25-8, lot# 2a	75 to 500 micron, acid-washed	1.5396	0.999947
VPX25-8, lot# 3a	75 to 500 micron, acid-washed	1.4922	0.999947
10.9 m2/g standard	NIST lot# 492206	10.6879	0.999993
VPX25-8, lot# 1b	<75 micron	2.4267	0.999967
VPX25-8, lot# 2b	<75 micron	2.6284	0.999968
VPX25-8, lot# 3b	<75 micron	2.6070	0.999959
10.9 m2/g standard	NIST lot# 492206	10.5378	0.999978

Copy to:
MS 1320 Hans Papenguth, 6832
MS 1320 George Perkins, 6832

Sandia National Laboratories

Albuquerque, New Mexico 87185-1341

date: August 28, 1996

to: W. G. Perkins, MS-1320 (Org. 6832)

L. H. Brush L. J. Storz

from: L. H. Brush and L. J. Storz, MS-1341 (Org. 6832)

subject: Conversion of K_ds to K_as

This memorandum describes the conversion of matrix distribution coefficients (K_ds) obtained from the empirical sorption study by I. Triay and her group at Los Alamos National Laboratory (LANL) to distribution coefficient expressed on a per-unit-surface-area basis (K_as). As you requested, I have converted only those K_ds obtained by Triay under conditions identical to those in the column transport study by D. A. Lucero and his colleagues at Sandia (synthetic AISinR or ERDA-6 brines in contact with ambient atmospheric CO_2).

To convert these K_ds to K_as, we divided the empirical K_ds, in units of ml/g, obtained under the conditions specified above by 1.5280×10^4 cm^2/g, the mean of Kelly's (1996) three measurements of the specific surface area of the acid-washed, 75-to-500-μm size fraction of VPX-25-8, and rounded to three significant figures. Kelly obtained values of 1.5521, 1.5396, and 1.4922 m^2/g for this sample, which Triay used for the six-week sorption experiments that yielded most of the results used to establish ranges and probability distributions of matrix K_ds for the performance-assessment calculations to support the Waste Isolation Pilot Plant Compliance Certification Application (see Brush, 1996). Table 1 shows the ranges of K_as we obtained for each element and brine type.

REFERENCES

Brush, L.H., and L.J. Storz. 1996. "Revised Ranges and Probability Distributions of K_ds for Dissolved Pu, Am, U, Th, and Np in the Culebra for the PA Calculations to Support the CCA." Unpublished memorandum to M. S. Tierney, July 24, 1996. Albuquerque, NM: Sandia National Laboratories.

Kelly, J.W. 1996. "Surface Area Analysis Results." Unpublished memorandum to L. H. Brush, August 22, 1996. Albuquerque, NM: Sandia National Laboratories.

Table 1. Ranges of Matrix K_as (ml/cm^2) for Pu(V), Am(III), U(VI), Th(IV), and Np(V) and Dolomite-Rich Culebra Rock. Converted using K_ds obtained from LANL six-week sorption runs with VPX-25-8 and ambient atmospheric CO_2 (see Brush, 1996) and mean of three specific surface area measurements by Kelly (1996) (see text).

Brine	Pu(V)	Am(III)	U(VI)	Th(IV)	Np(V)
AISinR	0.0141 to 0.126	NA	0.000164 to 0.000471	NA	0.000327 to 0.0104
ERDA-6	0.00812 to 0.0253	NA	0.000209 to 0.000360	0.0475 to 0.825	0.00175 to 0.00262

NA: not available.

Distribution:

MS 1320 E. J. Nowak (Org. 6831)
MS 1320 W. G. Perkins (Org. 6832)
MS 1320 R. Holt (Org. 6832)
MS 1320 J. W. Kelly (Org. 6832)
MS 1320 H. W. Papenguth (Org. 6832)
MS 1320 M. D. Siegel (Org. 6832)
MS 1324 A. R. Lappin (Org. 6115)
MS 1324 L. C. Meigs (Org. 6115)
MS 1335 M. S. Y. Chu (Org. 6801)
MS 1341 J. T. Holmes (Org. 6832)
MS 1341 L. H. Brush (Org. 6832)
MS 1341 L. J.. Storz (Org. 6832)
MS 1330 SWCF-A:1.1.10.3.1:TD:QA:non-Salado adsorption studies (2)

APPENDIX D
Memorandum on Fracture Orientations

Appendix D errata

Page	Reference	Correction
D-8	Mancock and Engelder, 1988	Mancock and Engelder, 1989

TECH REPS, INC.
5000 Marble Avenue NE
Albuquerque, New Mexico 87110-6390
telephone 505 266 5678, fax 505 260 1163

April 24, 1992

to: Distribution

from: Peter Swift
Tech Reps, Inc./SNL Division 6342

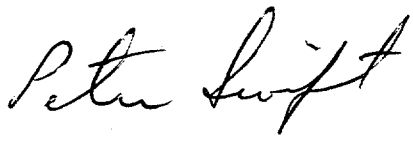

subject: Fracture Orientations in Outcrops of the Rustler Formation and Dewey Lake Red Beds, WIPP Area

Distribution

W. D. Weart, 6303
D. R. Anderson, 6342
B. M. Butcher, 6342
M. G. Marietta, 6342
D. P. Gallegos, 6342
M. S. Tierney, 6342
R. P. Rechard, 6342
E. D. Gorham, 6119
R. L. Beauheim, 6119
T. F. Corbet, 6119
P. B. Davies, 6119
F. Gelbard, 6119
C. F. Novak, 6119
H. Papenguth, 6119
D. J. Borns, 6116
C. L. Stein, 6118
SWCF/HYD

R. Becker, DOE-WPSO
R. Holt, IT/Albuquerque
K. Brinster, SAIC
W. Beyeler, SAIC
D. Rudeen, NMERI
B. Baker, Technadyne
M. LaVenue, INTERA
J. Pickens, INTERA
G. de Marsily, U. Paris
P. Roache, Ecodynamics
P. Knupp, Ecodynamics
T. Zimmerman, GRAM
J. Chapman, Tech Reps, Inc.

INTRODUCTION AND SUMMARY

To the best of my knowledge, the only previous work on fracture orientations in WIPP-area outcrops was done by C. L. Stein and W. H. Casey in 1986. I was unaware of their work when I made my field observations, and the interpretations presented here are based only on my data. Their observations are similar to my own, and I have attached their memo as an appendix for comparison. Neither their work nor mine constitute a definitive study of the subject, although for some applications, data may be adequate and essentially complete. If additional data are needed, they can be collected with relatively little effort by myself or others.

Results of the outcrop study clearly demonstrate that the northeast-southwest trend of Nash Draw coincides with a preferred orientation of fracturing in the units examined. This observation strongly supports a speculative suggestion made by Brinster (1991, Chapter 7) that regional structures control the morphology of Nash Draw. A second preferred orientation approximately perpendicular to the first (i.e., northwest-southeast) is also present in both topographic features and outcrop fractures.

Results of the outcrop study do not offer conclusive information about possible Rustler Formation fracture orientations in the subsurface at the WIPP. The regional scale over which orientations are consistent, however, suggests that similar preferred orientations should be expected at the site, and I conclude that, where fractures are present in the Rustler Formation in the subsurface near the WIPP, they are likely to have orientations similar to those observed in outcrops. I do not offer speculation about the location of subsurface fractures, their density or lengths, or their past and present apertures. My conclusions are consistent with (but not dependent on) my belief that the preferred orientations of fractures reflect past regional stress fields, whereas their specific geometries reflect local stress fields and solution processes.

TERMINOLOGY

The definitions offered here are my own. They are based on standard usage in structural geology (e.g., Hobbs et al., 1976; Bates and Jackson, 1980; Davis, 1984; Hancock, 1985; Pollard and Aydin, 1988; Narr and Suppe, 1991), but they are not taken from a specific reference. More complicated definitions are possible (e.g., Engelder, 1985; Pollard and Aydin, 1988) but they add little to this discussion.

Fracture: any break in a rock

Joint: an approximately planar fracture showing little or no displacement at the scale of observation

Joint set: a population of joints with subparallel orientations

High-Angle Joint: a joint with a dip greater than or equal to 75° from the horizontal

My emphasis is on the orientations of high-angle joints. Apparently random non-planar fractures are visible at various scales in outcrops, and subhorizontal joints are common in some outcrops. Neither of these types of fractures provide useful information about preferred orientations. Joints with intermediate dips are present but relatively rare; I have recorded their orientations but have chosen not to display them with the predominant high-angle trends.

FIELD OBSERVATIONS

Methodology

I selected six outcrops for study based on availability, accessibility, and geographic distribution (Figure 1). I did not examine all outcrops of the Rustler Formation and the Dewey Lake Red Beds in the WIPP area, nor did I examine in detail all portions of the outcrops from which I report data. For example, the outcrop at Culebra Bluff (Location 1 of Figure 1) extends for more than one km along the Pecos River. Orientations reported from that location come from four separate segments of the outcrop, each approximately 20 m in length (Figure 2). At Culebra Bluff, as at other locations, I selected portions of the outcrop to examine in detail based on representativeness and accessibility. In particular, I avoided locations where bedding is no longer subhorizontal, indicating deformation and probable rotation of the original orientations of the fractures. With the exception of Location 4, all measurements were collected from outcrops in which the dip of bedding was 5° or less. Dips of bedding in the Magenta Dolomite at Location 4 ranged locally up to 18°.

Orientations were measured using a Brunton compass/clinometer. My selection of individual joints to measure was subjective: at some locations there were few enough joints to measure all orientations, and at others I chose representative subareas to measure in detail. More rigorous methods are available to reduce observational bias in joint-orientation studies (e.g., the circle-inventory method as described by Davis, 1984) and could be used if applications of the data warrant the work.

At some locations exposures were not adequate to determine the dip of the joints, and the recorded azimuths are the trend of the trace of the joint exposed in a subhorizontal plane. As a result, some displayed azimuths may not be correctly attributed to high-angle joints. More rigorous field methods could eliminate this problem, but would also greatly reduce the area of outcrop available for study. All data from Location 3 were collected from two-dimensional exposures, as was much of the data from Location 2. Only at Location 1 (Culebra Bluff) were all measurements recorded from three-dimensional exposures.

Results

Results of the study are presented in Table 1 and Figures 3 through 8. Joint orientations in Table 1 are presented as strikes and dips for Location 1, where exposures permitted measuring both. For the other five locations, I recorded only the strikes of joints, although I confirmed whenever possible

in the field that dips were steep. Strike orientations are summarized in rose diagrams in Figures 3 through 8, with individual azimuth values grouped into 5° intervals and each radial increment indicating a discrete measurement. I have omitted the west half of the rose diagrams for simplicity.

REGIONAL OBSERVATIONS

Trends visible in Figures 3 through 8 can also be seen in map-scale physiographic features of the region. The long axis of Nash Draw, which I estimate by eye to be 39° east of north, is subparallel to the trend of the best-defined joint set. The northwest and southeast limbs of Nash Draw are approximately orthogonal to this trend (130° by eye), and are subparallel to a second joint set. Other features visible in Figure 1 with these orientations include orthogonal reaches of the Pecos River southwest of Nash Draw, the southern portion of Clayton Basin, and the alignment of playas northeast of Nash Draw.

The mid-Tertiary igneous dike intersected in two potash mines near Nash Draw and also mapped from borehole data and aeromagnetic surveys trends 50° east of north (Powers et al., 1978), approximately 10° off from the main axis of the Draw. Powers et al. (1978, section 3.5.1) note that the trend of the dike "generally coincides with the orientation of several tectonic lineaments in the area and also parallels ... joints ... near Carlsbad Caverns." Jagnow (1979) provides extensive data on joint orientations in the subsurface from caves in the Guadalupe Mountains, including Carlsbad Caverns. Joint sets are well-developed in the caves, and generally trend parallel and perpendicular to the mountain front. Over the entire length he examined, from the southern end of the range in Texas to Carlsbad Caverns, preferred orientations shift systematically from north-northeast toward east-northeast. In portions of the range, therefore, orientations of joints in the Guadalupe Mountains parallel both Nash Draw and the dike. In other portions they do not.

COMMENTS ON FRACTURING OBSERVED IN CULEBRA CORE

I have not examined core samples directly, and I have no data about fracture orientations from any core. I have examined all available photographs of the horizontal core from the Air Intake Shaft, and some photographs of vertical core from wells. My core observations are limited by problems of scale, preservation, and availability of samples, and should be regarded as anecdotal only.

Most fractures seen in core photographs appear to be random in orientation, and of relatively small extent (centimeters in scale). These fractures typically connect vugs, and are most abundant in regions (stratigraphic layers?) where vuggy porosity appears to be greatest. They are unlike the joints observed in outcrop, which do not appear to correlate in density to vugginess, and which cut across stratigraphic features on a vertical scale not seen in core. Larger, roughly planar, fractures are visible in many photographs of the horizontal core, and in several cases occur in approximately orthogonal pairs.

INTERPRETATIONS

Regional Extent of the Joint System

The six outcrop locations enclose less than 200 km^2. Based on the regional physiographic features noted in the previous section, I believe that joint orientations are consistent over a much larger area, extending at least 60 km from Laguna Tonto in the northeast (not shown in Figure 1) to the town of Malaga in the southwest, and as much as 25 km from Clayton Basin in the northwest to the vicinity of H-7 in the southeast limb of Nash Draw. No field or map observations define the limits of the joint system, and its actual extent may be considerably larger.

I believe that jointing in the Guadalupe Mountains and the orientation of the igneous dike west of the WIPP both share a common origin with the Nash Draw joint system. Available evidence does not conclusively support this observation, and I do not base interpretations of jointing near the WIPP on it.

Age of the High-Angle Joints

The older limit for the age of the joints is constrained by the age of the youngest unit affected, which I believe to be the Late Permian Dewey Lake Red Beds. I did not examine outcrops of the Triassic Dockum Group. The younger limit for the age of the joints is constrained by the age of the oldest unit not affected, which I believe to be the Pleistocene? Gatuña Formation. This limits the time of joint formation to a window of approximately 245 million years.

Evidence supporting these age bounds can be found at Location 6, where the Dewey Lake Red Beds are jointed (and the overlying post-Gatuña caliche is not), and at Location 1 (Culebra Bluff), where a deposit of undated Gatuña sandstone can be seen to partially fill and overlie a structural depression in the Culebra Dolomite. As have others (e.g., R. Holt, personal communication), I interpret much of the deformation at Culebra Bluff to be the result of dissolution of evaporites and collapse of the overlying dolomite. At least some of this deformation immediately preceded deposition of the flat-lying Gatuña sandstones that fill depressions, and therefore occurred in the latest Cenozoic or Pleistocene. Joints in and near structural depressions at Culebra Bluff have rotated from the vertical and remain subperpendicular to rotated bedding, indicating that they had formed prior to deformation of the section. The same relationship between bedding and jointing can be observed in the deformed Rustler section at "L-R Hill" in sections 24 and 25, T23S,R29E, southwest of Location 3.

Not all joints in the units examined need be of the same age. Individual joints within a single set are likely to be of the same age, however, and I believe that the northeast and southeast trending sets formed simultaneously. Other sets are present in the region and visible in Figures 3 through 8. In particular, east-west and north-south sets are well-developed at locations 2 and 3, and can be found at all locations. My field observations did not

reveal a consistent cross-cutting relationship between these joints and those of the northeast/southeast pair that could be used to determine their relative age. Additional field work could possibly resolve this point.

Origin of the High-Angle Joints

As is the case with most regional joint systems, the origin of these joints is unknown. In general, joints form in response to changes in regional stress (Engelder, 1985), but because joints show little or no displacement, it is difficult to interpret regional strain and the causative stresses. Suggested mechanisms for the formation of systematic joints include abnormal fluid pore pressures, compressional tectonic stresses, and the release of either lithostatic or tectonic stresses during erosional unloading (Engelder, 1985).

The origin of the joint system is of interest because the depth to which joints can be expected is in part a function of the mechanism by which they formed. For example, unloading joints may form at relatively shallow depths (between 1 km and 500 m for examples from the Appalachian Plateau, Hancock and Engelder, 1988); whereas joints formed by abnormal pore pressures can be expected at depths of 5 km or greater (Engelder, 1985).

My outcrop observations do not support a unique interpretation of the origin of the joints. My speculative belief is that they formed during Cenozoic uplift, tilting, and erosion of the Delaware Basin (Powers et al., 1978). Regional unloading provided the primary change in the stress field that initiated jointing, with joint orientations controlled by horizontal tectonic stresses. Horizontal stresses were probably created by plate-scale processes, including both intraplate extension along the Rio Grande Rift and the overall westward movement of the North American plate. Within the Delaware Basin, orientation of the stress field may have been strongly affected by pre-existing regional features, including lithologies of the basin fill and the crustal structures that define the shape of the basin. I suspect that the nature of the Cenozoic stress field in the Delaware Basin will remain uncertain, and I doubt that it will be possible to link joint orientations directly to past stress orientations.

Beauheim and Holt (1990) and others have suggested that the westward increase in transmissivity of the Culebra at the WIPP in part reflects an increase in fracturing caused by the decrease in overburden thickness. I agree that regional unloading probably played an important role in joint formation and that local stresses may in part control the degree to which joints in the subsurface are open at present. I do not believe, however, that the increase in overburden east of Nash Draw is of sufficient magnitude to provide the primary basis for an interpretation that fracture orientations or densities should be significantly different at the WIPP than in the Draw. Only about half of the approximately 200 m increase in overburden thickness between Nash Draw and the WIPP is the result of stratigraphic dip. The remainder reflects modern topography, which is controlled by erosion and dissolution. The consistency of joint orientations between locations with apparently different erosional and dissolutional histories, such as Culebra Bluff (Location 1), Location 6, and Location 3, suggests that topography has had little effect on

joint orientation. Furthermore, much of the present topography post-dates deposition of the Gatuña Formation and therefore post-dates joint formation.

Based in part on the Narr and Currie (1982) model for changes in stress during burial and erosion (which requires the assumption that rocks acquire their present material properties at maximum burial), Engelder (1985) suggests that unloading joints form in a sedimentary basin when approximately 50 percent of the original maximum load has been removed by erosion. The total thickness of rocks which once overlaid the Culebra at the WIPP is unknown (and will remain so) but can be inferred to have included at a minimum the 200 m of present overburden and the approximately 375 m of Triassic rocks preserved to the east of the site, as well as a Cretaceous section which may have been up to 300 m thick (R. Holt, personal communication). A crude application of Engelder's (1985) approach suggests that unloading joints could be expected in the Culebra above depths ranging anywhere from 290 to 440 m below the pre-Gatuña land surface. Uncertainty in this estimate is large, but depths are great enough that overburden thickness alone should not be used to argue against fracturing of the Culebra at the WIPP. The low end of the range is a minimum value based on the unrealistic assumption of no Cretaceous sedimentation, and conceptual models for other mechanisms of joint formation suggest greater depths (Engelder, 1985).

Non-systematic joints (the "noise" visible in the rose diagram for Location 3, for example) are probably not related genetically to the major sets, and may have formed later in response to local changes in the stress field related to erosion and dissolution. If so, randomly-oriented joints may be less abundant in subsurface east of the area of outcrop, where stresses are presumably more uniform. Outcrop observations, however, suggest an increase in the abundance of non-systematic joints eastward, and Culebra Bluff, which may have undergone the most deformation related to dissolution, shows the least variability in joint orientation. Additional field work may help resolve questions about the origin and distribution of non-systematic joints.

Hydrologic Implications for the WIPP

I believe that the evidence presented here demonstrates that the orientation of Nash Draw is controlled by the orientation of regional joint sets, which apparently controlled preferential dissolution and erosion. My field work does not explain the location of Nash Draw: joint sets are best-developed at Culebra Bluff west of the Draw, and regional map observations suggest that the joint sets are present over an area much larger than the Draw.

Outcrop observations provide no direct information about fracturing in the subsurface at and near the WIPP. I believe, however, based on both outcrop data and regional map observations, that the same joint sets are present throughout the area of interest for hydrologic modeling. The major joint sets formed before modern topography developed, and therefore probably do not correlate well with the present distribution of overburden above the Rustler Formation.

I offer essentially no conclusions about the hydrologic significance of preferred joint orientations in the subsurface at and near the WIPP. Joints in the subsurface may remain closed until local stresses allow opening, and

joints that have opened may be further opened by dissolution or sealed by precipitation. My outcrop observations provide no information relevant to the subsurface about spatial variability in the density of joints or the length of individual joint surfaces. Map-scale examination of the morphology of Nash Draw suggests that west of the WIPP jointing affects groundwater flow on a several-kilometer scale.

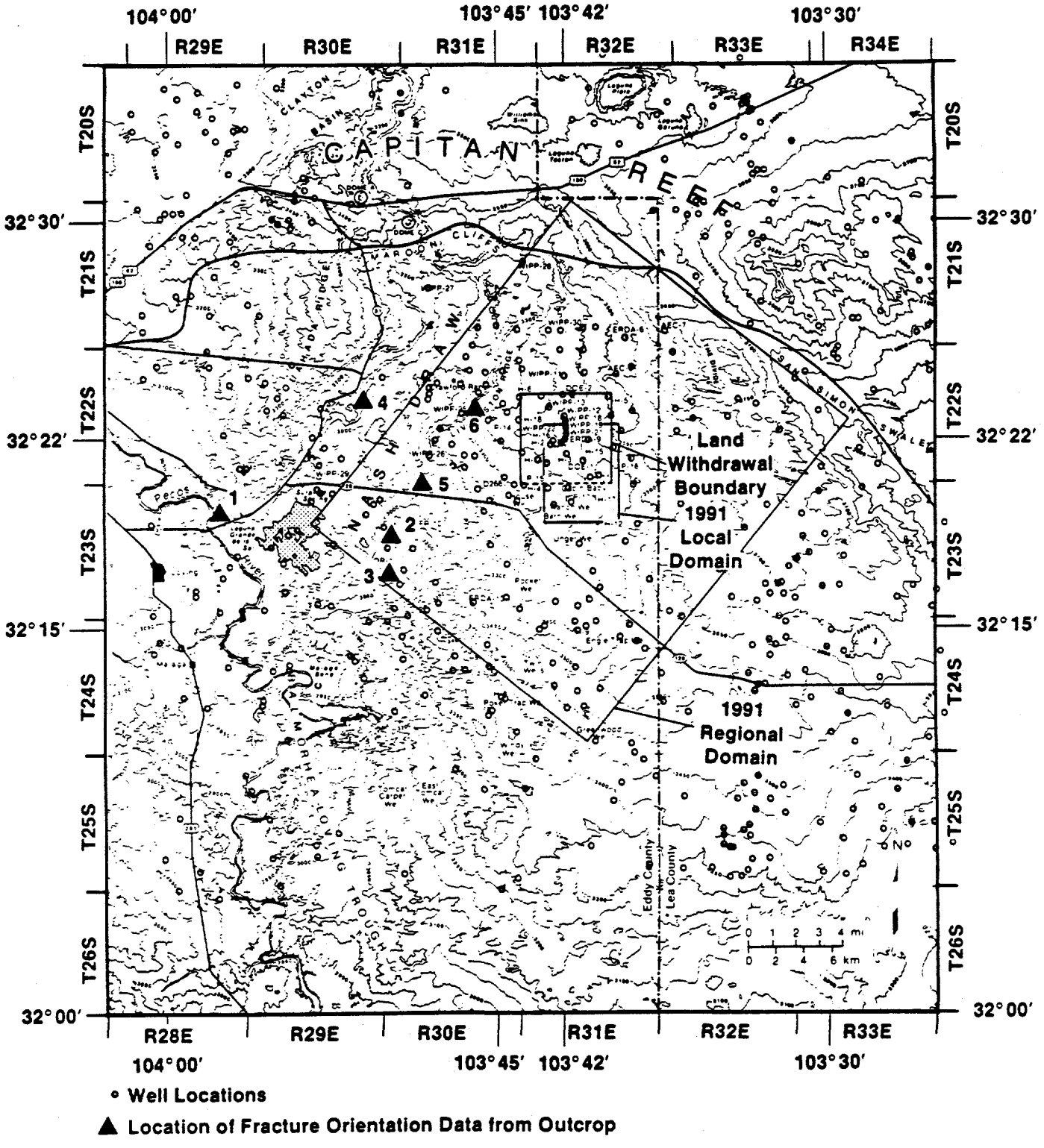

Figure 1. Location of Joint Orientation Measurements. Base map from WIPP PA Division (1991).

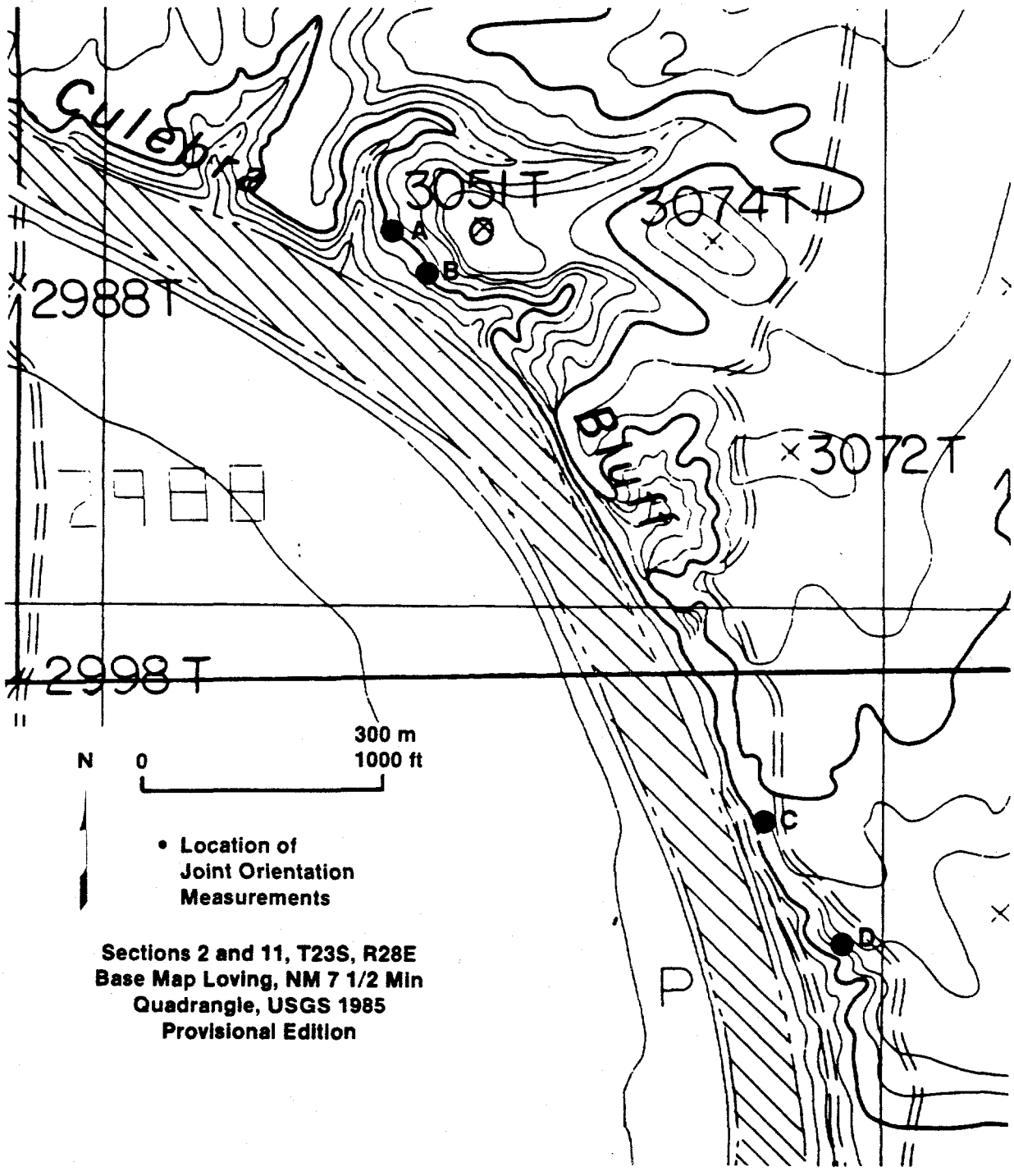

Figure 2. Location of Joint Measurement Stations at Culebra Bluff (sections 2 and 11, T23S,R28W).

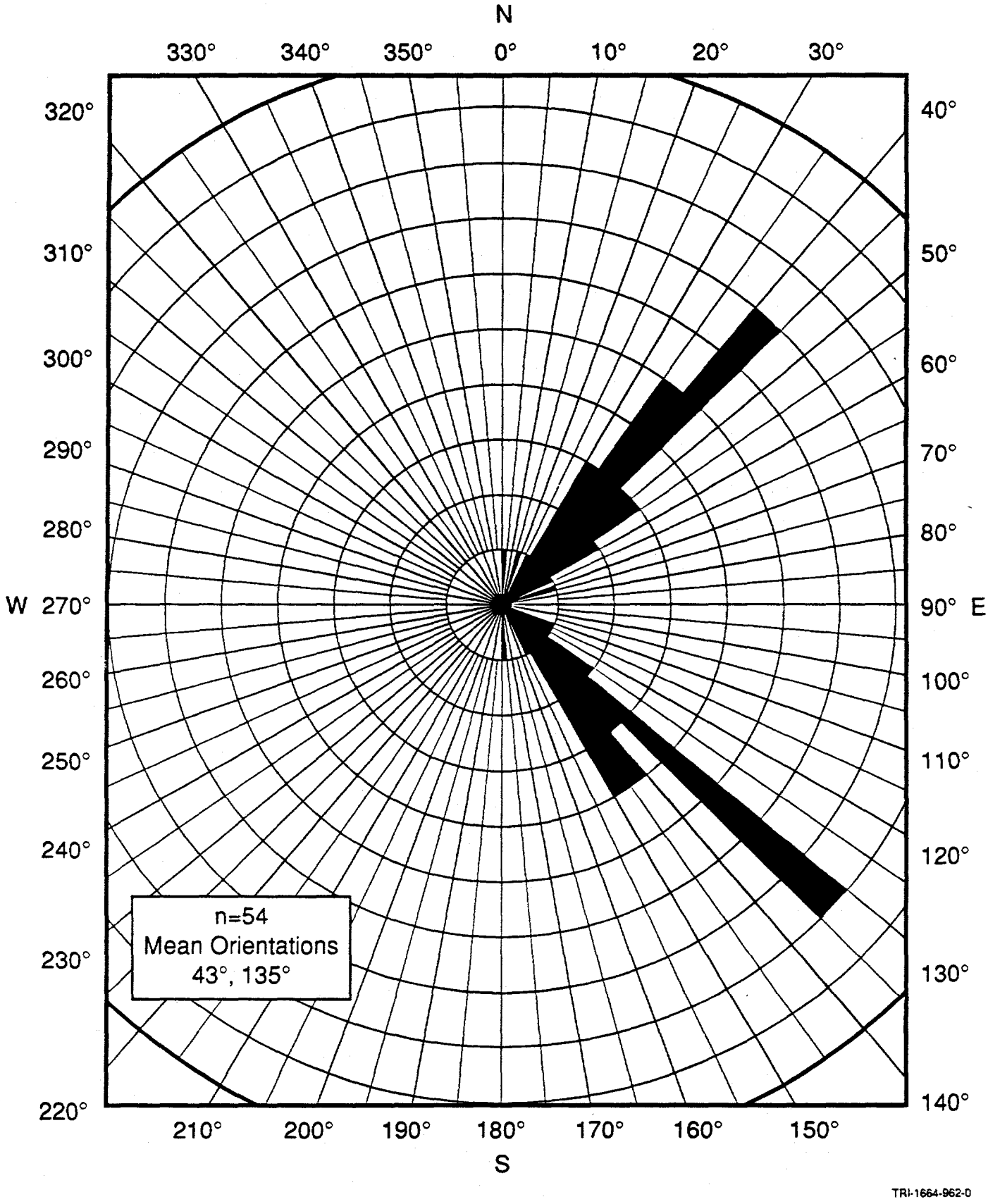

Figure 3. Strike of High-Angle Joints at Location 1 (Culebra Dolomite at Culebra Bluff, sections 2 and 11, T23S,R28E).

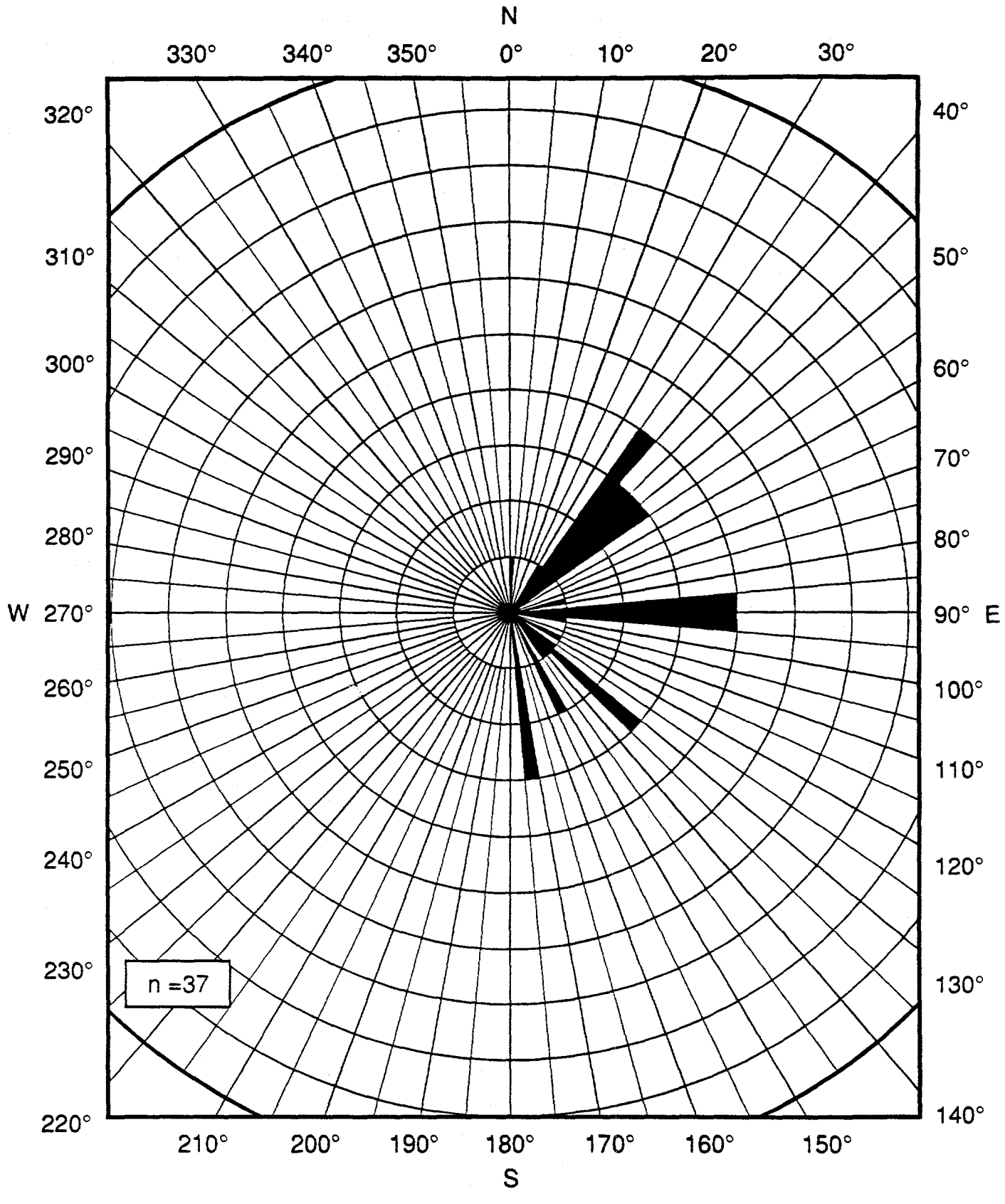

Figure 4. Strike of High-Angle Joints at Location 2 (Culebra Dolomite in and near roadside quarry, section 18, T23S,R30E).

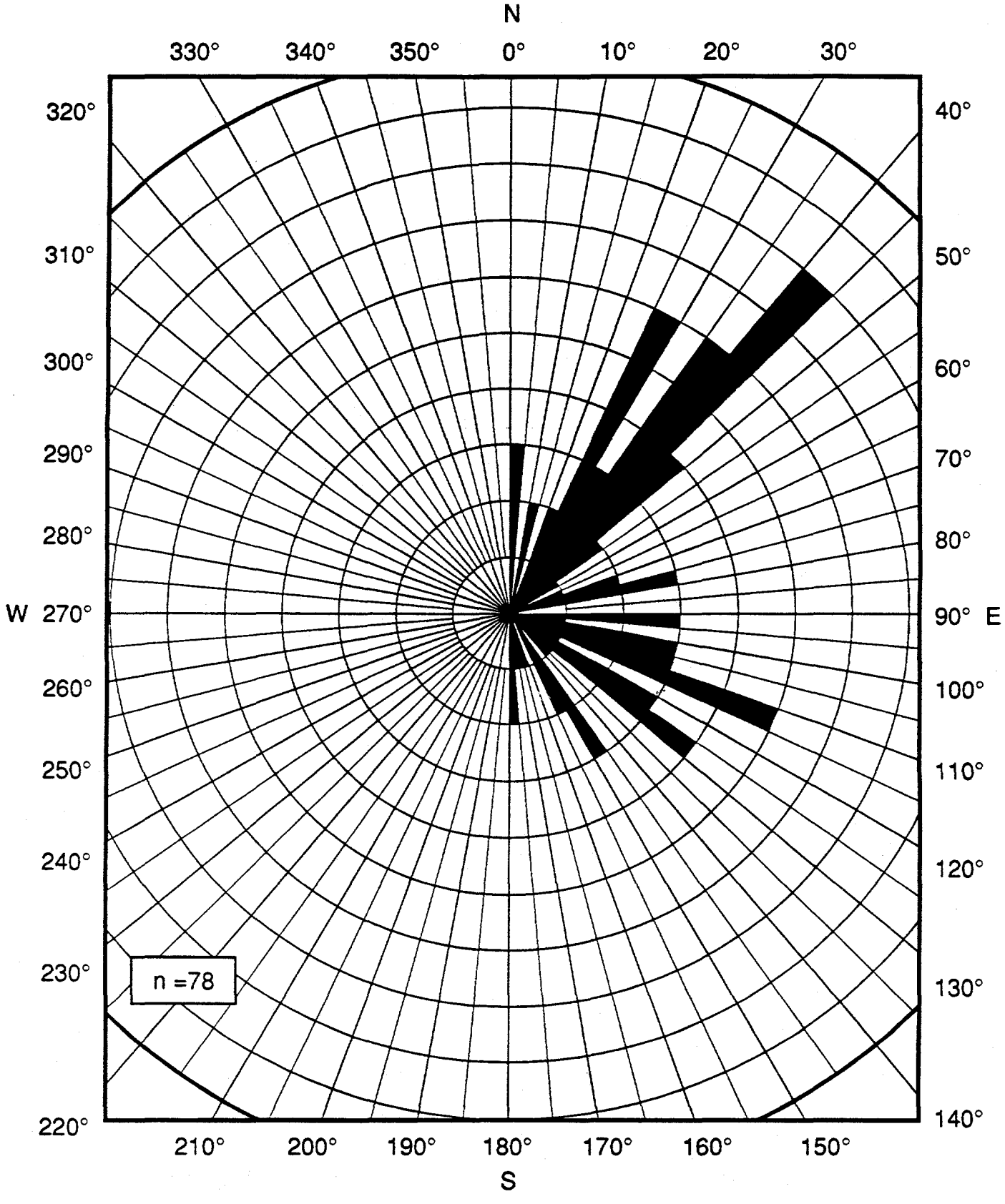

Figure 5. Strike of High-Angle Joints at Location 3 (Culebra Dolomite northeast of "L-R Hill," section 19, T23S,R30E and section 24, T23S,R29E).

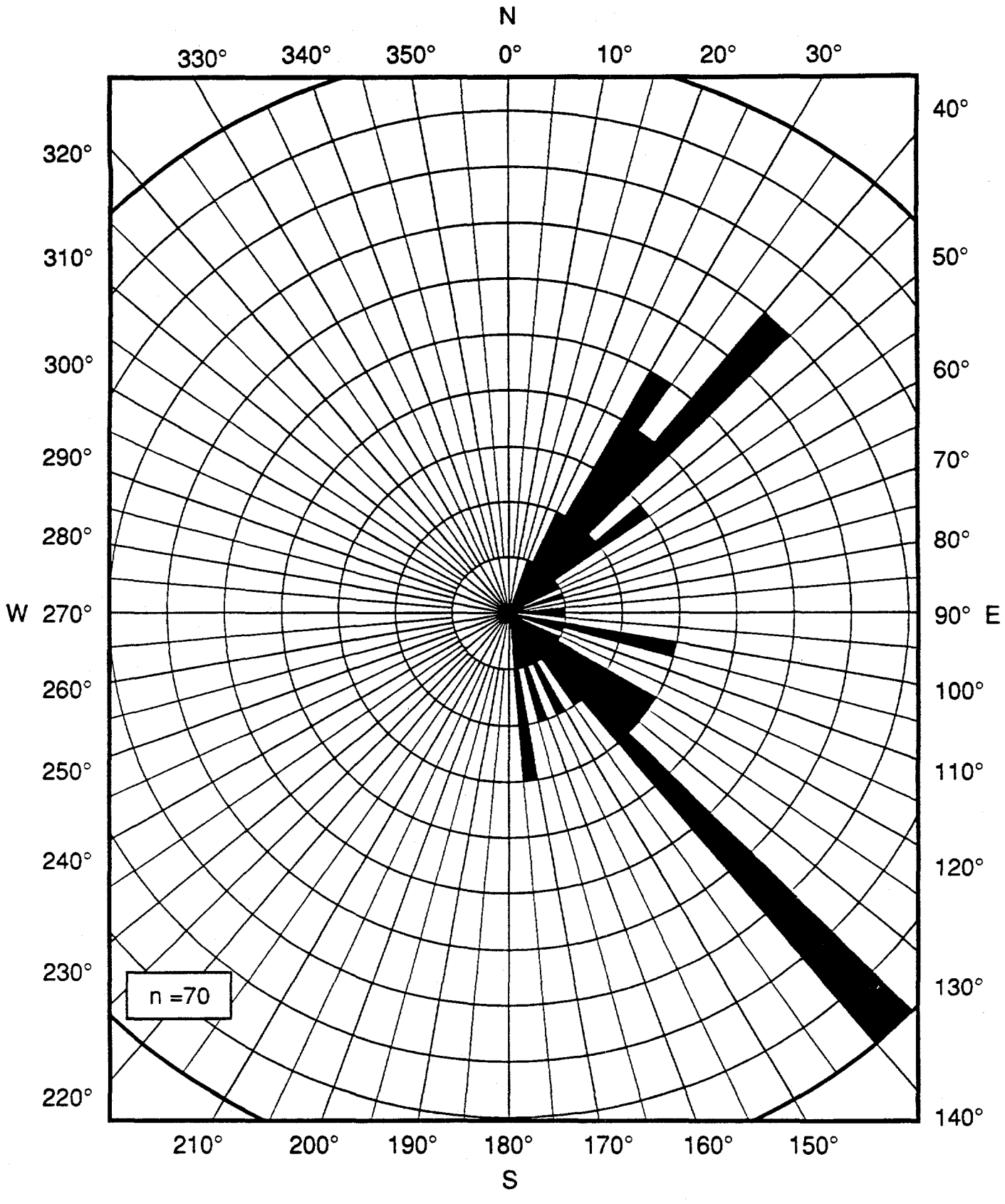

Figure 6. Strike of High-Angle Joints at Location 4 (Magenta Dolomite and Forty-Niner Members of the Rustler Formation in sections 13 and 14, T22S,R29E).

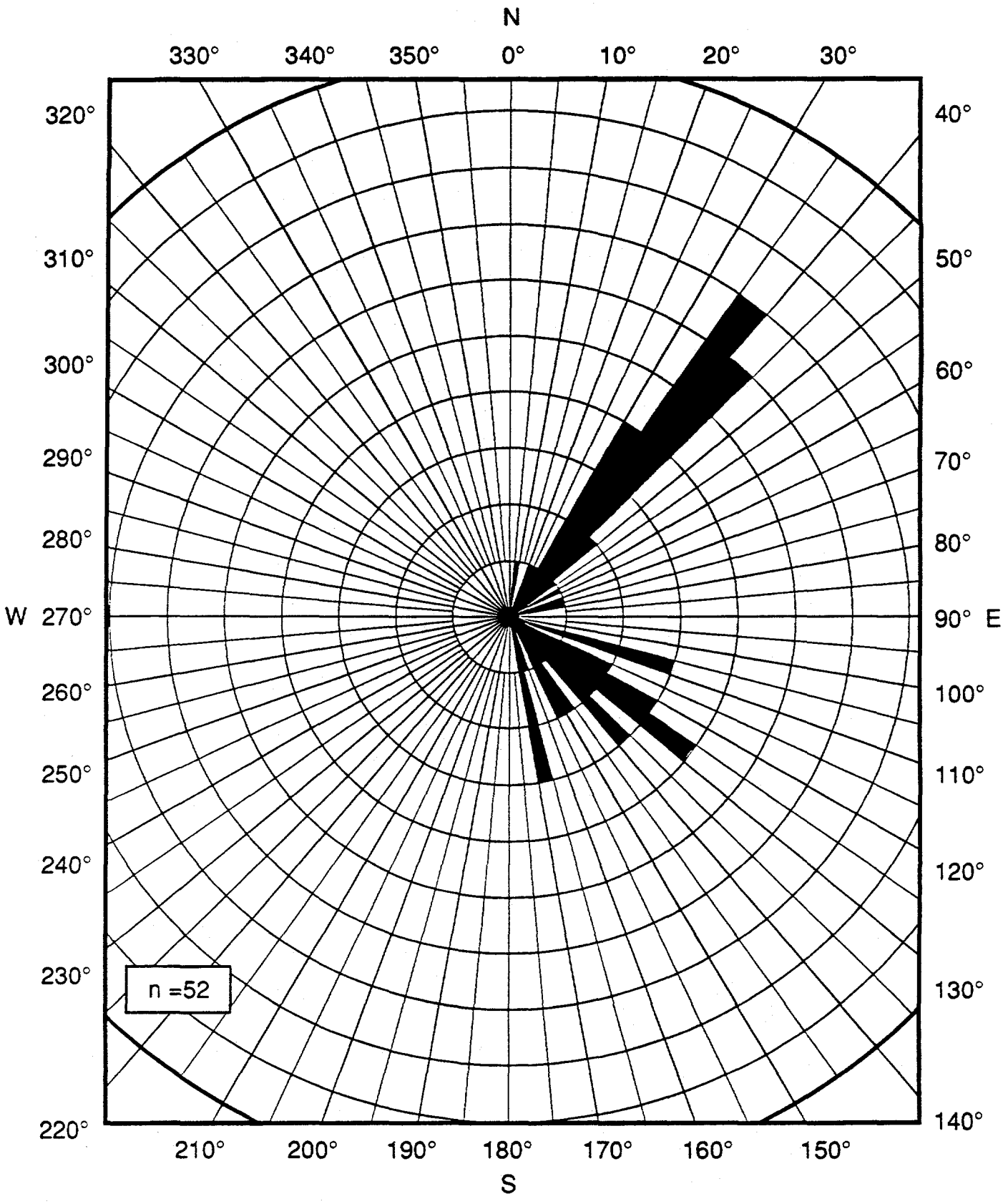

Figure 7. Strike of High-Angle Joints at Location 5 (Magenta Dolomite in railroad cut, section 18, T23S,R30E).

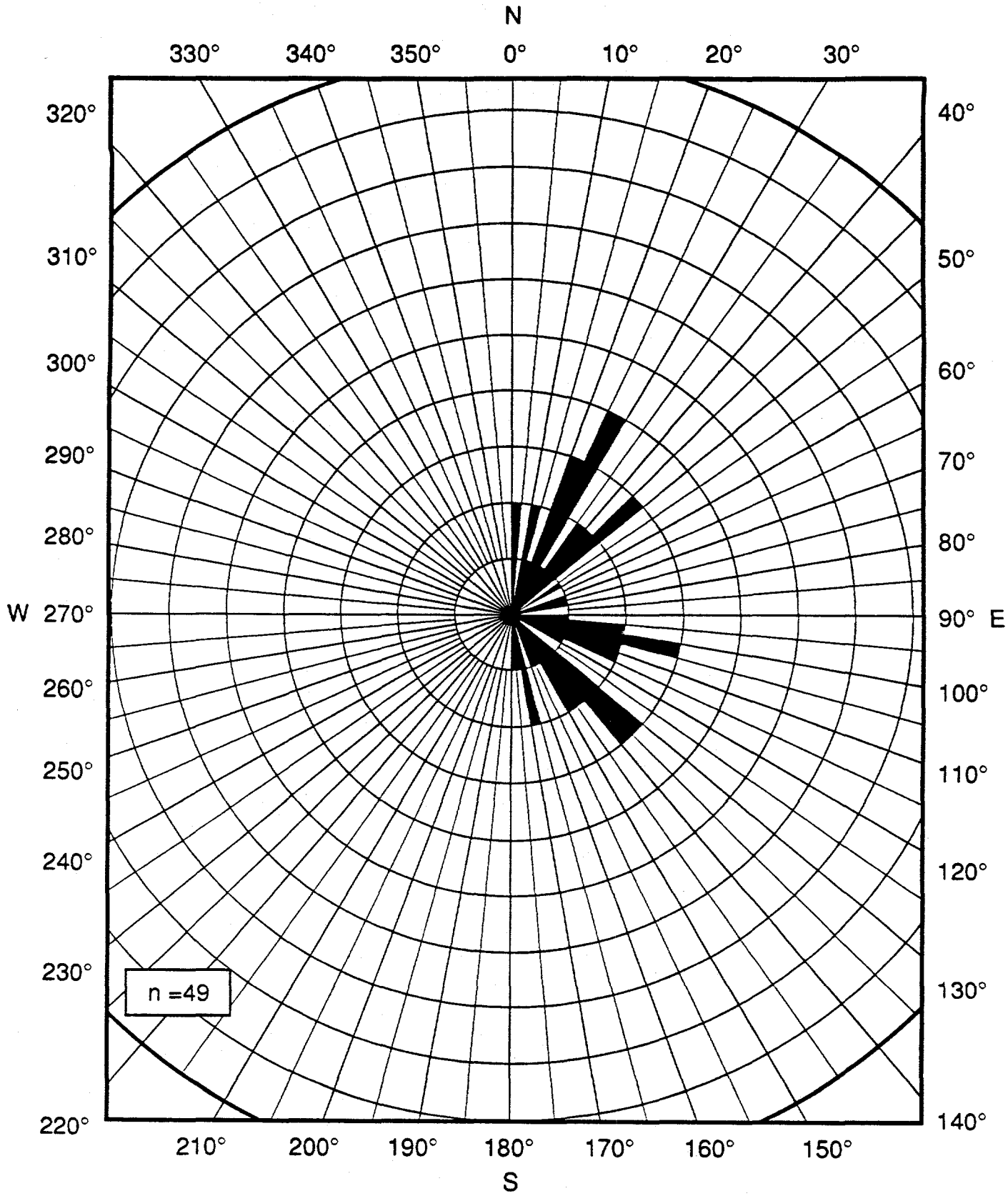

Figure 8. Strike of High-Angle Joints at Location 6 (Dewey Lake Red Beds in section 15, T22S,R30E, northeast of WIPP-25).

Table 1. Joint Orientations Recorded from Outcrops of the Rustler Formation and the Dewey Lake Red Beds. Locations are shown on Figures 1 and 2. Strike orientations are given in degrees clockwise from true north. Dip orientations, where recorded, were measured perpendicular to strike and are given in degrees below horizontal with the principal compass direction noted. The order in which data is presented reflects the organization of my field notes: in some cases I have attempted to group data into sets, but in general the organization is not significant.

Location 1. Culebra Bluff, sections 2 and 11, T 23S,R28E.

Station A. Measurements recorded February 25, 1992

strike	dip	strike	dip
42	88S	130	82W
42	85N	129	88W
54	86S	130	90
47	78N	130	84E

Station B. Measurements recorded February 25, 1992

strike	dip	strike	dip
34	84S	130	85W
40	86S	138	85E
45	85S	144	80W
33	85S	140	85W
35	88S	133	75W
52	80S	130	85W
15	90	150	90
		145	90

Station C. Measurements recorded February 26, 1992

strike	dip	strike	dip
38	78N	130	85W
28	74N	140	85W
52	87N	145	82W
42	73N	119	88W
38	90	145	80W
60	89S	135	70W
42	85N	130	55E
35	86N	122	42W
75	80N	120	28W
30	62S		

Station D. Measurements recorded February 26, 1992

strike	dip	strike	dip
55	85S	145	85W
40	85N	110	76W
55	90	130	90
40	90	135	85W
45	90	140	90
38	90	128	90
30	90	120	90
0	90		
175	75E		

Location 2. Culebra Dolomite outcrop in and near roadside quarry, section 18, T23S,R30E.

Strike orientations recorded February 26, 1992

35	130	90	0
35	130	90	175
50	150	85	
45	150		

Strike orientations recorded March 10, 1992

47	138	85	178
42	144	87	176
43	130	88	
50	126	90	
38	119	91	
46		97	
31		77	
38			
52			
44			

Location 3. Culebra Dolomite in section 19, T23S,R30E and section 24, T23S,R29E

Strike orientations recorded March 10, 1992

38	114	78	177
44	105	68	175
20	128	97	4
47	100	72	174
36	105	79	164
42	104	74	168
22	122	94	17
26	149	94	14
49	154	77	4
52	119		
50	145		
34	114		
44	110		
38	108		
28	154		
36	136		
42	124		
36	126		
42	112		
25	114		
26			
28			
38			
41			

Strike orientations recorded March 11, 1992

47	92	146	11
32	101	132	1
31		127	
29		128	
58		124	
43			
41			

Location 4. Outcrops of Magenta Dolomite and Forty-Niner Members of the Rustler Formation in sections 14 and 13, T22S,R29E

Strike orientations recorded February 25, 1992

44	130
34	128

Strike orientations recorded March 11, 1992

32	119	164	100
41	121	162	89
41	142	169	101
32	132	154	78
46	128	174	92
48	136	154	101
38	149	170	
38	139	158	
29	136	174	
32	129		
29	121		
51	109		
49	139		
44	135		
52	134		
61	138		
46	141		
20	136		
44	135		
51	138		
56	130		
48	122		
34			
46			
48			
47			
38			
38			
40			

Location 5. Magenta Dolomite in railroad cut, section 18, T 23S,R30E

Strike orientations measured March 10, 1992

40	105	62	165
38	126	75	165
34	132	72	162
38	136		166
52	138		150
42	144		5
45	105		150
40	146		
39	122		
35	129		
44	130		
32	109		
36	138		
30	128		
26	129		
46	116		
34	121		
22	119		
36	145		
38	122		
44			
42			

Location 6. Dewey Lake Formation, section 15, T22S,R30E (NE of WIPP-25)

Strike orientations measured March 10, 1992

10	100	42	135
172	97	36	135
169	104	46	132
169	90	47	155
4	104	47	146
3	98	42	132
10	109	37	141
	105	28	143
	70	24	150
	5	29	112
		18	110
		20	130
		20	138
		28	116
		55	147
		26	
		31	

REFERENCES

Bates, R. L., and J. A. Jackson, eds. 1980. *Glossary of Geology, Second Edition*. Falls Church, VA: American Geological Institute.

Beauheim, R. L., and R. M. Holt. 1990. "Hydrogeology of the WIPP Site," in *Geological and Hydrological Studies of Evaporites in the Northern Delaware Basin for the Waste Isolation Pilot Plant (WIPP), New Mexico*. Guidebook, Geological Society of America Field Trip Number 14, November 1-4, 1990. Dallas, TX: The Dallas Geological Society.

Brinster, K. F. 1991. *Preliminary Geohydrologic Conceptual MOdel of the Los Medaños Region Near the Waste Isolation Pilot Plant for the Purpose of Performance Assessment*. SAND89-7147. Albuquerque, NM: Sandia National Laboratories.

Davis, G. H. 1984. *Structural Geology of Rocks and Regions*. New York, NY: John Wiley and Sons.

Engelder, T. 1985. "Loading Paths to Joint Propagation During a Tectonic Cycle: An Example From the Appalachian Plateau, U.S.A.," *Journal of Structural Geology* 7: 459-476.

Hancock, P. L. 1985. "Brittle Microtectonics: Principles and Practice," *Journal of Structural Geology* 7: 437-457.

Hancock, P. L., and T. Engelder. 1989. "Neotectonic Joints," *Geological Society of America Bulletin* 101: 1197-1208.

Hobbs, B. E., W. D. Means, and P. F. Williams. 1976. *An Outline of Structural Geology*. New York, NY: John Wiley and Sons.

Jagnow, D. H. 1979. *Cavern Development in the Guadalupe Mountains*. Albuquerque, NM: Adobe Press.

Narr, W., and J. B. Currie. 1982. "Origin of Fracture Porosity—Example from Altamont Field, Utah," *American Association of Petroleum Geologists Bulletin* 66: 1231-1247.

Narr, W., and J. Suppe. 1991. "Joint Spacing in Sedimentary Rocks," *Journal of Structural Geology* 13: 1037-1048.

Pollard, D. D., and A. Aydin. 1988. "Progress in Understanding Jointing Over the Past Century," *Geological Society of America Bulletin* 100: 1181-1204.

Powers, D. W., S. J. Lambert, S.-E. Shaffer, L. R. Hill, and W. D. Weart, eds. 1978. *Geological Characterization Report, Waste Isolation Pilot Plant (WIPP) Site, Southeastern New Mexico. Volume 1*. SAND78-1596. Albuquerque, NM: Sandia National Laboratories.

WIPP PA (Performance Assessment) Division. 1991. *Preliminary Comparison With 40 CFR Part 191, Subpart B for the Waste Isolation Pilot Plant, December*

1991. Volume 3: Reference Data. SAND91-0893/3. Albuquerque, NM: Sandia National Laboratories.

Sandia National Laboratories

Albuquerque, New Mexico 87185

date: 5 June 1986

to: Distribution

from: C. L. Stein, 6331 and W. H. Casey, 1543

subject: Fracture mapping in Culebra outcrops

As part of the preparation for the sorbing tracer test, we performed some very preliminary mapping of fractures in the Culebra Dolomite. We examined several outcrops where the Culebra is exposed along the Pecos River near Carlsbad. Three areas where the unit appears to be exposed in its entirety were selected for more detailed mapping.

Although we took both dip and strike measurements, most of the fractures are vertical or near-vertical. Therefore we used rose diagrams, as shown below, to illustrate fracture direction. Major trends are NW-SE and NE-SW. In addition, we observed that most of the outcrops have very pronounced bedding plane fractures that occur on a scale of approximately 2" to 10" apart. The individual dolomite beds themselves are fractured on scales of less than one inch up to several feet; the smaller fractures are not continuous vertically, i.e., these do not cross the bedding plane fractures. There is no correlation between fracture spacings from one sedimentary bed to the next.

Also, not all outcrops exhibit the same abundance or distributuion of fracturing. We observed two outcrops approximately 300' apart, one of which is highly fractured as described above. The other is much more intact and contains primarily the large vertical fractures that cut across the bedding planes. We photographed these outcrops in some detail in order to produce a photomosaic; we will notify anyone expressing an interest when the pictures are ready.

We realize that any correlation between the appearance of the Culebra Dolomite in outcrops and its subsurface character is tenuous at best. Nevertheless, it seems that any possible relation between fracture spacing, aperture, and direction (as seen in outcrop) and hydrologic behavior must be examined. We welcome any suggestions and/or directions for future work on this topic.

CLS/BC

OUTCROP I

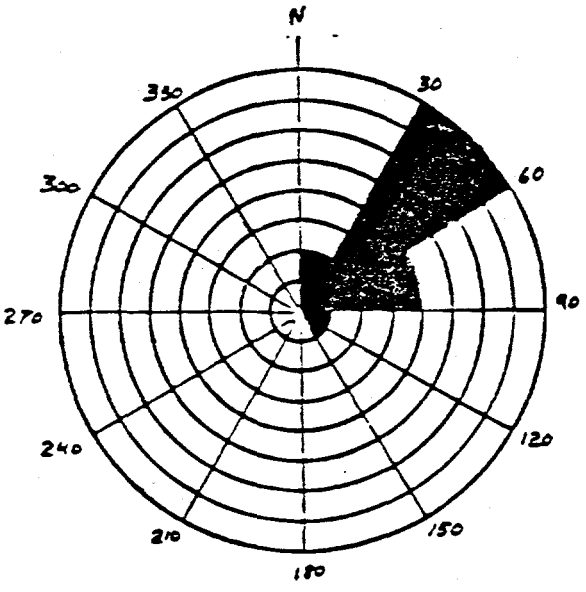

OUTCROP II

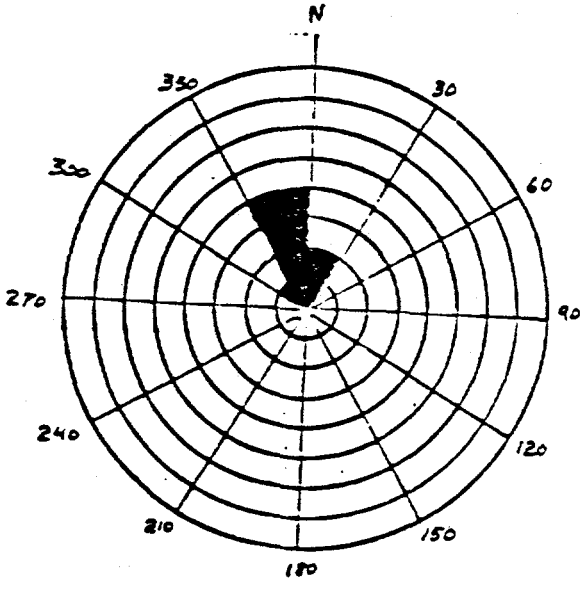

OUTCROP III

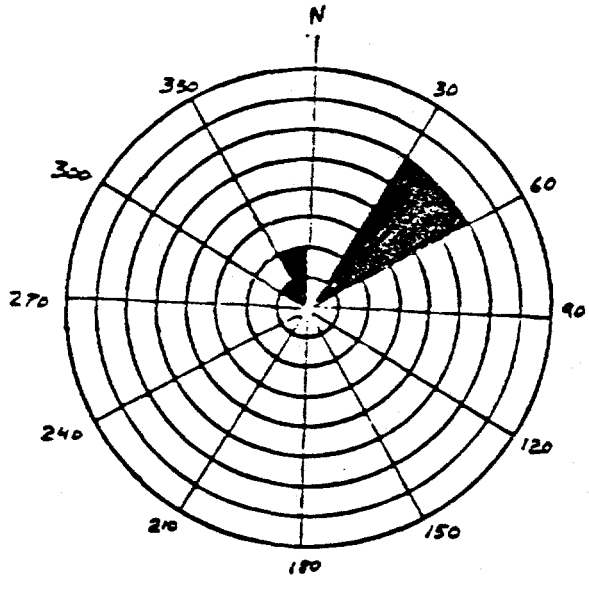

APPENDIX E
Damkohler Number Calculations and Parameters for Cores C, D, and E

Tables E-1 and E-2 provide the parameters necessary for calculating Damkohler numbers for cores C, D, and E. Porosity estimates are based on the core surface maps (Figures 4-3, 4-4, and 4-5). As in Section 2.4, porosity estimates are made by scaling the mean porosity of material present (Table 2-1 and Appendix A) by the fraction of the core containing that material.

Table E-1. Damkohler Number Calculations for Cores C, D, and E

Core C									
Porosity Type	Half-Block Size l_n (m)	Geometry	Geometric Factor B_n	Diffusive Porosity ϕ_n	Specific Surface Area $S_{A,n}$ (m^2/g)	Bulk Density $\rho_{b,n}$ (g/m^2)	Retardation Factor R_n	Formation Factor F_n	$D_{a,n}$ (m^2/s)
Refer to:				Table 4-1	Sect. 2.1	Eq. 2-1	Eq. 3-2	Table 2-1	Eq. 3-7
IC	0.02	layered	2.5	0.10	1	2530000	17	111	2.7E-12
IC,V	0.05	layered	2.5	0.002	1	2820000	1229	104	2.9E-12
Core D									
Porosity Type	Half-Block Size l_n (m)	Geometry	Geometric Factor B_n	Diffusive Porosity ϕ_n	Specific Surface Area $S_{A,n}$ (m^2/g)	Bulk Density $\rho_{b,n}$ (g/m^2)	Retardation Factor R_n	Formation Factor F_n	$D_{a,n}$ (m^2/s)
Refer to:				Table 4-1	Sect. 2.1	Eq. 2-1	Eq. 3-2	Table 2-1	Eq. 3-7
IC	0.02	layered	2.5	0.09	1	2560000	19.1	111	2.7E-12
IC,V	0.02	layered	2.5	0.002	1	2820000	1229	104	2.9E-12
Core E									
Porosity Type	Half-Block Size l_n (m)	Geometry	Geometric Factor B_n	Diffusive Porosity ϕ_n	Specific Surface Area $S_{A,n}$ (m^2/g)	Bulk Density $\rho_{b,n}$ (g/m^2)	Retardation Factor R_n	Formation Factor F_n	$D_{a,n}$ (m^2/s)
Refer to:				Table 4-1	Sect. 2.1	Eq. 2-1	Eq. 3-2	Table 2-1	Eq. 3-7
IC	0.02	layered	2.5	0.06	1	3000000	28	111	2.7E-12
IC,V	0.02	layered	2.5	0.01	1	3000000	175	104	2.9E-12

Table E-1. Damkohler Number Calculations for Cores C, D, and E

Core C										
Porosity Type	Half-Block Size l_n (m)	Geometry	Diffusive Porosity ϕ_n	Non-reactive β_n	Reactive β_n	Non-reactive α_n (1/s)	Reactive α_n (1/s)	Core Length L (m)	Non-reactive DaI_n	Reactive DaI_n
Refer to:			Table 4-1	Eq. 3-4	Eq. 3-4	Eq. 3-9	Eq. 3-9		Eq. 3-16	Eq. 3-16
IC	0.02	layered	0.10	7.69	14	1.7E-08	9.7E-10	0.1	0.15	0.14
IC,V	0.05	layered	0.002	0.11	15	2.9E-09	2.3E-12	0.1	0.003	0.0003
Core D										
Porosity Type	Half-Block Size l_n (m)	Geometry	Diffusive Porosity ϕ_n	Non-reactive β_n	Reactive β_n	Non-reactive α_n (1/s)	Reactive α_n (1/s)	Core Length L (m)	Non-reactive DaI_n	Reactive DaI_n
Refer to:			Table 4-1	Eq. 3-4	Eq. 3-4	Eq. 3-9	Eq. 3-9		Eq. 3-16	Eq. 3-16
IC	0.02	layered	0.09	2.8	5.6	1.7E-08	8.7E-10	0.1	0.06	0.05
IC,V	0.02	layered	0.002	0.045	5.9	1.8E-08	1.5E-11	0.1	0.02	0.0009
Core E										
Porosity Type	Half-Block Size l_n (m)	Geometry	Diffusive Porosity ϕ_n	Non-reactive β_n	Reactive β_n	Non-reactive α_n (1/s)	Reactive α_n (1/s)	Core Length L (m)	Non-reactive DaI_n	Reactive DaI_n
Refer to:			Table 4-1	Eq. 3-4	Eq. 3-4	Eq. 3-9	Eq. 3-9		Eq. 3-16	Eq. 3-16
IC	0.02	layered	0.06	0.83	2.5	1.7E-08	5.9E-10	0.1	0.03	0.02
IC,V	0.02	layered	0.01	0.14	2.5	1.8E-08	1.0E-10	0.1	0.02	0.003

Table E-2. Parameters for Cores

Non-Unit-Specific Parameters for cores	
Particle Density ρ_d (g/m^3)	2820000
Porewater Velocity v (m/s)	1E-07
K_a (m) for a K_d of 1	6.54E-07
Molecular Diffusion Coefficient in Water D_v (m^2/s)	3E-10
Core C parameters — Advective Porosity	
Advective Porosity – ϕ [Table 4-1]	0.01
Specific Surface Area – S_A (m^2/g) [Eq. 2-2]	0.06
Bulk Density – ρ_b (g/m^3) [Eq. 2-1]	2780000
Retardation Factor – R [Eq. 3-2]	9.5
Core D parameters — Advective Porosity	
Advective Porosity – ϕ [Table 4-1]	0.03
Specific Surface Area – S_A (m^2/g) [Eq. 2-2]	0.16
Bulk Density – ρ_b (g/m^3) [Eq. 2-1]	2730000
Retardation Factor – R [Eq. 3-2]	9.5
Core E parameters — Advective Porosity	
Advective Porosity – ϕ [Table 4-1]	0.08
Specific Surface Area – S_A (m^2/g) [Eq. 2-2]	0.38
Bulk Density – ρ_b (g/m^3) [Eq. 2-1]	2600000
Retardation Factor – R [Eq. 3-2]	9.4

WIPP
UC721 - DISTRIBUTION LIST
SAND97-0194

Federal Agencies

US Department of Energy (4)
Office of Civilian Radioactive Waste Mgmt.
Attn: Deputy Director, RW-2
Acting Director, RW-10
Office of Human Resources & Admin.
Director, RW-30
Office of Program Mgmt. & Integ.
Director, RW-40
Office of Waste Accept., Stor., & Tran.
Forrestal Building
Washington, DC 20585

Attn: Project Director
Yucca Mountain Site Characterization Office
Director, RW-3
Office of Quality Assurance
P.O. Box 30307
Las Vegas, NV 89036-0307

US Department of Energy
Albuquerque Operations Office
Attn: National Atomic Museum Library
P.O. Box 5400
Albuquerque, NM 87185-5400

US Department of Energy
Research & Waste Management Division
Attn: Director
P.O. Box E
Oak Ridge, TN 37831

US Department of Energy (6)
Carlsbad Area Office
Attn: G. Dials
D. Galbraith
M. McFadden
R. Lark
J. A. Mewhinney
G. Basabilvazo
P.O. Box 3090
Carlsbad, NM 88221-3090

US Department of Energy
Office of Environmental Restoration and
Waste Management
Attn: M Frei, EM-30
Forrestal Building
Washington, DC 20585-0002

US Department of Energy (3)
Office of Environmental Restoration and
Waste Management
Attn: J. Juri, EM-34, Trevion II
Washington, DC 20585-0002

US Department of Energy
Office of Environmental Restoration and
Waste Management
Attn: S. Schneider, EM-342, Trevion II
Washington, DC 20585-0002

US Department of Energy (2)
Office of Environment, Safety & Health
Attn: C. Borgstrom, EH-25
R. Pelletier, EH-231
Washington, DC 20585

US Department of Energy (2)
Idaho Operations Office
Fuel Processing & Waste Mgmt. Division
785 DOE Place
Idaho Falls, ID 83402

US Environmental Protection Agency (2)
Radiation Protection Programs
Attn: M. Oge
ANR-460
Washington, DC 20460

Boards

Defense Nuclear Facilities Safety Board
Attn: D. Winters
625 Indiana Ave. NW, Suite 700
Washington, DC 20004

Nuclear Waste Technical Review Board (2)
Attn: Chairman
J. L. Cohon
1100 Wilson Blvd., Suite 910
Arlington, VA 22209-2297

State Agencies

Attorney General of New Mexico
P.O. Drawer 1508
Santa Fe, NM 87504-1508

Environmental Evaluation Group (3)
Attn: Library
7007 Wyoming NE
Suite F-2
Albuquerque, NM 87109

NM Energy, Minerals, and Natural
Resources Department
Attn: Library
2040 S. Pacheco
Santa Fe, NM 87505

NM Environment Department (3)
Secretary of the Environment
Attn: Mark Weidler
1190 St. Francis Drive
Santa Fe, NM 87503-0968

NM Bureau of Mines & Mineral Resources
Socorro, NM 87801

Laboratories/Corporations

Battelle Pacific Northwest Laboratories
Battelle Blvd.
Richland, WA 99352

Los Alamos National Laboratory
Attn: B. Erdal, INC-12
P.O. Box 1663
Los Alamos, NM 87544

Tech Reps, Inc. (3)
Attn: J. Chapman (1)
Loretta Robledo (2)
5000 Marble NE, Suite 222
Albuquerque, NM 87110

Westinghouse Electric Corporation (5)
Attn: Library
J. Epstein
J. Lee
B. A. Howard
R. Kehrman
P.O. Box 2078
Carlsbad, NM 88221

S. Cohen & Associates
Attn: Bill Thurber
1355 Beverly Road
McLean, VA 22101

Thomas W. Doe
Golder Associates Inc.
4104 148th Avenue NE
Redmond, Washington 98052

**National Academy of Sciences,
WIPP Panel**

Howard Adler
Oxyrase, Incorporated
7327 Oak Ridge Highway
Knoxville, TN 37931

Tom Kiess
Board of Radioactive Waste Management
GF456
2101 Constitution Ave.
Washington, DC 20418

Rodney C. Ewing
Department of Geology
University of New Mexico
Albuquerque, NM 87131

Charles Fairhurst
Department of Civil and Mineral Engineering
University of Minnesota
500 Pillsbury Dr. SE
Minneapolis, MN 55455-0220

B. John Garrick
PLG Incorporated
4590 MacArthur Blvd., Suite 400
Newport Beach, CA 92660-2027

Leonard F. Konikow
US Geological Survey
431 National Center
Reston, VA 22092

Carl A. Anderson, Director
Board of Radioactive Waste Management
National Research Council
HA 456
2101 Constitution Ave. NW
Washington, DC 20418

Christopher G. Whipple
ICF Kaiser Engineers
1800 Harrison St., 7th Floor
Oakland, CA 94612-3430

John O. Blomeke
720 Clubhouse Way
Knoxville, TN 37909

Sue B. Clark
University of Georgia
Savannah River Ecology Lab
P.O. Drawer E
Aiken, SC 29802

Konrad B. Krauskopf
Department of Geology
Stanford University
Stanford, CA 94305-2115

Della Roy
Pennsylvania State University
217 Materials Research Lab
Hastings Road
University Park, PA 16802

David A. Waite
CH_2 M Hill
P.O. Box 91500
Bellevue, WA 98009-2050

Thomas A. Zordon
Zordan Associates, Inc.
3807 Edinburg Drive
Murrysville, PA 15668

Universities

University of New Mexico
Geology Department
Attn: Library
141 Northrop Hall
Albuquerque, NM 87131

University of Washington
College of Ocean & Fishery Sciences
Attn: G. R. Heath
583 Henderson Hall, HN-15
Seattle, WA 98195

Libraries

Thomas Brannigan Library
Attn: D. Dresp
106 W. Hadley St.
Las Cruces, NM 88001

Government Publications Department
Zimmerman Library
University of New Mexico
Albuquerque, NM 87131

New Mexico Junior College
Pannell Library
Attn: R. Hill
Lovington Highway
Hobbs, NM 88240

New Mexico State Library
Attn: N. McCallan
325 Don Gaspar
Santa Fe, NM 87503

New Mexico Tech
Martin Speere Memorial Library
Campus Street
Socorro, NM 87810

WIPP Public Reading Room
Carlsbad Public Library
101 S. Halagueno St.
Carlsbad, NM 88220

Foreign Addresses

Atomic Energy of Canada, Ltd. (2)
Whiteshell Laboratories
Attn: B. Goodwin
C. C. Davison
Pinawa, Manitoba, CANADA R0E 1L0

Atomic Energy Control Board
Attn: Peter Flavelle
P. O. Box 1046, Station B
280 Slater Street
Ottawa, K18 5S9
CANADA

Francois Chenevier (2)
ANDRA
Route de Panorama Robert Schumann
B. P. 38
92266 Fontenay-aux-Roses, Cedex
FRANCE

Claude Sombret
Centre d'Etudes Nucleaires de la Vallee Rhone
CEN/VALRHO
S.D.H.A. B.P. 171
30205 Bagnols-Sur-Ceze
FRANCE

Commissariat a L'Energie Atomique
Attn: D. Alexandre
Centre d'Etudes de Cadarache
13108 Saint Paul Lez Durance Cedex
FRANCE

Philippe Lalieux
OECD Nuclear Energy Agency
LeSeine St-Germain
12 Boulevard des Iles
92130 Issy-les-Moulineaux
FRANCE

Claudio Pescatore
OECD Nuclear Energy Agency
Le Seine St. Germain
12 Boulevard des Iles
92130 Issy-les-Moulineaux
FRANCE

Alain Galli
Centre de Geostatistique
Ecole de Mines de Paris
35 rue St. Honore
77035 Fountainebleau
FRANCE

Dr. Ghislain de Marsily
Universite Paris VI
Laboratoire de Geologie Appliquee
4 place JUSSIEN
75230 Cedex 05
FRANCE

Jean-Francois Aranyossy
ANDRA
Parc de la Croix Blanche
1-7 rue Jean Monnet
92298 Chatenay-Malabry, Cedex
FRANCE

Jean-Yves Boisson
CEA/IPSN
DPRE/SERGD
CEN/FAR
BP N 6
92265 Fontenay-aux-Roses Cedex
FRANCE

Bundesanstalt fur Geowissenschaften und Rohstoffe
Attn: M. Langer
Postfach 510 153
D-30631 Hannover
GERMANY

Wernt Brewitz
GRS
Final Repository Safety Research Division
Theodor-Heuss Strasse 4
38122 Braunschweig
GERMANY

Bundesministerium fur Forschung und Technologie
Postfach 200 706
5300 Bonn 2
GERMANY

Gesellschaft fur Anlagen und Reaktorsicherheit (GRS)
Attn: B. Baltes
Schwertnergasse 1
D-50667 Cologne
GERMANY

Gesellschaft fur Anlagen-und Reaktosicherheit (GRS) mbH
Attn: P. Bogorinski
Schwertnergasse 1
D-50667 Koln
GERMANY

Gessellschaft fur Anlagen-und Reaktosicherheit (GRS) mbH
Attn: Eckhard Fein
Theodor-Heuss Strasse 4
D-38122 Braunschweig
GERMANY

Manfred Wallner
BGR
Federal Institute for Geosciences & Natural Resources
Stilleweg 2
30655 Hannover
GERMANY

VTT Energy
Attn: Aimo Hautojarvi
Teckniikantie 4 C, Espoo
P. O. Box 1604
FIN - 02044 VTT
FINLAND

Timo Aikas
Posiva Oy
Annankaatu 42 D
00100 Helsinki
FINLAND

Paavo Vuorela
Geological Survey of Finland
Nuclear Waste and Engineering Geology Unit
Betonimiehenkuja 4
02150 Espoo
FINLAND

Shingo Tashiro
Japan Atomic Energy Research Institute
Tokai-Mura, Ibaraki-Ken, 319-11
JAPAN

Erik K. Webb
Power Reactor and Nuclear Fuel Development Corporation
Muramatsu, Tokai-Mura
Naka, Ibaraki
JAPAN

Netherlands Energy Research Foundation ECN
Attn: J. Prij
3 Westerduinweg
P.O. Box 1
1755 ZG Petten
THE NETHERLANDS

Svensk Karnbransleforsorjning AB
Attn: F. Karlsson
Project KBS (Karnbranslesakerhet)
Box 5864
S-102 48 Stockholm
SWEDEN

Olle Olsson
SKB Aspo HRL
PL 300
S-572 95 Figeholm
SWEDEN

Anders Winberg
Conterra AB
Ogardesvagen 4
S-433 30 Parthle
SWEDEN

Lars O. Ericsson
SKB
Box 5864
102 40 Stockholm
SWEDEN

Fritz Kautsky
SKI 106 52 Stockholm
SWEDEN

Nationale Genossenschaft fur die Lagerung Radioaktiver Abfalle (2)
Attn: S. Vomvoris
P. Zuidema
Hardstrasse 73
CH-5430 Wettingen
SWITZERLAND

Marc Thury
NAGRA
Chief Geologist
Hardstrasse 73
5430 Wettingen
SWITZERLAND

AEA Technology
Attn: J. H. Rees
D5W/29 Culham Laboratory
Abington, Oxfordshire OX14 3DB
UNITED KINGDOM

AEA Technology
Attn: W. R. Rodwell
044/A31 Winfrith Technical Centre
Dorchester, Dorset DT2 8DH
UNITED KINGDOM

AEA Technology
Attn: J. E. Tinson
B4244 Harwell Laboratory
Didcot, Oxfordshire OX11 ORA
UNITED KINGDOM

Alan J. Hooper
UK NIREX Ltd
Manager for Science
Curie Avenue
Harwell, Didcot
Oxfordshire OX11 ORH
UNITED KINGDOM

Peter Grindrod
QuantiSci Ltd.
Chiltern House, 45 Station Road
Henley-on-Thames
Oxfordshire, RG9 1AT
UNITED KINGDOM

Rae Mackay
Dept. of Civil Engineering
University of Newcastle Upon Tyne
Newcastle Upon Tyne NE1 7RU
UNITED KINGDOM

Dr. Brian Berkowitz
Weizmann Institute of Science
Dept. of Environmental Sciences/
Energy Research
Rehovot 76100
ISRAEL

Gedeon Dagan
Dept. of Fluid Mechanics / Heat Transfer
Tel Aviv Univeristy
P.O. Box 39040
Ramat Aviv, Tel Aviv 69978
ISRAEL

Peter Airey
ANSTO
Environment Division
Lucas Heights Research Laboratories
PM 1, PO
Menai, NSW 2234
AUSTRALIA

Bernard Neerdael
SCK/CEN
Waste and Disposal Department
Boeretang 200
2400 Mol
BELGIUM

Dr. J. Jaime Gomez Hernandez
Departmetno de Ingenieria Hidraulica y Med io
Ambiente
Universidad Politecnice de Valencia
46071 Valencia
SPAIN

Jesus Carrera
Universidad Politechnica de Catalunya
E.T. S. I. Caminos
Jordi, Girona 31
E-08034 Barcelona
SPAIN

Carl Axness
ETS Ingenieros de Caminos, C.iP.c/. Gran
Capitan, s/n
Modul D-2
08034, Barcelona
SPAIN

Others

Sean Fleming
Dept. of Geosciences
Oregon State University
Corvallis, OR 97331-6605

Roy Haggerty
Dept. of Geosciences, Wilkinson 104
Oregon State University
Corvallis, OR 97331-5506

Dr. Brian Wagner
USGS
345 Middlefield Rd, MS 409
Menlo Park, CA 94025

Dr. Charles Harvey
Division of Engineering and Applied Sciences
29 Oxford St.
Pierce 118
Cambridge, MA 02138

Robert M. Holt (20)
Consulting Hydrogeologist
17 Sunset Blvd.
Placitas, NM 87043

D. W. Powers
HC 12 Box 87
Anthony, TX 79821

John D. Bredehoeft
Western Region Hydrologist
Water Resources Division
US Geological Survey (MS 439)
345 Middlefield Road
Menlo Park, CA 94025

Dr. Rafael Bras
MIT
Department of Civil Engineering
Room 48-311
Water Resources and Environmental Eng. Div.
Cambridge, MA 02139

Dr. Steve Gorelick, Assoc. Prof.
Dept. of Geological and Environmental Sci.
Mitchell Bldg. - First Floor
Stanford University
Stanford, CA 94305-2225

Dr. Shlomo Neuman
College of Engineering and Mines
Dept. of Hydrology and Water Resources
University of Arizona
Tucson, AZ 85721

Dr. Peter K. Kitanidis
Department of Civil Engineering
Terman Engineering Center
Stanford University
Stanford, CA 94305-4020

Dr. Dennis McLaughlin
Associate Professor
MIT
Room 48-209
Cambridge, MA 02139

Dr. Anil Kumar Mishra
Earth Science Division
MS 90-1116
E.O. Lawrence Berkeley Laboratory
One Cyclotron Road
Berkeley, CA 94720

D. A. Zimmerman
GRAM, Inc.
8500 Menaul Blvd. NE
Suite B335
Albuquerque, NM 87112

Mr. Walt Beyeler
SAIC
2201 Buena Vista Blvd. SE
Albuquerque, NM 87016

INTERA, Inc. (2)
Attn: M. LaVenue
B. S. Rama Rao
6850 Austin Center Blvd.
Austin, TX 78731

Dr. Carol Gotway
Center for Disease Control and Prevention
National Immunization Program
Statistical Analysis Branch, Bldg. 12
Corporate Square Blvd.
Atlanta, GA 30329

Yorim Rubin
Department of Civil Engineering
University of California, Berkeley
Berkeley, CA 94270

Allan Gutjahr
Dept. of Mathematics
New Mexico Institute of Mining and
Technology
Socorro, NM 87801

Internal

MS	Org.	
1324	6115	P. B. Davies
1320	6831	E. J. Nowak
1322	6121	J. R. Tillerson
1328	6849	D. R. Anderson
1328	6848	H. N. Jow
1335	6801	M. Chu
1341	6832	J. T. Holmes
1395	6800	L. Shephard
1395	6821	M. Marietta
1341	6115	W. G. Perkins (10)
1341	6832	L. Brush (10)
1341	6832	D. Lucero (2)
1341	6832	M. Siegel (10)
1341	6832	H. W. Papenguth
1328	6849	J. Ramsey
1324	6115	T. Corbet
1324	6115	S. McKenna
1328	6849	A. Treadway
1324	6115	R. Beauheim
1324	6115	L. Meigs (20)
1322	6121	K. Knowles
1395	6821	K. Larson

1335	6801	P. Swift
1328	6848	L. Hill
1345	6416	D. P. Gallegos
1337	6000	W. Weart
1330	6811	K. Hart (2)
1330	4415	NWM Library (60)
9018	8940-2	Central Technical Files
0899	4916	Technical Library (5)
0619	12690	Review and Approval Desk (2), For DOE/OSTI